The Astrophysical Journal, 995:228 (32pp), 2025 December 20 https://doi.org/10.3847/1538-4357/ae1501

A Luminous and Hot Infrared through X-Ray Transient at a 5 kpc Offset from a Dwarf Galaxy

Jean J. Somalwar[1], Vikram Ravi[1], Raffaella Margutti[2,3], Ryan Chornock[2], Priyamvada Natarajan[4,5,6], Wenbin Lu[2,7], Charlotte Angus[8], Matthew J. Graham[1], Erica Hammerstein[2], Edward Nathan[1], Matt Nicholl[8], Kritti Sharma[1], Robert Stein[9,10,11], Frank Verdi[1], Yuhan Yao[2,12], Eric C. Bellm[13], Tracy X. Chen[14], Michael W. Coughlin[15], David Hale[16], Mansi M. Kasliwal[1], Russ R. Laher[14], Reed Riddle[16], and Jesper Sollerman[17]
[1] Cahill Center for Astronomy and Astrophysics, MC 249-17 California Institute of Technology, Pasadena CA 91125, USA; jsomalwa@caltech.edu
[2] Department of Astronomy, University of California, Berkeley, CA 94720-3411, USA
[3] Department of Physics, University of California, 366 Physics North MC 7300, Berkeley, CA 94720, USA
[4] Department of Astronomy, Yale University, P.O. Box 208101, New Haven, CT 06520, USA
[5] Black Hole Initiative, Harvard University, Cambridge, MA 02138, USA
[6] Department of Physics, Yale University, P.O. Box 208121, New Haven, CT 06520, USA
[7] Theoretical Astrophysics Center, University of California, Berkeley, CA 94720, USA
[8] Astrophysics Research Centre, School of Mathematics and Physics, Queens University Belfast, Belfast BT7 1NN, UK
[9] Department of Astronomy, University of Maryland, College Park, MD 20742, USA
[10] Joint Space-Science Institute, University of Maryland, College Park, MD 20742, USA
[11] Astrophysics Science Division, NASA Goddard Space Flight Center, Mail Code 661, Greenbelt, MD 20771, USA
[12] Miller Institute for Basic Research in Science, 468 Donner Lab, Berkeley, CA 94720, USA
[13] DIRAC Institute, Department of Astronomy, University of Washington, 3910 15th Avenue NE, Seattle, WA 98195, USA
[14] IPAC, California Institute of Technology, 1200 E. California Blvd, Pasadena, CA 91125, USA
[15] School of Physics and Astronomy, University of Minnesota, Minneapolis, MN 55455, USA
[16] Caltech Optical Observatories, California Institute of Technology, Pasadena, CA 91125, USA
[17] Department of Astronomy, The Oskar Klein Center, Stockholm University, AlbaNova University Center, SE 106 91 Stockholm, Sweden
Received 2025 May 16; revised 2025 October 9; accepted 2025 October 17; published 2025 December 19

Abstract

We are searching for hot, constant-color, offset optical flares in the Zwicky Transient Facility data stream that are $>10''$ from any galaxy in public imaging data from the PanSTARRS survey. Here, we present the first discovery from this search: AT 2024puz, a luminous multiwavelength transient offset by 5 kpc from a $\sim 10^8\,M_\odot$ galaxy at $z = 0.356$ with a low–moderate star formation rate ($0.01 \pm 0.003\,M_\odot\,\mathrm{yr}^{-1}$). It produced luminous $10^{44.79\pm0.04}\,\mathrm{erg\,s}^{-1}$ optical/UV emission that evolved on a $\sim$20 day timescale, as well as $10^{44.12\pm0.03}\,\mathrm{erg\,s}^{-1}$ X-ray emission with a photon-index $\Gamma = 1.73^{+0.10}_{-0.09}$. No associated radio or millimeter emission was detected. We show that the early time optical emission is likely powered by reprocessing of high-energy, accretion-powered radiation, with a possible contribution from a shock in a dense circumtransient medium. If the shock is dominant at early times, the circumtransient medium has a mass $\sim$0.1–1 $M_\odot$, a radius 10^{15} cm, and a density profile shallower than $\sim r^{-1}$. A near-infrared excess appears at late-times and is suggestive of reprocessing within a wind or other circumtransient medium. The X-rays are most consistent with a central engine. We suggest that AT 2024puz may be associated with an accretion event onto a 50–$10^5\,M_\odot$ black hole, where the lower masses are preferred based on the large projected offset from the host galaxy. AT2024puz exhibits properties similar to both luminous, fast, blue optical transients and tidal disruption events, but is intermediate between them in its energetics and evolution timescale. This highlights the need for broader exploration of the landscape of hot optical transients to trace their origins.

Unified Astronomy Thesaurus concepts: Astrophysical black holes (98); Intermediate-mass black holes (816); Transient sources (1851); Ultraviolet transient sources (1854); X-ray transient sources (1852); Tidal disruption (1696); Dwarf galaxies (416)

1. Introduction

Many open questions surround the formation and demographics of black holes (BHs) with masses $10^{2-5}\,M_\odot$. The mass function of stellar-mass BHs informs models of stellar evolution. The "upper mass gap" of stellar-mass BHs, near $\sim 50\,M_\odot$, is thought to be the result of an implosion of more massive stars in pulsational pair instability supernovae (SNe), but gravitational-wave searches have begun detecting objects above this limit (S. E. Woosley 2017; B. P. Abbott et al. 2019), possibly due to mergers of massive stellar BHs in dense environments (K. Kremer et al. 2020).

These massive stellar-mass BHs may be the local Universe analogs of the seeds of SMBHs (BH mass $M_{\rm BH} > 10^6\,M_\odot$). SMBH seeding and growth are some of the biggest open problems in astrophysics (P. Natarajan 2014; K. Inayoshi et al. 2020). If BHs with masses $\sim 100\,M_\odot$, formed from the stellar remnants of the first stars at high redshift, can grow rapidly through super-Eddington accretion, they may be able to form SMBHs detected at both high and low redshifts as proposed by the light seed models of SMBH growth (P. Madau & M. J. Rees 2001; P. Natarajan 2014). Additionally, amplified growth of light seeds might be incubated in nuclear star clusters that might operate throughout cosmic time, leading to the formation of intermediate-mass BHs (IMBHs) even in the

nearby Universe (P. Natarajan 2021). Heavy seed models invoke $\sim 10^4\,M_\odot$ gas clouds that directly collapse into BHs in the early Universe (A. Loeb & F. A. Rasio 1994; G. Lodato & P. Natarajan 2006) or stellar-mass BHs that rapidly accrete through runaway mergers and/or rapid accretion in dense environments (M. C. Miller & D. P. Hamilton 2002; B. Devecchi & M. Volonteri 2009; T. Alexander & P. Natarajan 2014). The resulting massive BHs may subsequently grow through Eddington-limited accretion to SMBH masses over time. These models produce distinct, observable predictions for the present-day demographics, occupation fraction, and locations of IMBHs ($M_{\rm BH} \sim 10^{2-5}\,M_\odot$) (J. E. Greene et al. 2020).

To solve these challenging open problems, we must discover more massive stellar and supermassive BHs. Transient emission is proving to be the most promising method of doing so, as it uncovers both active and quiescent BHs. In particular, transient optical flaring is enabling us to discover *populations* of time-domain varying events associated with compact objects and pushing to new regimes of their physics. Accretion flares from low-mass SMBHs and IMBHs form a clear example of this, which we briefly outline here.

Tidal disruption events (TDEs) occur when a massive black hole (MBH; $M_{\rm BH} \sim 10^{2-9}\,M_\odot$) tidally shreds a nearby star (M. J. Rees 1988; C. R. Evans & C. S. Kochanek 1989; E. S. Phinney 1989). TDEs produce luminous electromagnetic flares and illuminate otherwise nonaccreting and unobservable MBHs. To date, $\sim$100 TDEs have been discovered, largely thanks to wide-field, cadenced, optical surveys, like the Zwicky Transient Facility (ZTF; E. C. Bellm et al. 2019b; M. J. Graham et al. 2019; F. J. Masci et al. 2019; R. Dekany et al. 2020), All Sky Automated Survey for SuperNovae (B. J. Shappee et al. 2014; C. S. Kochanek et al. 2017), Panoramic Survey Telescope and Rapid Response System (PS1; K. C. Chambers et al. 2016), and Asteroid Terrestrial-impact Last Alert System (ATLAS; J. L. Tonry et al. 2018). These have contributed $\gtrsim$100 events in the last decade (e.g., T. W.-S. Holoien et al. 2019, 2020; S. van Velzen et al. 2019, 2021; J. T. Hinkle et al. 2020, 2023; E. Hammerstein et al. 2023; Y. Yao et al. 2023; W. B. Hoogendam et al. 2024). TDEs produce blue, hot ($T \sim 10^{4-5}$ K) optical flares that show minimal cooling and evolve over weeks–months.

TDE discoveries are beginning to push down to the lowest-mass SMBHs known ($\sim 10^5\,M_\odot$; e.g., C. R. Angus et al. 2022; Y. Yao et al. 2024), providing unique access and potential for discovering the elusive population of bona-fide IMBHs. Selection effects, however, may be preventing discoveries of a population of IMBH TDEs. In ZTF, TDEs are typically identified as blue ($g - r < 0.2$ mag), constant color ($d(g-r)/dt < 0.02$ mag day^{-1}), coincident with the location of a galactic nucleus, defined by pre-TDE images from public survey data (typically Pan-STARRS; K. C. Chambers et al. 2016; S. van Velzen et al. 2019; Y. Yao et al. 2023). The last host galaxy cut is particularly significant for ZTF IMBH TDE sensitivity. First, many IMBHs are expected to be hosted by dwarf galaxies, which are not detectable to large comoving volumes in typical survey data (e.g., a $10^8\,M_\odot$ galaxy can be detected to $z \approx 0.1$ in Pan-STARRS). Requiring a detectable host galaxy typically rules out these sources. Likewise, dwarf galaxies may not have well-defined nuclei, or gravitational potential minima (E. J. Weller et al. 2022), but TDEs are required to reside in their hosts' nuclei. Off-center TDEs are expected to be more numerous in more massive galaxies from wandering IMBHs in the hierarchical buildup of structure in the standard Λ cold dark matter paradigm via mergers of galaxies and the BHs hosted by them (A. Ricarte et al. 2021b). These will likewise be excluded from current searches (but see Y. Yao et al. 2025).

Searches of optical transient surveys that focus on non-TDE phenomena do not suffer from the same selection effects, and so may be more sensitive to IMBHs. One candidate for an IMBH-triggered transient is the luminous, fast, blue, optical transient (LFBOT; S. J. Prentice et al. 2018; R. Margutti et al. 2019; D. L. Coppejans et al. 2020; B. D. Metzger 2022; C. P. Gutiérrez et al. 2024). LFBOTs have an optical evolution similar to TDEs (blue, constant color), but vary on much faster timescales $\lesssim$1 week and always offset from their host galaxy center (e.g., A. Y. Q. Ho et al. 2019; D. A. Perley et al. 2019; D. L. Coppejans et al. 2020; A. Y. Q. Ho et al. 2020, 2023; J. S. Bright et al. 2022; A. Y. Q. Ho et al. 2022; A. Inkenhaag et al. 2023; A. A. Chrimes et al. 2024a, 2024b; C. P. Gutiérrez et al. 2024; G. Migliori et al. 2024). They are produced by a compact object of an as yet unknown nature: stellar-mass BHs, IMBHs, and neutron stars (NSs) have all been proposed as potential sources (R. Margutti et al. 2019; B. D. Metzger 2022; D. R. Pasham et al. 2022; L. Li et al. 2024; D. Tsuna & W. Lu 2025). Like TDE searches, LFBOT searches may be limited by other selection effects: events are typically required to rise and fade on a $\lesssim$week timescale (A. Y. Q. Ho et al. 2023), which is significantly faster than almost all SMBH TDEs (Y. Yao et al. 2023), leaving a gap between these populations. If LFBOTs are not TDEs, they are likely triggered by accretion onto an NS or stellar-mass BH, or spin-down of a young magnetar (see R. Margutti et al. 2019; and references therein).

If we want to identify the nature of the compact object that triggers LFBOTs, or find definitive accreting IMBHs, we must extend optical transient searches to span the parameter space intermediate to TDEs and LFBOTs. In other words, we need to map out the full range of these extreme, energetic, hot optical transients, regardless of timescale or host galaxy. This will allow us to conclusively connect these populations, or show that they are distinct and that LFBOTs are more likely associated with stellar-mass compact objects, as well as potentially identify new types of transients.

This paper presents the first discovery of our ongoing effort to explore the full landscape of energetic, hot optical transients with ZTF. Here, we present AT 2024puz (hereafter 24puz), a luminous, multiwavelength transient in a dwarf galaxy that may be associated with an extreme compact object accretion event. We favor models with an accreting BH ranging in a mass 50–$10^5\,M_\odot$. In Section 2, we present the parameters of the search in which we discovered 24puz. In Section 3, we detail our extensive multiwavelength follow-up effort and data reduction. In Section 4, we analyze our observations to constrain the basic physical parameters of 24puz. In Section 5, we constrain the emission mechanisms and sizes of the emitting regions. In Section 6, we compare 24puz to similar transient classes, constrain the rate of 24puz-like events, and comment on the most likely kind of compact object powering the event. Finally, we present our conclusions and future prospects in Section 7.

We adopt the Plank2015 (P. A. Ade et al. 2016) cosmology with $H_0 = 67.7\,{\rm km\,s^{-1}}$ and $\Omega_M = 0.3075$. We correct for Milky Way extinction using the (E. Fitzpatrick 1999)

extinction law with $A_V = 0.1$ mag and $R_V = 3.1$ (D. J. Schlegel et al. 1998).

2. Discovery

24puz was the first discovery from an ongoing, real-time search for hostless or highly offset, consistently blue, optical transients with ZTF (E. C. Bellm et al. 2019b; M. J. Graham et al. 2019; F. J. Masci et al. 2019; R. Dekany et al. 2020). ZTF conducts several public and private surveys using the Palomar 48 inch Schmidt telescope (E. C. Bellm et al. 2019a). The public survey covers the northern sky once every 2 days in the g and r bands, while private surveys include i band as well as high-cadence observations of smaller areas. We identify candidates in ZTF alert photometry from the `kowalski` broker (S. J. v. d. Walt et al. 2019; M. W. Coughlin et al. 2023). Our cuts are identical to those for the TDE sample in Y. Yao et al. (2023; see Section 2.2), except that we require a significant offset from the nearest PanSTARRS source ($>10''$). The significant offset requirement aimed to reject supernovae that were offset from massive host galaxies, and was chosen by testing for this pilot search. The resulting redshift-dependent distance threshold would bias a sample study, and as such should not be used or should be considered carefully in assessing selection effects. Because our initial search aimed to identify single objects, it does not affect our results. The goal of this search is to identify TDE-like events that are either at higher redshift or in low-mass galaxies.

We manually scan through the resulting candidates on a ∼weekly basis using the `fritz.science` instance of the SkyPortal platform (S. J. v. d. Walt et al. 2019; M. W. Coughlin et al. 2023). We identify sources that have lightcurves that are inconsistent with a cataclysmic variable, which form our main background. We do this by rejecting sources that have no observations during the flare rise and a perfectly linear decay (by eye) in magnitude space, with no color evolution. We obtain rapid follow-up with the Spectral Energy Distribution Machine (SEDM) on the Palomar 60 inch telescope (N. Blagorodnova et al. 2018; M. Rigault et al. 2019) and/or the Low Resolution Imaging Spectrometer (LRIS) on the Keck I telescope (J. B. Oke et al. 1995), with some dependence on our telescope allocations. We rule out any objects with spectra that have features that are well modeled as a supernova or that are at $z \approx 0$. We continue to follow up any remaining sources.

24puz was first reported on the Transient Name Survey by J. Sollerman et al. (2024) on 2024 July 20 or MJD 60511 and was the first source to pass all these cuts, a few months after we began our search. The ZTF lightcurve for this source (described in detail below) is shown in the top left panel of Figure 1. We initiated an expansive multiwavelength follow-up for 24puz upon obtaining a Keck I/LRIS spectrum that showed a featureless spectrum with galaxy interstellar matter (ISM) absorption features at $z = 0.356$. Figure 2 compares the optical properties of 24puz to other classes of featureless, blue transients (LFBOTs and TDEs); we will discuss this figure in detail in Section 6, but include it here for context.

The first ZTF forced-photometry detection ($>3\sigma$) of 24puz occurred on MJD 60507, or 2024 July 16. We adopt this MJD as the discovery date t_0 throughout this work.

3. Multiwavelength Observations and Data Reduction

In this section, we summarize archival and follow-up observations and our data reduction procedures.

3.1. Zwicky Transient Facility

While we discovered 24puz in alert photometry from ZTF, we perform all analyzes using forced photometry from the IPAC ZTF forced-photometry server (F. J. Masci et al. 2023) in the *gri* bands. This server performs point-spread function photometry on ZTF difference images. We processed the resulting lightcurve following recommended procedures,[18] and it is shown in Figure 1.

3.2. Palomar 60 inch Rainbow Camera

We obtained optical *ugri* photometry of 24puz with the SEDM rainbow imager on the Palomar 60 inch telescope (PI: R. Stein; N. Blagorodnova et al. 2018). The observations are summarized in Table 4. We reduce the data using the automated pipeline.[19]

3.3. Palomar 200 inch Wide Field Infrared Camera

We observed 24puz with the Wide Field Infrared Camera (WIRC) on the Palomar 200 inch telescope on MJDs 60526 (2024 August 4; PI S. Ocker) and 60546 (2024 August 24; PI V. Ravi). We used the J band and exposure times of 1620 and 6525 s, respectively. We reduced both epochs using the `irImagePipe` code (K. De et al. 2020) using default settings, including flux calibration against sources from the Two Micron All Sky Survey catalog (R. M. Cutri et al. 2003). We measured the source flux in an aperture of the radius 7 pix and subtracted the median background in an annulus of [10, 50] pix. The source was detected at J-band flux densities of 14.2 ± 1.6 and 5.9 ± 1.2 μJy in each epoch.

3.4. The Neil Gehrels Swift Observatory

We obtained observations of 24puz with the Neil Gehrels Swift Observatory (Swift; N. Gehrels et al. 2004) through ToOs 20912 and 20962 (PI Somalwar, object ID 16746). The observations are summarized in Tables 8 and 7. The X-Ray Telescope (XRT) was used in photon counting mode, and the Ultra-violet Optical Telescope (UVOT) observations used the u, uvm2, uvw1, and uvw2 filters.

We first describe the UVOT data reduction and then the XRT. For UVOT, we used the default data reduction provided by the observatory. We measured the source flux in all bands using an aperture centered on the position of 24puz with the radius $5''$ and a background region offset from the source region with the radius $20''$. We used the `uvotsource` tool in `heasoft` (v6.34) to perform the photometry. We used the `ssstype=high` flag to reject observations where the transient was located in a low-sensitivity region. The measured fluxes for all good observations are detailed in Table 7.

We processed the XRT data using the online Swift/XRT data products tool.[20] We used the lightcurve tool to measure the count rate in each observation, adopting the ZTF coordinates of 24puz and a 3σ detection threshold. We used default

[18] https://irsa.ipac.caltech.edu/data/ZTF/docs/ztf_forced_photometry.pdf
[19] https://sites.astro.caltech.edu/sedm/Pipeline.html
[20] https://www.swift.ac.uk/user_objects/

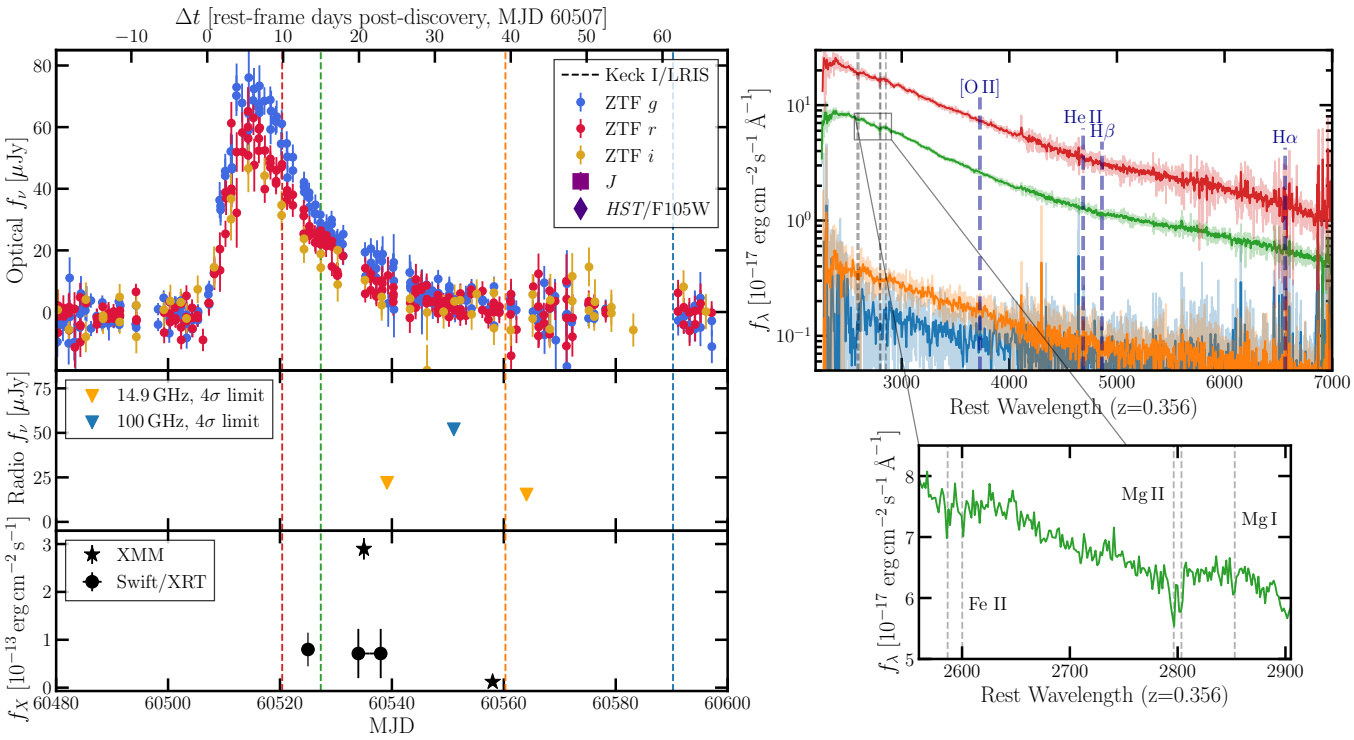

Figure 1. Summary of emission from 24puz. The left panel shows the ZTF lightcurve on the top panel, the radio/millimeter upper limits in the middle panel, and the 0.3–10 keV Swift/XRT and XMM-Newton lightcurves in the bottom panel. The X-ray fluxes are computed as the unabsorbed, observed 0.3–10 keV flux assuming a $\Gamma = 1.77$ power law. The two Swift/XRT observations that are joined together by a line were individually nondetections, so we show the flux measured by stacking the two observations, which is significant. Dates of Keck I/LRIS spectroscopy are shown as dashed lines. The top right panels show the optical spectral sequence, which no significant features detected. The solid lines are smoothed by a Gaussian with width of 5 pix. The faded lines show the unsmoothed spectra. Commonly detected transient lines are shown as dashed blue lines; none are detected. The apparent line in the red, MJD 60520 spectrum near 4000 Å is a poorly subtracted sky line. The bottom right panel shows a zoom-in on the detected absorption lines, with the lines labeled in gray.

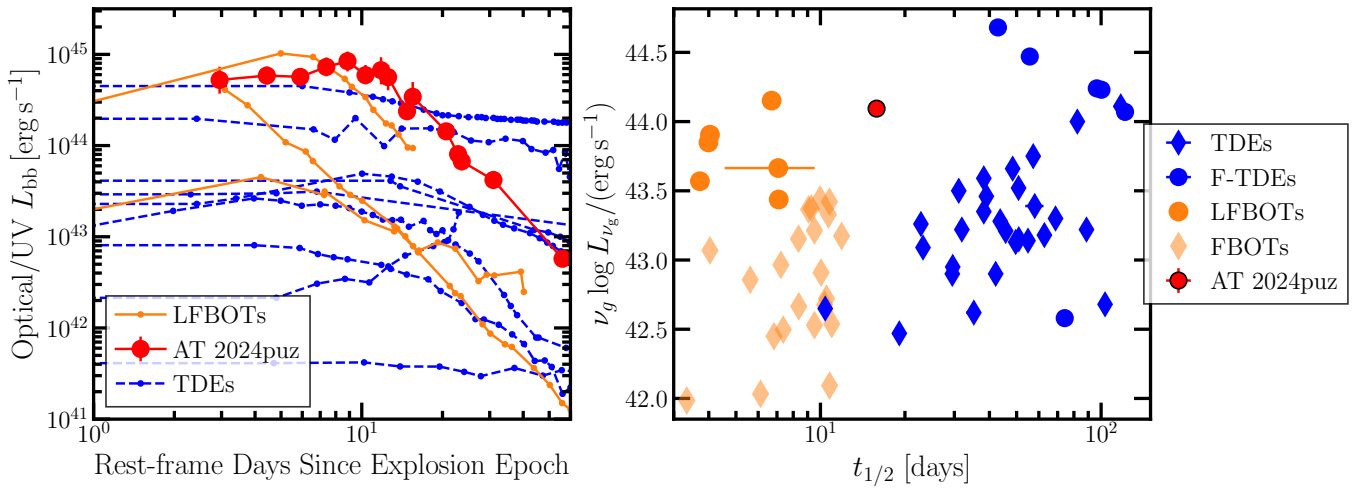

Figure 2. Comparison between the optical/UV emission from 24puz, LFBOTs (A. Y. Q. Ho et al. 2023; Y. Yao et al. 2023; A. A. Chrimes et al. 2024b; M. Pursiainen et al. 2024), and TDEs (Y. Yao et al. 2023; J. J. Somalwar et al. 2025). In all panels, LFBOTs are shown in orange, TDEs are shown in blue, and 24puz in red. The left panel shows the blackbody luminosity evolution. Observational constraints are shown as points, whereas the lines show linear extrapolations between observations. In the case of TDEs, we show the compilation from J. J. Somalwar et al. (2025), who identified TDEs with published nonparametric blackbody luminosity modeling (T. W. S. Holoien et al. 2014, 2016; N. Blagorodnova et al. 2017, 2019; M. Nicholl et al. 2020; A. V. Payne et al. 2021; P. Charalampopoulos et al. 2023). We show the lightcurves relative to the first constraint, which is typically postpeak, explaining the relatively flat early time lightcurves. LFBOTs show rapid fading with a similar late-time power-law decay as 24puz, but on overall slower timescales and typically with fainter luminosities. TDEs show a range of lightcurve shapes, which generally evolve slower than that of 24puz. Some TDEs show a rapid fade like 24puz, but these are all at least 1 order of magnitude fainter than 24puz. These trends are highlighted in the right panel, which shows the peak g-band luminosity versus time above half-peak luminosity. We also include fast blue optical transients (FBOTs) as faint diamonds. TDEs are divided into featureless TDEs (F-TDEs, circles), which show featureless spectra like 24puz, and those that have transient spectral features (diamonds). 24puz is intermediate to LFBOTs and TDEs, and is notably more luminous than all events at a similar timescale and is much faster evolving than F-TDEs.

settings and binned by observation ID (ObsID). We converted counts to fluxes assuming a power-law spectrum with the photon-index $\Gamma = 1.7$, motivated by our X-ray spectral modeling in Section 5.1.3, and Milky Way absorption with $n_{\rm H} = 2.88 \times 10^{20}\,{\rm cm}^{-2}$ (N. Ben Bekhti et al. 2016). The resulting count rates and upper limits are shown in Table 8.

3.5. The XMM-Newton Telescope

We observed 24puz with the XMM-Newton telescope on the dates and with the exposure times listed in Table 9. We used the thin filters for all observations. We retrieved the PPS data for each observation from the XMM-Newton archive. For each epoch, we extracted a spectrum of 24puz following recommended procedures,[21] including flagging bad time intervals using the `tabtigen` command with a rate upper limit found by manual inspection of the lightcurve. We process the data from all three EPIC cameras and perform all fitting to the data from the three detectors together. We centered the source apertures on the ZTF position of 24puz and used radii of 20″ to avoid contamination from a nearby source. We used 30″ background regions close to the source but uncontaminated by any nearby sources. Our first EPIC-planetary nebula (PN) exposure had the strongest contamination, and so, the effective exposure time quoted in Table 9 is lower than the on-source time as observed by the telescope.

3.6. The Nuclear Spectroscopic Telescope Array

The Nuclear Spectroscopic Telescope Array (NuSTAR) is a hard XRT, with two independent detectors known as focal plane module (FPM) A and B, observing between 3–79 keV (F. A. Harrison et al. 2013). We obtained two observations approximately a day apart, with details in Table 10. We reduced the observations with the data reduction software NuSTARDAS v2.1.2, with CALDB v20240520. For each observation, we used the NUPIPELINE task to produce a cleaned event list from each detector. From these event lists, we extract events from a 60″ circular region around the expected source location, and also from a 60″ circular background region located close to the source region on the detector. We report the observed count rates from each region on each detector in Table 10. As none of the detectors showed a clear detection, we use the method of R. P. Kraft et al. (1991) to estimate the 90% upper confidence limit for the number of counts seen by each NuSTAR detector.

3.7. The Low Resolution Imaging Spectrometer

We obtained both optical spectra and photometry for 24puz with the LRIS on the Keck I telescope (J. B. Oke et al. 1995; PI: V. Ravi). The observations are summarized in Table 11.

We centered all observations on the transient location as measured by ZTF. The slit angle was set to parallactic for all observations except MJD 60590, for which we set the angle to $337\overset{\circ}{.}18$ to include the closest galaxy to 24puz that is detected in our Hubble Space Telescope (HST) observations, described later in this section. The slit positions are shown in Figure 3. We used the 400/3400 grism, the 400/8500 grating with central wavelength 7830, and the 560 dichroic. We reduced the observations using the `lpipe` data reduction pipeline (D. A. Perley 2019) with default settings. The final two LRIS epochs had a poor red–blue scaling in the default reduction, so we manually rescaled the red-side spectra to improve the match.

The resulting wavelength range from ∼3100 to 10000 Å, and the resolution $R \approx 700$. Our spectroscopic observations are summarized in Table 11. The slit positions are overlaid on an HST image of the transient in Figure 3.

3.8. The Lowell Discovery Telescope

We obtained observations of 24puz with the Large Monolithic Imager mounted on the 4.3 m Lowell Discovery Telescope (LDT; PI E. Hammerstein) on 2024 August 27. We reduced the LDT data using standard data reduction techniques, including bias subtraction, flat-fielding, and cosmic-ray rejection. We used the Scamp code to align frames and the Swarp code to combine. We flux calibrate using the Pan-STARRS DR2 catalog. The data are summarized in Table 5.

3.9. The Liverpool Telescope

We obtained imaging of 24puz in the *u*, *g*, *r*, and *i* bands with the Liverpool Telescope (LT; PI C. Angus) between 2024 August 5 and 2024 August 20. All raw LT images were reduced using standard reduction techniques, and aperture photometry was performed using the "Photometry Sans Frustration" (`PSF`; M. Nicholl et al. 2023) pipeline, using a PSF optimized aperture and archival images from the Sloan Digital Sky Survey (F. D. Albareti et al. 2017) for template subtraction. The observations are summarized in Table 6.

3.10. The Hubble Space Telescope

We observed 24puz for two orbits with four bands using the Wide Field Camera 3 on the HST on 2024 September 30 (PID 17854, PI Somalwar). The data are summarized in Table 12. We retrieved the reduced data from the `mast` archive. From some basic data quality checks, we concluded that all the default data were sufficient for our analysis, except the IR/F160W image. This image suffered from scattered light, so we followed recommended procedures to manually flag the individual reads that were most affected and then redrizzled the data using recommended parameters.[22]

The transient was significantly detected ($>5\sigma$) in all images, alongside many other sources. We performed aperture photometry for both the transient and all other sources in the image using the `sep` package (K. Barbary 2016; E. Bertin et al. 1996). We first background subtract each image using background boxes of a size $32 \times 32\,{\rm pix}^2$ and a smoothing kernel of $3 \times 3\,{\rm pix}^2$. We also measure the uncertainty in the images using these parameters. We detect sources on the F606W image, because of its combination of resolution and sensitivity. We verify by eye that we are not missing any IR or UV-bright sources because of this choice. We extract sources within 200″ of the transient (1 Mpc at $z = 0.356$) using a 3×3 smoothing kernel and requiring at least 5 pixels above 1.5σ. We measure elliptical kron radii using `sep`. We then perform aperture photometry using the `photutils` package. We use elliptical apertures scaled to twice the kron radii, which should include ∼90% of the enclosed flux for typical galaxies. For the IR images, which have poorer spatial resolutions, we increase the

[21] https://www.cosmos.esa.int/web/xmm-newton/sas-threads

[22] See https://github.com/spacetelescope/WFC3Library/tree/main/notebooks/ir_scattered_light_calwf3_corrections for details.

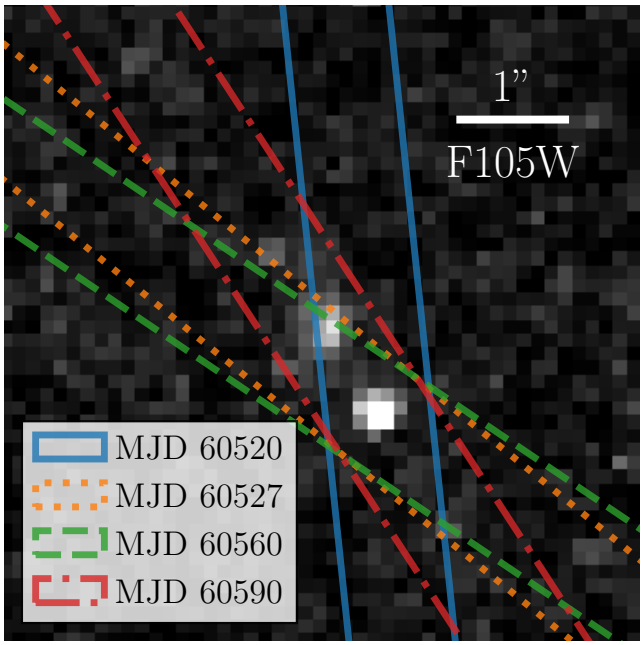

Figure 3. Position angle of the Keck I/LRIS longslit for each observation, overlaid on the HST/WFC3 F105W observation. 24puz is toward the bottom right corner of the image, whereas the galaxy is in the center. The MJD 60590 observation longslit was positioned to include the nearby galaxy and 24puz.

aperture radii by the quadrature difference of the IR and F606W PSFs. We measure the background around each source and the local flux uncertainty using the mean and root-mean-squared error in a circular aperture from 1.″8 to 3″, centered on each source. We reject any source that is not detected at a 3σ level in at least three bands.

For most of the sources in the images, our goal is to measure approximate stellar masses (to be described in Section 4.1) and half-light radii. We measure half-light radii using the `sep flux_radius` function. For the transient, we modify our photometry slightly. We adopt a circular aperture with a radius twice the kron radius. We then correct the photometry in each band for the encircled energy curves provided by MAST.

3.11. The Very Large Array

We observed 24puz with the Jansky Very Large Array (VLA) on MJDs 60539 (2024 August 17; PI Somalwar, Project 24B-456) and 60564 (2024 September 11; PI J. Somalwar, Project 24B-456). The VLA was in B configuration, and we observed in the Ku band (∼15 GHz). We used J1740+5211 as a gain calibrator and 3C286 as a flux calibrator. We followed recommended procedures for high-frequency observations. We manually reduced each epoch using the `casa` package (CASA Team et al. 2022) version 6.5.3.28 following recommended procedures. No source was detected in a 5″ box around the known transient location in either observation. The rms uncertainties were 5.5, 3.8 μJy, respectively. We set 5σ upper limits of <27.5, 19 μJy, respectively, where we adopt the rms measured in a 30″ box.

3.12. The Northern Extended Millimeter Array

We observed 24puz with the Northern Extended Millimeter Array (NOEMA) on MJD 60551 (2024 August 29) at 100 GHz with proposal D24AB (PI: V. Ravi), using a standard continuum setup. We used MWC349 as the flux calibrator, and 1739+522 as the gain calibrator. The observations were reduced using the standard NOEMA pipeline. No source was detected in a 5″ box around the known transient location in either observation, with an rms of 13 μJy. We set a 3σ upper limit of <52, μJy, where we adopt the rms measured in a 20″ box.

4. Data Analysis

In this section, we describe the physical properties of 24puz and its environment that can be inferred from our observations. We begin with constraints on the redshift and host galaxy of 24puz. Then, we consider the transient emission. We first discuss the ultraviolet-infrared lightcurve, followed by the limits on transient optical spectral features, the X-ray lightcurve and spectral evolution, and finally the implications of the radio limits.

4.1. Host Galaxy and Environment

In this section, we identify possible host galaxies of 24puz. We first constrain the redshift of 24puz using the detected ISM absorption lines. Then, we consider whether 24puz is associated with a galaxy (or galaxy overdensity) that is detected in imaging of the field. We finally constrain the possibility that 24puz is associated with an undetected (i.e., faint and/or compact and obscured by the transient) host galaxy.

4.1.1. Optical Spectroscopy: ISM Absorption and Redshift Constraints

In this section, we measure the redshift and equivalent widths of the ISM absorption lines detected in the spectra of 24puz, as shown in Figure 4. We consider the Fe II $\lambda\lambda$2586, 2600, Mg II $\lambda\lambda$2796, 2803, and the Mg I λ2852 lines. We do not detect any Ca absorption. We measure these lines using our spectrum from MJD 60527.3, which is the deepest spectrum we obtained that includes bright transient emission (as required to detect the absorption lines). We fit the spectrum in the regions [2630 Å, 2670 Å] and [2760 Å, 2880 Å], which include a sufficient continuum to perform a local continuum fit around each line. We model the continuum in each region separately as first degree polynomials. We chose these continuum models as the lowest degree polynomials required such that the χ^2/degrees of freedom (dof) was consistent in each region with a p-value >10%. We fit each absorption line as a Gaussian. The Gaussian amplitudes were independent. The widths were tied for lines within doublets, but were otherwise free. We perform the fit using the `scipy` least-squares function and report best-fit equivalent widths and 1σ uncertainties in Table 1. The fit is shown in Figure 4. The best-fit redshift was $z = 0.35614 \pm 0.00009$. The lines are largely unresolved. The χ^2/dof of the final fit was 140/167, for a fully consistent p-value of 0.94.

The Mg II λ2796 equivalent width is $\mathrm{EW}_{2796} = 0.753 \pm 0.104$ Å, placing the absorber in the class of strong absorbers ($W_{2796} \gtrsim 0.3$ Å; C. C. Steidel & W. L. W. Sargent 1992). This gas could originate from the host galaxy of 24puz or from the extended circumgalactic medium of a nearby galaxy/galaxy group. We will discuss these possibilities in the following section.

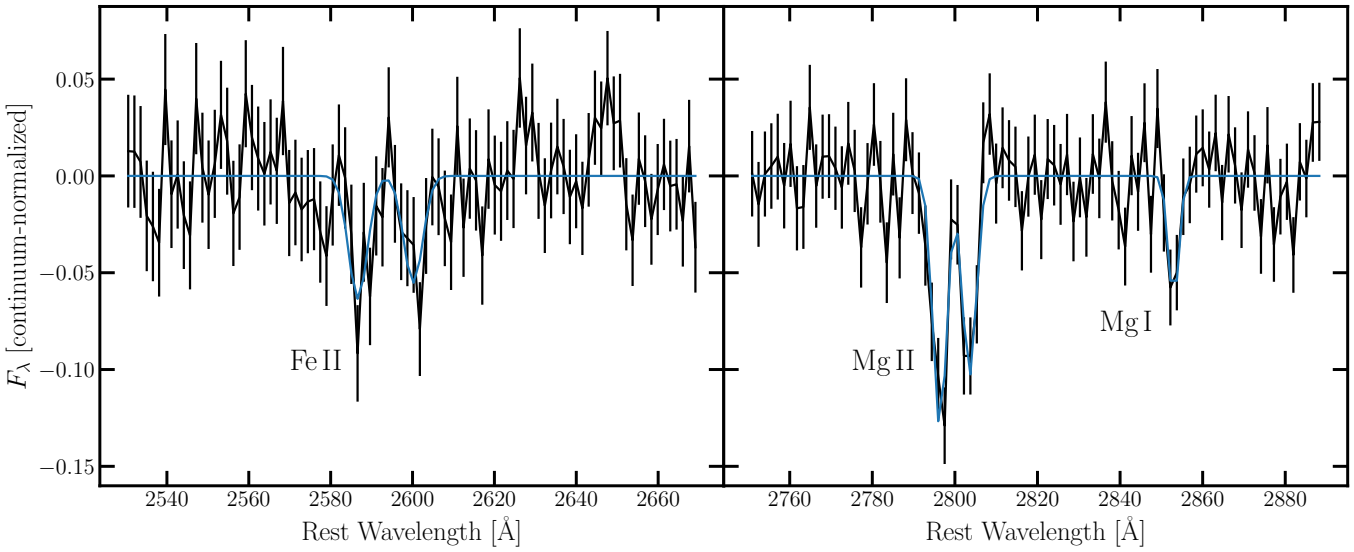

Figure 4. Fits to the absorption lines Fe II λλ2586, 2600, Mg II λλ2796, 2803, and Mg I λ2852. The spectra are fit as linear continuum components and Gaussian lines, as described in Section 4.1.1. The Gaussian widths and redshifts are fixed to the same value for all lines. The best-fit redshift is $z = 0.35614 \pm 0.00009$. The Mg II absorption is consistent with a strong-absorber ($EW_{2796} = 0.753 \pm 0.104$ Å > 0.3 Å), suggesting that this absorption is more likely occurring within the nearest galaxy to 24puz (G1) or a nearby group/cluster.

Table 1
Absorption Line Equivalent Widths

Line	Equivalent Width (Å)
Fe II λ2586	0.502 ± 0.148
Fe II λ2600	0.438 ± 0.14
Mg II λ2796	0.753 ± 0.104
Mg II λ2803	0.599 ± 0.099
Mg I λ2852	0.286 ± 0.098

Note. The line redshifts were tied together in fitting. The line widths were tied together for doublets, but were otherwise allowed to float freely. The best-fit redshift was $z = 0.35614 \pm 0.00009$.

4.1.2. HST Imaging: Nearby Galaxies and Probability of Association

We next consider the galaxies detected in our deep HST imaging of the field of 24puz (zoom-in in Figure 5). We will show that 24puz is likely associated with a detected galaxy, and in the following sections, we will identify and characterize the galaxy that is the most likely host. Henceforth, we will call the nearest galaxy to 24puz in projected distance "G1."

In Appendix B, we show that the probability of 24puz randomly lying at its location relative to G1 is $p_1 = 3 \times 10^{-4}$. We also show that the probability that all the second- through 10th-nearest neighbors being closer than those observed for 24puz is small: $p_{2-10} = 1.3 \times 10^{-3}$. It is thus $\gtrsim 3\sigma$ unlikely that 24puz lies close to the observed galaxies by chance.

Given that the probability of 24puz randomly lying near both the nearest and the second-10th-nearest neighbors is low, 24puz is likely part of a galaxy group or cluster. The closest cataloged galaxy group is centered at a 5.′89 offset and at the spectroscopic redshift $z = 0.354$, corresponding to a 1.8 Mpc projected distance (H. Zou et al. 2021; Z. L. Wen & J. L. Han 2024). This redshift is fully consistent ($<1\sigma$) with the ISM/CGM absorption lines in the spectrum of 24puz at $z = 0.35614 \pm 0.00009$. The reported mass and radius of this structure are $M_{500} = 8.5 \times 10^{13}\, M_\odot$ and $r_{500} = 0.612$ Mpc (Z. L. Wen & J. L. Han 2024). The projected offset between 24puz and this group is large: 1.8 Mpc corresponds to $2.9 r_{500}$. 24puz is well outside the virial radius of the group (note that $r_{200} \approx (1.4\text{–}2) r_{500}$, so the offset is $\sim(1.5\text{–}2) r_{200}$). 24puz may be associated with a structure that is infalling into this group, or it may be unassociated and instead part of a smaller, nearby group that is undetectable in X-ray or spectroscopic group catalogs.

Even though 24puz may not be associated with this group, the Mg II absorber that is detected in our optical spectroscopy could be associated with the group at 1.8 Mpc. If the Mg II absorber is associated with the group, it is possible that we are simply unlucky, and 24puz is a background source at $z \gtrsim 0.356$ that happens to lie along the line of sight of this group. At a 1.8 Mpc $= 2.9 r_{500}$ projected offset from a low-mass cluster, the covering fraction of Mg II absorbers is low: $<1\%$ (A. Anand et al. 2022). It is unlikely that 24puz would happen to lie along such a line of sight, unless it is associated with a structure (e.g., a galaxy) that hosts Mg II absorbers. As we will discuss, 24puz is coincident with a galaxy, so it is feasible that the absorber is within this galaxy (Y.-H. Huang et al. 2021).

Thus, regardless of the precise large-scale structure that 24puz is associated with, we can come to some reasonable conclusions. First, 24puz is unlikely to be randomly associated with the galaxies in the field. Second, the ISM/CGM absorption lines at $z = 0.35614 \pm 0.00009$ are unlikely to be associated with an absorber in the nearby group given the large projected offset, and instead are probably associated with a galaxy or galaxy group closer to 24puz. We can then reasonably assume that 24puz is located within a more nearby galaxy or group, and is thus also at $z = 0.35614 \pm 0.00009$. We adopt the assumption that 24puz is at this redshift for the rest of this work. We briefly discuss the implications of 24puz as a background source in Appendix C.

4.1.3. Host Galaxy Candidates

From the previous section, we have concluded that 24puz is likely hosted by a large-scale structure at $z = 0.35614 \pm 0.00009$. Now, we narrow down the association: 24puz is an object that

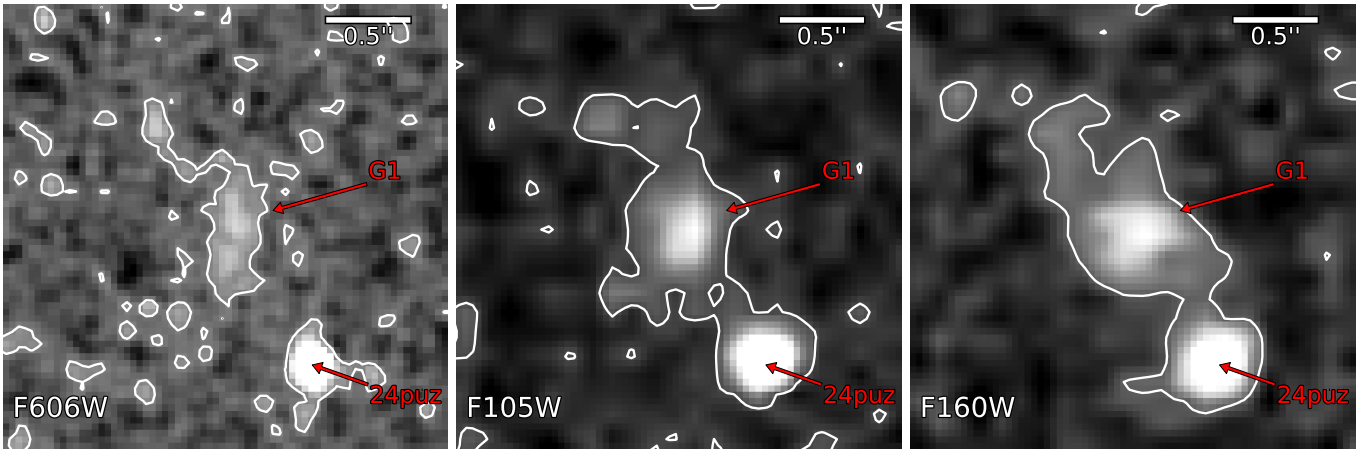

Figure 5. Morphology of the nearest galaxy to 24puz, which we name G1. We show HST/WFC3 imaging of G1 in the F606W (left), F105W (middle), and F160W (right) bands. These images were taken 56 rest-day postdiscovery. We have reprojected all images to the F606W pixel scale for ease of comparison, but this means that the F105W and F160W have been resampled to a smaller pixel scale than the original images. G1 and 24puz are labeled. The white lines show contours, which highlight the morphology of G1. In all bands, there is an extended tidal tail or other irregular component toward the top left of G1. The contour levels are shown for visualization but are not intended to represent σ levels.

either is (1) gravitationally bound to a galaxy, like a star or stationary BH, or (2) ejected, like a recoiling BH or NS. In the former case, we expect 24puz to be within, roughly, the virial radius of its host. In the latter, 24puz may be offset from its host galaxy.

We first consider the case where 24puz is bound to a galaxy. We have named the closest galaxy (in projected distance) to 24puz "G1." 24puz is at a $\sim$5 kpc offset from G1, assuming $z = 0.356$. We model our HST/F606W image of G1 with a Sérsic profile, in addition to a Moffat profile, to represent 24puz. 24puz is located at $\sim$3 projected half-light radii from G1.

In the previous section, we showed that the random association probability with G1 is low ($p_1 = 3 \times 10^{-4}$), assuming a uniform probability of 24puz occurring at any point in the field. The galaxy with the second-lowest-chance association probability has $p_2 = 0.02$, a factor $\sim$70$\times$ higher. If 24puz has a higher probability of occurring within the virial radius of the other galaxies in the field, the probability of chance association with G1 would *decrease*. Thus, even though there are many galaxies within a virial radius of 24puz, G1 is the most likely host.

We next consider the case that 24puz is produced by an astrophysical object that has received a kick velocity after a dynamical event (a merger, binary/triple interactions; e.g., A. Peres 1962; J. D. Bekenstein 1973). In this case, the offset distribution depends on the type of astrophysical object and the process that caused the kick. If 24puz is kicked, but it is still associated with G1, we require a low-velocity kick $\lesssim$100 km s^{-1}: the observed offset is 5 kpc, so for a mean kick velocity v_k, we have a mean delay time $\sim 60\,\mathrm{Myr} \times \frac{v_k}{100\ \mathrm{km\ s^{-1}}}$. Note that G1 is a dwarf galaxy with a low escape velocity $\lesssim$150 km s^{-1}. If the kick velocities are $v_k \gg 100$ km s^{-1} or the delay times $\sim$gigayears, then 24puz cannot be associated with G1. While we cannot exclude this case, the problem of the low probability of chance association with G1 remains. Thus, we still prefer a physical association with G1, and thus a small kick velocity and delay time.

Based on these arguments, we will cautiously associate 24puz with G1 for the rest of this work.

4.1.4. Host Galaxy Physical Properties

In this section, we analyze the photometric properties of G1. For completeness, we also constrain the presence of a stellar overdensity (e.g., a stellar cluster) at the location of 24puz, but the luminous emission from 24puz precludes any strong photometric constraints on the overdensity.

We first consider the morphology of G1. In Figure 5, we show zoom-ins of G1 in the F606W, F105W, and F160W bands. The F606W image is smoothed with a Gaussian kernel of the width 0.9 pix for visualization. All images have been reprojected onto the frame of the F606W image. Contours are overlaid on each image to guide the eye. While the low signal-to-noise of the G1 detection combined with the insufficient resolution in the redder bands precludes quantitative modeling of the structure of G1, the images suggest a faint source detected near G1, which may be connected to G1 via a low surface brightness tail. We cannot confirm this, however, due to the low signal-to-noise of the image: we require deep, space-based follow-up. G1 may be in an interacting pair, have tidal tails, or simply be near a background galaxy. We favor one of the former two scenarios, particularly given the evidence that 24puz is in a galaxy group. The chance association probability of a background galaxy with G1 is even lower than that of 24puz, given the proximity of the candidate background galaxy.

Next, we consider the stellar mass and age of G1. We model the HST photometry of G1, including an upper limit from the F336W band, as a simple stellar population. The lack of wavelength coverage and high signal-to-noise observations prevents more detailed modeling. We use the `prospector` code (C. Conroy et al. 2010; J. Leja et al. 2017; B. D. Johnson et al. 2021). We set a normal redshift prior at $z = 0.35614 \pm 0.00009$. We do not include host galaxy extinction, given the lack of photometric constraints on G1 and the low extinction level implied by the UV/optical spectral energy distribution (SED) of 24puz, but we do include Milky Way extinction with $A_V = 0.1$ mag and $E(B-V) = 0.03$ mag (D. J. Schlegel et al. 1998). We allow the redshift, galaxy age, galaxy metallicity, and galaxy mass to float. We require that the galaxy age is smaller than the age of the Universe at each redshift. We fit the data using the `dynesty` code using the random walk sampling, 400 initial live points, and 200 live points per batch (J. Skilling 2004, 2006; J. S. Speagle 2020).

The results are shown in Figure 6. There are strong degeneracies between the stellar mass, age, and metallicity, but we can draw some conclusions. First, G1 is a dwarf galaxy,

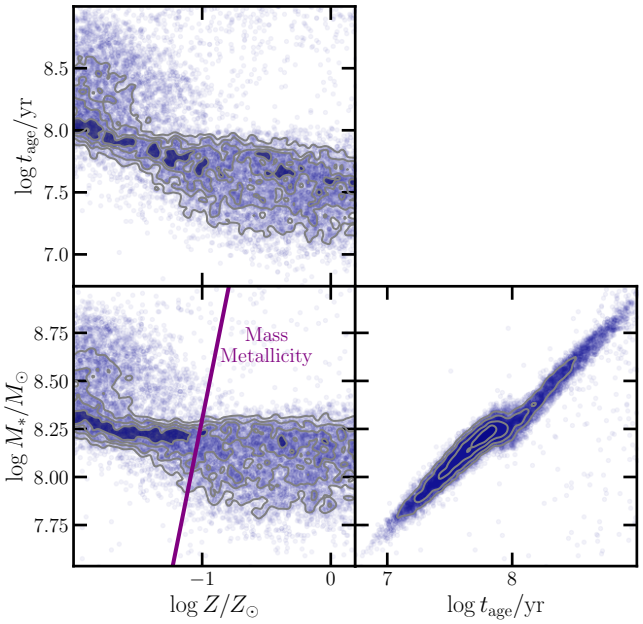

Figure 6. Constraints on the stellar population of G1. We assume a simple stellar population, due to a lack of constraints on the galaxy emission. The corner plot shows the distribution of possible stellar ages (t_{age}), metallicities Z, and stellar masses M_* with gray contours overlaid. The mass–metallicity relation from E. N. Kirby et al. (2013) is shown in dark purple. We find that G1 is a dwarf galaxy with $M_* \lesssim 10^{8.75}\,M_\odot$. If it lies on the mass–metallicity relation, then the mass is $10^{7.75} \lesssim M_*/M_\odot \lesssim 10^{8.25}$, and the age t_{age}/Myr $\sim$ 100 Myr.

with a stellar mass $M_* \lesssim 10^{8.75}\,M_\odot$. If G1 lies on the mass–metallicity relation from E. N. Kirby et al. (2013), then the stellar mass is $10^{7.75} \lesssim M_*/M_\odot \lesssim 10^{8.25}$. In this case, the stellar population age is $10 \lesssim t_{age}/\mathrm{Myr} \lesssim 100$ Myr, although the upper end of this range is preferred.

We briefly consider a stellar population that is hidden beneath the transient emission from 24puz. Because 24puz was still luminous during our HST observations, our constraints are weak. As we will discuss in Section 4.2, however, 24puz shows an evolving red excess. A component, however, could also be produced by a stellar population. We model this by assuming that all the emission in the F105W and F160W bands is produced by stars, with no transient component. This will give us a rough estimate on the maximum mass expected. We use the F336W and F606W constraints on the transient emission as upper limits. We find a 99% mass upper limit $M_* < 10^{8.9}\,M_\odot$; i.e., a compact dwarf galaxy or stellar cluster could be present. Deep, space-based follow-up once the transient emission has faded will be critical for constraining the stellar population at the location of 24puz.

We conclude that G1 is a low-mass dwarf galaxy with a moderately young stellar population. Current constraints on any stars hidden underneath the transient emission allow for a compact dwarf galaxy or stellar cluster, with a mass upper limit $M_* < 10^{8.9}\,M_\odot$.

4.1.5. Star Formation Rate Constraints

We constrain the star formation rate (SFR) at the location of 24puz by constraining the Hα, Hβ, and [O II] $\lambda\lambda$3726, 3729 luminosities from our LRIS spectra. Note that the slits for each spectrum were positioned differently. All the spectra were centered on 24puz and contained fractions of G1. The MJD 60590 (61.4 rest-day) spectrum was positioned to fully cover both 24puz and G1. We will consider each spectrum separately, given the different fractions of G1 included in the slit.

Table 2
Emission Line Fluxes

Date	Δt	$L_{H\alpha}$	$\mathrm{SFR}_{H\alpha}$	$L_{[O\,II]}$	$\mathrm{SFR}_{[O\,II]}$
2024-07-29	60,520.4	<3.04	<0.09	<2.62	<0.17
2024-08-05	60,527.3	<1.44	<0.04	<1.0	<0.07
2024-09-07	60,560.3	<0.65	<0.02	<0.19	<0.01
2024-10-07	60,590.2	<1.56	<0.05	$0.15^{+0.05}_{-0.05}$	$0.01^{+0.003}_{-0.003}$

Note. Line emission and star formation rate constraints. All luminosities are in units 10^{40} erg s^{-1}, and star formation rates in units $M_\odot$ yr^{-1}. Δt gives rest-frame day postdiscovery.

We fit each spectrum after continuum subtraction. We model the continuum by convolving each spectrum with a Gaussian kernel of the width 50 pixels and subtracting this from the spectrum. We fit Hα and Hβ simultaneously because they are expected to have correlated luminosities: we fit for the Hα luminosity, denoted L_α, and fix the Hβ luminosity $L_\beta = L_\alpha/2.86$, where we have adopted the theoretical Balmer decrement commonly assumed for star formation (computed assuming photoionized gas at temperature 10^4 K; D. E. Osterbrock & G. J. Ferland 2006). This Balmer decrement assumes no host galaxy extinction. We separately fit a Gaussian at the locations of [O II] $\lambda\lambda$3726, 3729, and we tie the doublet ratio to be $L_{3726}/L_{3729} = 0.35$ (D. E. Osterbrock & G. J. Ferland 2006). We allow the widths of the lines to vary between $\sigma_v \in [90, 600]$ km s^{-1}. We assume a redshift $z = 0.356$ but allow the line centroids to vary by $\Delta_v \in [-150, 150]$ km s^{-1}. These velocities are assumed to be the same for the Balmer lines but are allowed to be different for [O II] $\lambda\lambda$3726, 3729. We adopt a linear model to absorb any residual continuum. We fit regions of each spectrum corresponding to 10^4 km s^{-1} around each relevant line. We use the `emcee` sampler with default settings to perform the fit independently for each spectrum (D. Foreman-Mackey et al. 2013). We used 200 walkers and 7000 burn-in steps, followed by an additional 5000 steps. We thinned the resulting chains by a factor of 13.

The fit results are summarized in Table 2 and Figure 7. The only 3σ line detection was [O II] $\lambda\lambda$3726, 3729 in the MJD 60590 (61.4 rest-day) spectrum. Assuming that the [O II] luminosity correlates with SFR as $\mathrm{SFR} = 6.58 \times 10^{-42} \mathrm{L([O\,II])}/(\mathrm{erg\,s^{-1}})$ (L. J. Kewley et al. 2004), we find that this detection corresponds to an SFR $\mathrm{SFR} = 0.01^{+0.003}_{-0.003}\,M_\odot$ yr^{-1}, or a specific SFR sSFR $\approx 10^{-10}$ yr^{-1}. This detection is consistent with the Balmer upper limit and the upper limits from every other spectrum. Extrapolating to low stellar masses from the star-forming main sequence at $z = 0.356$ measured by J. Leja et al. (2022), we find that this emission is below the star-forming main sequence (see the right panel of Figure 8), although it is within $\sim 2\sigma$ of the measured spread (extrapolated by eye from Figure 3 of J. Leja et al. 2022).

Note that the significance of the [O II] $\lambda\lambda$3726, 3729 detection is somewhat sensitive to the prior on the line width. We tested increasing the prior to a maximum of 3000 km s^{-1} (which is unphysically broad), the significant decreases to $\sim 2.5\sigma$, so we consider this line a marginal detection. The conclusion that the star formation rate is below the star-forming main sequence is still robust.

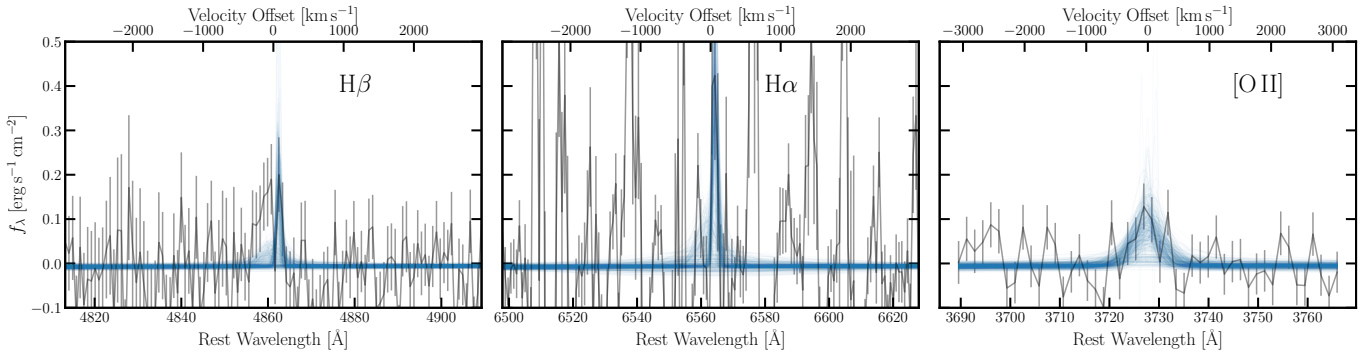

Figure 7. Emission line fits to the optical spectrum of 24puz from MJD 60590.2, or 61.4 rest-day postdiscovery. Fits to Hβ, Hα, and the [O II] $\lambda\lambda$3726, 3729 doublet are shown in the left, middle, and right panels, respectively. The data is shown in black. The amplitudes of the Balmer lines are tied to the expected ratio for star formation, and the ratio of the [O II] doublet amplitudes are likewise tied. The apparent line at the location of Hβ is a sky subtraction artifact—rereducing the spectrum with different sky subtraction algorithms removes this feature. The [O II] line, on the other hand, is robust to sky subtraction. Blue lines show samples from our Gaussian `emcee` fits.

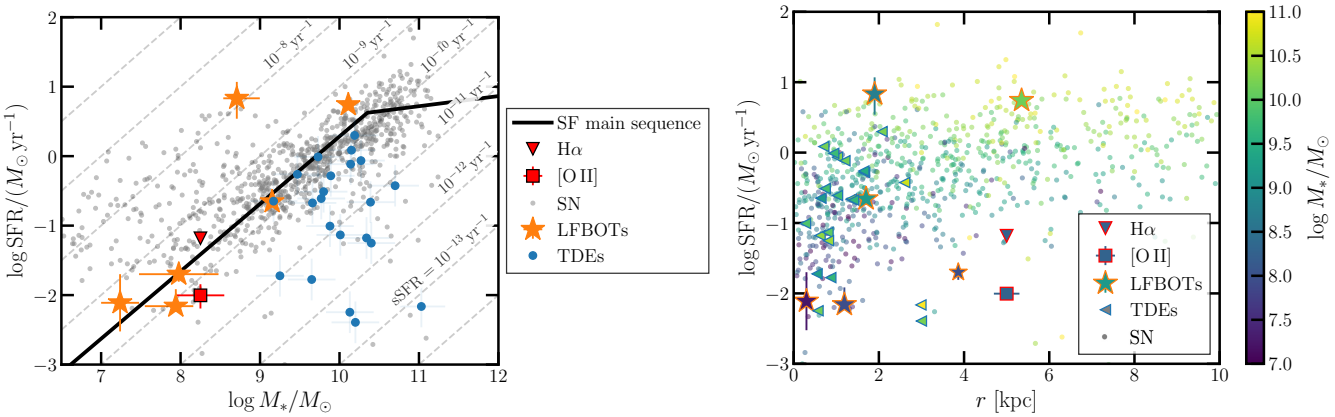

Figure 8. Left: star formation versus stellar mass of G1 relative to other galaxy populations. Constraints from the optical spectroscopy of G1 are shown in red. LFBOT hosts from D. A. Perley et al. (2019, 2021), D. L. Coppejans et al. (2020), A. A. Chrimes et al. (2024a), Y. Yao et al. (2022), and A. Y. Q. Ho et al. (2020) are shown in orange, and TDE hosts from Y. Yao et al. (2023) in blue. The core-collapse supernova host galaxy sample from S. Schulze et al. (2021) is shown in gray. Lines of constant specific star formation rate (sSFR) are shown in gray dashed. 24puz lies below the star-forming main sequence. Its location is consistent with LFBOT host galaxies, but is at a low sSFR and stellar mass relative to core-collapse supernova hosts and a low stellar mass relative to TDE hosts. Right: star formation versus physical offset from host galaxy of 24puz relative to other populations. The format is the same as in the left panel, except that we have colored the points by their stellar mass but left the marker outline colors the same as in the left panel. For TDEs, we assume a host galaxy offset $<0\farcs6$. The LFBOT AT 2020xnd does not have a reported offset, so we assume that it is $\lesssim 1''$, based on a by-eye approximation from images in D. A. Perley et al. (2021). 24puz is at a larger offset than expected from its host galaxy mass, if it is associated with a star-forming region.

We conclude that G1 is located below the star-forming main sequence, and there is no evidence for strong star formation at the location of 24puz.

4.2. Broadband UVOIR Lightcurve

We modeled the broadband transient emission from ultraviolet through infrared (UVOIR) wavelengths as evolving blackbodies. We find a statistically consistent fit at all epochs without including extinction within the host galaxy. We use the `dynesty` nested sampler with default settings (J. S. Speagle 2020). We adopt uninformative Heaviside priors on the temperature T_{bb} and radius R_{bb}: $\log T_{bb}/\mathrm{K} \in [3, 5]$ and $\log R_{bb}/\mathrm{cm} \in [12, 17]$. We report the best-fit parameters and computed luminosities L_{bb} and absolute g-band magnitudes M_g in Table 13.

The final two epochs of observations showed an infrared excess above a single blackbody fit, so we require a second component. We consider three models: (1) a second blackbody (e.g., warm gas), (2) an absorbed, dusty blackbody, where the absorption is assumed to be caused by graphite grains, and (3) a power law, defined as $f_\nu \propto \nu^{-\Gamma}$. As we will discuss, these choices are motivated by similar excesses in observations of LFBOTs and TDEs (R. Margutti et al. 2019; D. A. Perley et al. 2019; Y. Chen et al. 2023b; B. D. Metzger & D. A. Perley 2023). For the blackbody models, we report infrared luminosities integrated across all wavelengths. For the power-law model, we integrate from 2000 to 10^7 Å to compute the luminosity, to match previous work (Y. Chen et al. 2023b). We will discuss the red excess and these models in more detail in Section 5.1.2.

All fits are shown in Figure 16, and best-fit parameters are in Table 13. The luminosity, radius, and temperature evolution are shown in Figure 9. The luminosity rises over a ∼day timescale and then approximately plateaus or slowly rises, with a mean value of $\log L_{\mathrm{peak,OptUV}} = 10^{44.79\pm0.04}$ erg s^{-1}. After ∼12 days (rest frame), the luminosity drops as t^{-3}, although note that this slope is sensitive to the best-fit luminosity from our HST observations, which showed a significant red excess for which the appropriate model is uncertain, as we will discuss. The radius is consistent with expanding at $v = (0.082 \pm 0.02)c$ to a peak of $\log R_{\mathrm{OptUV}}/\mathrm{cm} = 15.33 \pm 0.04$ at 5.9 rest-day postdiscovery. Alternatively, the radius expansion may be a power-law

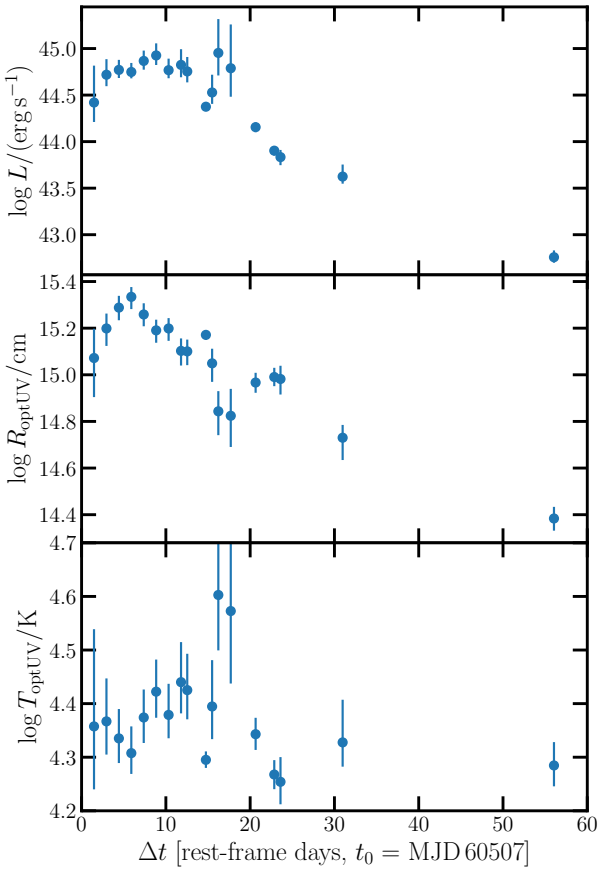

Figure 9. The evolution of the best-fit blackbody parameters to the optical/UV photometry of 24puz. The blackbody luminosity, radius, and temperature are shown in the top, middle, and bottom panels, respectively. The luminosity rapidly rises over a few days, then slowly rises/plateaus before rapidly decaying. The radius expands at a velocity of $0.1c$ or a power law $\sim t^{0.4}$ and then decays as $t^{-1.3}$ after a ∼week. The temperature is largely constant, and the weighted-mean value is $\log T_{\mathrm{bb}}/\mathrm{K} = 4.32 \pm 0.14$.

$\log R_{\mathrm{OptUV}}/\mathrm{cm} \propto t^{0.4}$. The temperature shows slight evolution, but is relatively constant at $\log T_{\mathrm{OptUV}}/\mathrm{K} = 4.32 \pm 0.14$. The error is driven by the standard deviation of the measured temperatures around the mean rather than measured error bars, implying that the temperature does evolve slightly.

4.3. Transient Spectral Features

We constrain narrow ($\lesssim$3000 km s^{-1}) transient features. We do not consider broad spectral features, other than to note that none are apparent by eye in any of our optical spectra (top right panel of Figure 1). We focus on narrow, transient Balmer Hα and Hβ lines, as these are sometimes observed at late-times from optical transients, as we will discuss later. These constraints are identical to those from our star formation constraints on these lines in Section 4.1.5, but we allow the line widths to range from $\sigma_v \in [0, 0.01c]$. We also fit Hα and Hβ independently, as transient spectral features need not be photoionized, and so, the Balmer decrement can vary from the nominal value ∼3. The resulting luminosity constraints are shown in Table 3. No significant emission is detected.

4.4. X-Ray Lightcurve and Spectrum

We constrained the X-ray evolution of 24puz using our Swift/XRT, XMM-Newton, and NuSTAR observations. We adopt a Milky Way hydrogen density $n_{\mathrm{H}} = 2.88 \times 10^{20}\,\mathrm{cm^{-2}}$ and report integrated fluxes in the observed energy band 0.3–10 keV everywhere (N. Ben Bekhti et al. 2016). We first constrained the spectral shape using our first XMM-Newton/EPIC-PN observation (MJD 60536, 21.4 rest-days). We modeled the spectrum using the `xspec` tool with Wilm abundances (J. Wilms et al. 2000), Vern cross sections (D. A. Verner et al. 1996), and W statistics (W. Cash 1979). The spectrum was best modeled as a power law (`tbabs*zashift*tbabs*cflux*powerlaw`, total W statistic 67.87 for 88 dof) rather than a blackbody (`tbabs*zashift*cflux*bbody`, total W statistic 146.92 for 88 dof), so we adopt the power-law model for all epochs. We run a length 300,000 Markov Chain Monte Carlo (MCMC) using `xspec` and the Metropolis-Hastings algorithm with a temperature of 50 to fully sample the parameter space. The best-fit power law and a corner plot showing the best-fit parameter range are shown in the top panels of Figure 10.

The best-fit power-law index is $\Gamma = 1.73^{+0.10}_{-0.09}$. The spectral modeling prefers no intrinsic absorption, with a 3σ upper limit $n_{\mathrm{H}} \lesssim 2 \times 10^{21}\,\mathrm{cm^{-2}}$.

We also tested a Bremsstrahlung model and note that it is consistent with our spectrum (`tbabs*apec`, cash statistic 77.63 for 88 dof), but not preferred over the power-law model. The best-fit temperature is 7.0 ± 1.5 keV. This temperature is low for typical interactions, which produce a forward shock at $\sim 10^9$ K, or 100 keV (C. Fransson et al. 1996). This temperature may be consistent with emission from the reverse shock, but the reverse shock is expected to be highly absorbed due to rapid (subday) cooling in the postshock region (see Table 1 of C. Fransson et al. 1996), and so will not dominate the emission. The best-fit normalization corresponds to a volume emission measure $\int n_e n_H dV = (3.29 \pm 0.17) \times 10^{66}\,\mathrm{cm^{-3}}$. Assuming a spherical emitting region with a radius $\sim 10^{15}$ cm, this corresponds to a high average density $\sim 10^{10}\,\mathrm{cm^{-3}}$. This analysis will become relevant when we discuss possible shock origins of the X-ray emission in Section 5.1.3.

Our second epoch of XMM-Newton observations ($\Delta t = 37.6$ rest-days) is tentatively softer than the first epoch. We model this epoch as an unabsorbed power law (`tbabs*zashift*cflux*powerlaw`, W statistic 28.31 for 26 dof), given the lack of evidence for absorption in the first epoch. The results are shown in Figure 17 in Appendix E, and we find a 1% chance that the photon-index is consistent with the first epoch $\Gamma \leqslant 1.73$. This tentatively suggests that the photon-index softened with time. Following the same procedure, the final XMM-Newton observation was best modeled with $\Gamma = 1.5 \pm 0.3$, which is consistent with both the first and second epochs.

Given that the evidence for evolution in the photon-index is tentative, we construct a lightcurve with better constrained fluxes by simultaneously fitting all epochs together with a

Table 3
Intermediate Width Balmer Line Constraints

Date	MJD	$L_{\mathrm{H}\alpha}$	$L_{\mathrm{H}\beta}$
2024-07-29	60520.4	<4.28	<4.53
2024-08-05	60527.3	<2.26	<3.64
2024-09-07	60560.3	<1.3	<0.12
2024-10-07	60590.2	<2.85	<2.34

Note. All luminosities are in units 10^{40} erg s^{-1}.

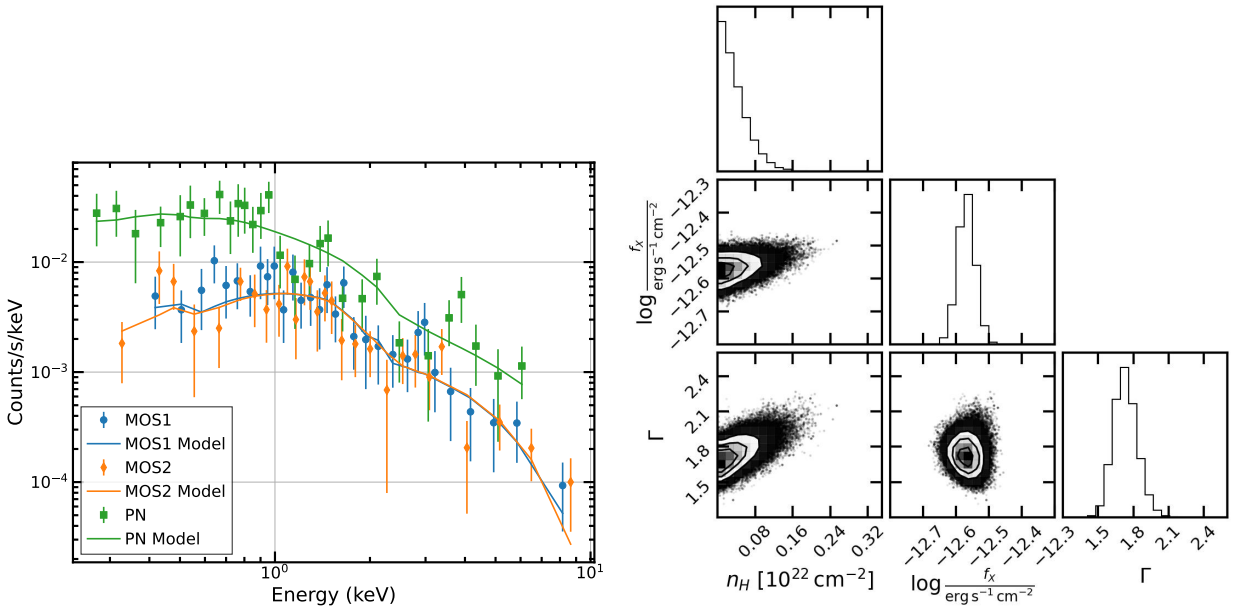

Figure 10. Left: the MJD 60536 (21.4 rest-day) XMM-Newton spectrum of 24puz (blue scatter) with the best-fit power-law model overlaid. Right: corner plot showing the best-fit power-law parameters. The host galaxy absorption is negligible ($n_{\rm H} \lesssim 3 \times 10^{21}$ cm^{-2}). The power-law index is $\Gamma = 1.73^{+0.10}_{-0.09}$.

constant photon-index, following the same procedure as above in `xspec`. Likewise, we convert the NuSTAR and Swift/XRT observations into X-ray fluxes, assuming that the underlying spectrum is an unabsorbed power law with a photon-index of 1.7. The resulting lightcurve is shown in the bottom left panel of Figure 1. We verify that our conclusions do not change if we separately fit the photon indices.

The soft X-ray emission is luminous and highly variable. The peak luminosity detected was in the 21.4 rest-day postdiscovery XMM-Newton observation, with $L_X = 10^{44.12\pm0.034}$ erg s^{-1}. By stacking the Swift/XRT observations at 20.6 and 23.2 rest-days, we obtain a 3σ upper limit of the luminosity $L_X < 10^{43.8}$ erg s^{-1}. Our most luminous detection at 21.4 rest-days (i.e., in between the Swift data points) is 6σ higher than the Swift upper limit. 24puz was variable at a factor of $3.8^{+5.5}_{-1.5}$ assuming normally distributed fluxes (3σ limit >1.3) on $\sim$3 day timescales in the soft X-ray. The NuSTAR upper limits exclude any luminous hard emission component.

4.5. Radio-millimeter Emission

24puz was not detected in any of our radio or millimeter observations. Motivated by radio observations of similar transients, as we will discuss in the following section, we constrain the circumtransient medium under the assumption that any radio emission is produced by a nonrelativistic, wide-angle outflow colliding with a dense medium. Radio emission in this scenario is generally produced by the synchrotron mechanism, with possible contributions from bremsstrahlung. We follow G. B. Rybicki & A. P. Lightman (1986) closely in this section.

We consider an electron with Lorentz factor γ and pitch angle θ in a region of uniform density (n) and magnetic field (B). The synchrotron frequency of this electron is $\nu_s = \frac{eB\gamma^2}{2\pi m_e c}$, where e is the electron charge, m_e is the electron mass, and c is the speed of light. The synchrotron power for this electron is given by

$$P_s(\nu|B,\,\gamma,\,\theta) = \frac{\sqrt{3}\,e^3 B\sin\theta}{m_e c^2} = F(\nu/\nu_c), \quad (1)$$

where $\nu_c = 3/2\nu_s \sin\theta$, $F(x) = x\int_x^\infty K_{5/3}(y)dy$, and $K_{5/3}(y)$ is the modified Bessel function of the order 5/3.

For a population of electrons, the synchrotron spectrum is computed by summing Equation (1) over all electrons. We adopt the standard assumption of a population of electrons with Lorentz factors drawn from a power law with the index p: $N(\gamma)d\gamma = N_0\gamma^{-p}d\gamma$. We adopt the approximation of $F(x)$ used in J. J. Somalwar et al. (2023), which allows Equation (1) to be analytically integrated for a power-law electron distribution with small errors relative to numerically integrating $K_{5/3}(y)$.

Let the system volume be given by V, where for a spherical region of the radius R and filling factor f_V we have $V = 4/3\pi f_V R^3$. The total energy in the system is given by E. Then, the total energy stored in the magnetic field is $E_B = \frac{B^2 V}{8\pi}$. We adopt the equipartition assumption, such that the total energy stored in the magnetic field E_B is a fixed fraction of the total energy of the system: $\epsilon_B = E_B/E$. Likewise, the total energy stored in the electrons, $E_e = \frac{N_0 m_e c^2}{(p-2)\epsilon_e}$ is a fixed fraction of the total energy $\epsilon_e = E_e/E$. This assumption allows us to reduce the number of free parameters in the system. We adopt the common assumption that $\epsilon_B = 0.01$ and $\epsilon_E = 0.1$ (R. Margutti et al. 2019).

Thus, given a magnetic field, radius, and electron energy distribution index p, we can compute the expected synchrotron luminosity at each frequency. The postshock density, in the strong shock regime, is given by

$$n_e = \frac{B^2}{6\pi\epsilon_B m_p v^2}, \quad (2)$$

where we have defined the shock velocity v, which we assume is the average velocity $v = R/t$ given a radius R and a time

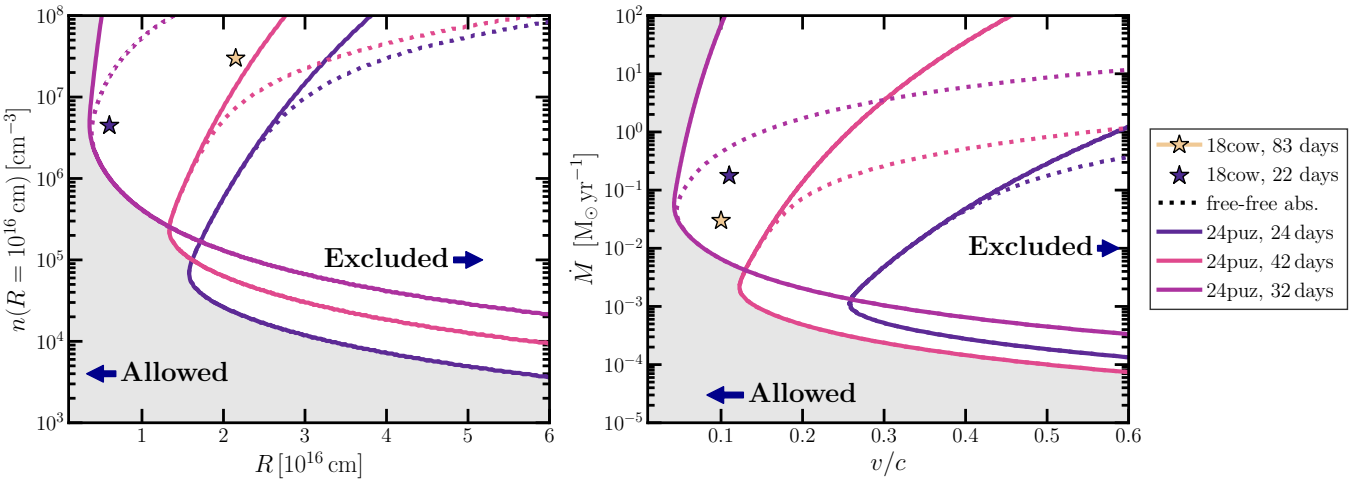

Figure 11. Constraints on the physical parameters of any synchrotron-emitting region from our radio/millimeter observations. The left panel shows the ambient medium density n at outflow radius R for a spherical, nonrelativistic outflow. The dashed lines mark the boundary between physical parameters excluded and allowed by a model that includes free–free absorption, where the absorbing medium density is assumed to be the same as the emitting region. The gray region is allowed by all models. Each line corresponds to a different observation, and the color scales with the time since discovery. The solid lines do not include free–free emission. Regions to the left of these lines are allowed, while regions to the right are excluded. The LFBOT AT 2018cow is shown in stars for comparison (A. Y. Q. Ho et al. 2019; R. Margutti et al. 2019). The right panel is in the same format as the left, but it shows physical parameters appropriate for a stellar-wind-like circumtransient medium. The x-axis shows velocity v, and the y-axis the mass-loss rate $\dot{M}$.

since launch t. Whenever we discuss density in the rest of this section, we refer to this postshock density.

In some cases, we must also include free–free absorption. The free–free optical depth is given by (B. T. Draine 2011, Equation (10.13))

$$\tau_{ff} = \sqrt{\frac{2\pi}{3m_e^3 k_B T_e}}\frac{4e^6}{3hc\nu^3} \times (1 - e^{-\frac{h\nu}{k_B T_e}}) Z_i^2 g_{ff}(\nu, T_e, Z_i) \int n_i n_e dl. \quad (3)$$

We have defined the electron temperature T_e, the number of electrons per ion Z_i, the frequency ν, the ion density n_i and the electron density n_e, and the Gaunt factor $g_{ff}(\nu, T_e, Z_i)$. We approximate the Gaunt factor following Section 10.2 of B. T. Draine (2011). All other variables follow a common notation for constants (e.g., electron mass m_e). The final integral is over the line of sight and is the emission measure $\mathrm{EM} = \int n_i n_e dl$. We adopt the common assumptions $Z_i = 1$ and $n_i = n_e$. We adopt a temperature of $T_e = 10^5$ K, which is higher than the standard photoionization equilibrium temperature due to Compton heating by hard X-ray photons. This is justified in Appendix F.

We assume the density profile is $\sim r^{-2}$, such that the emission measure is $EM = \int_R^\infty n_e n_i dl = n_e^2 R/3$. As we will discuss in Section 5.1.1, our modeling of the optical/UV emission as a shock prefers a shallower density profile $\sim r^{-1}$ in the inner regions of the circumtransient medium ($R \lesssim 10^{15}$ cm). If the outer density profile is similarly shallow, the emission measure will increase by a factor of $\sim$3 (assuming the outer radius is large enough that integrating to infinity causes minimal errors). This does not change our conclusions.

In Figure 11, we show the postshock density from the 24puz upper limits. We treat each observation independently. In the left panel of this figure, we show the upper limit on the radius (x-axis) for a range of assumed densities. The dashed lines include free–free absorption, while the solid lines only include synchrotron self-absorption. The shaded region is allowed by all observations. The right panel shows the same results but in variables appropriate for stellar winds. We assume a wind-like density profile $\rho = \dot{M}/(4\pi v r^2)$. We convert the radius to the average velocity for each epoch. The plot is otherwise formatted the same as the left panel.

The observations allow for a nonrelativistic outflow colliding with a dense medium. A faster outflow is allowed for low densities $\lesssim 10^4\,\mathrm{cm}^{-3}$ or very high densities $\gtrsim 10^9\,\mathrm{cm}^{-3}$, although note that we are not consistently treating relativistic effects.

5. Results

As detailed in the previous section, our observations have shown the following:

1. 24puz is most likely associated with G1, a dwarf galaxy ($10^{7.74} \lesssim M_*/M_\odot < 10^{8.25}$ assuming a standard mass–metallicity relation) that is located slightly below ($\lesssim$1 dex) the star-forming main sequence. 24puz is 5 kpc offset from G1 and shows no evidence for star formation or a massive stellar structure ($\lesssim 10^9\,M_\odot$) at its location, although space-based follow-up once 24puz has faded is critical for tighter constraints. Both 24puz and G1 are most likely at $z = 0.35614 \pm 0.00009$, based on the detection of ISM or CGM absorption lines, and may be bound to or infalling into a galaxy group. G1 shows tentative evidence for irregularities that could suggest a merger or environmental stripping, but deep imaging is required to confirm that the irregularities are not a background galaxy.
2. 24puz produced a luminous UVOIR flare. The flare is well modeled as a single blackbody in observations from 1.5 to 27 rest-day postdiscovery. The emission peaks at a luminosity $L_{\mathrm{OptUV}} = 10^{44.79\pm0.04}\,\mathrm{erg\,s}^{-1}$ after a short, day-timescale rise. The luminosity stays near this value for $\sim$12 days and then decreases rapidly, as $\sim t^{-3}$. The

emitting region radius initially expands rapidly as a power law or constant velocity ($v = (0.082 \pm 0.02)c$) to a maximum radius of $R_{\rm OptUV} = 10^{15.33\pm0.04}$ cm. The temperature of the emitting region is relatively constant at $T_{\rm OptUV} = 10^{4.3\pm0.1}$ K. At 31 rest-days, a near-infrared excess is detected, which is more significantly detected at 56 rest-days. A similar excess could have been present at earlier times, but the hot optical/UV emission dominate.

3. 24puz is a luminous, highly variable, soft X-ray source. The peak X-ray luminosity observed was $L_X = 10^{44.12\pm0.034}$ erg s^{-1} at 21.4 rest-days. At this time, the photon-index was $\Gamma = 1.73^{+0.10}_{-0.09}$ with low intrinsic absorption $n_{\rm H} \lesssim 3 \times 10^{21}$ cm^{-2}. There is tentative evidence for a softer photon-index in the 37.6 rest-day spectrum, with a p-value $\sim 1\%$ that this spectrum has the same photon-index as at the peak. The X-ray emission is variable on $\sim$3 day timescales by a factor of $3.8^{+5.5}_{-1.5}$ (3σ limits >1.3). For the spectrum at the peak, a power-law model is preferred over a blackbody or Bremsstrahlung. Bremsstrahlung emission can fit the observations, but the implied temperature (7 ± 1.5 keV) is too low for typical emission from a forward shock.
4. 24puz is nondetected at 15 and 100 GHz (observer frame). If an outflow was launched, the circumtransient material must have either a density below $\sim 10^5$ cm^{-3} if the average velocity is $\gtrsim 0.1c$ or a higher density but an average velocity $\lesssim 0.1c$.

In the rest of this section, we discuss the structure, physics, and energetics of the emitting regions and compare to published classes of transients.

5.1. Energetics and Emitting Region Scales

The optical/UV photosphere is observed at radii from (0.25 to 1.6) $\times 10^{15}$ cm. Numerically integrating the blackbody luminosity over time, we find a total emitted energy from 0 to 55 rest-frame day postdiscovery of $1.4^{+0.7}_{-0.2} \times 10^{51}$ erg. In the case where this is an accretion energy, which we will consider, the accreted mass is $7.7 \times 10^{-3}\,M_\odot$ for a radiative efficiency of 10% (note that this efficiency is often lower for super-Eddington accretion, as will become relevant later; Y. F. Jiang et al. 2014; J. C. McKinney et al. 2015; E. Takeo et al. 2019; Y.-F. Jiang & L. Dai 2024). This energy does not include contributions from the red excess observed in later epochs, but total energy emitting in this red excess is small relative to that emitting in the optical/UV. If we assume that the red excess luminosity traces the optical/UV (as we have the best evolution constraints in this band), then the excess energy emitting at redder wavelengths is $\sim$10% of that at optical/UV wavelengths.

The variability of the X-ray emission sets a weak limit on the size of the emitting region $\lesssim$3 light days $= 8 \times 10^{15}$ cm. It is plausible that the X-ray emitting region is much more compact and associated with the central engine that is ionizing the UV-infrared emitting regions, in which case the emitting region size must be smaller than that of the optical emitting region. The total energy detected in the X-rays is $\gtrsim 4 \times 10^{49}$ erg. We computed this value by fitting a power law in time to the first and last X-ray detections and integrating. This is a lower limit because of the high variability, which is not included in this estimate, and because we integrate over the 0.3–10 keV range. From the variability alone, the real energy could be a factor $\sim$4 higher. We estimate the energy in the X-rays to be $\sim$4%–16% of the optical/UV energy.

The lack of transient optical spectra features implies that the optical-infrared emitting region is fully ionized, or that the emitting region density profile rapidly steepens above the photosphere so that the line-forming region is small. Given the luminous UV emission and the sizes of the regions stated above, either is feasible.

5.1.1. The Optical/UV Emission

We first consider the origin of the optical/UV flare. We rule out a transient powered by ^{56}Ni decay, following the same logic as R. Margutti et al. (2019) used for the LFBOT AT 2018cow. The ^{56}Ni mass can be constrained in two ways: first, from the optical/UV peak luminosity and, second, from the rise time. From W. D. Arnett & D. W. Arnett (1982), the rise time $t_{\rm rise}$ can be approximated as the diffusion time $t_{\rm dif}$

$$t_{\rm rise} \approx t_{\rm dif} \approx \left(\frac{M_{\rm ej}\kappa}{4\pi v_{\rm ej} c}\right)^{1/2} = 10\ {\rm days}\left(\frac{M_{\rm ej}}{4.3\,M_\odot}\right)^{1/2}\left(\frac{v_{\rm ej}}{0.1c}\right)^{-1/2}, \quad (4)$$

where $\kappa = 0.1$ cm^2 g^{-1} is the effective opacity, $v_{\rm ej}$ is the ejecta velocity, and $M_{\rm ej}$ is the ejecta mass. The peak bolometric luminosity is given by (K. D. Nadyozhin 1994)

$$L_{\rm bol} = \frac{M_{\rm Ni}}{\tau_{\rm Co} - \tau_{\rm Ni}}\left\{\left(Q_{\rm Ni}\left(\frac{\tau_{\rm Co}}{\tau_{\rm Ni}} - 1\right) - Q_{\rm Co}\right)e^{-\frac{t}{\tau_{\rm Ni}}} + Q_{\rm Co}e^{-\frac{t}{\tau_{\rm Co}}}\right\} = \frac{M_{\rm Ni}}{M_\odot}(6.45e^{-\frac{t}{8.8\ {\rm days}}} + 1.45e^{-\frac{t}{111.3\ {\rm days}}})10^{43}\ {\rm erg\ s^{-1}}, \quad (5)$$

where $\tau_{\rm Co} = 111.3$ days is the half-life of ^{56}Co, and $\tau_{\rm Ni} = 8.8$ days is the half-life of ^{56}Ni, $Q_{\rm Ni} = 1.75$ MeV and $Q_{\rm Co} = 3.73$ MeV are emitted energies per decay, and t is the time since the initial event. $M_{\rm Ni}$ is the nickel mass. To reproduce the peak optical/UV luminosity of 24puz, we thus require a large ^{56}Ni mass of $\sim 30\,M_\odot$. This contradicts constraints from the lightcurve rise time, which would correspond to the diffusion time. The ejecta mass required for a $\lesssim$10 day rise with an ejecta velocity of $0.1c$, as implied by the optical/UV photosphere, is $\lesssim 4\,M_\odot$. The kinetic energy of this ejecta mass is large at 4×10^{52} erg.

We next consider an accretion-powered flare, where gas surrounding a central source reprocesses high-energy emission to produce the optical/UV flare. Motivated by the similarity of this transient to TDEs that we present in Section 6, we first tested this origin using the `MOSFIT` code to model the optical/UV emission from 24puz as a TDE-like accretion flare (J. Guillochon et al. 2018; B. Mockler et al. 2019). `MOSFIT` is based on a grid of hydrodynamical simulations of simulated disruptions of a $1\,M_\odot$ star by a $10^6\,M_\odot$ SMBH, which are then scaled to other stellar and BH parameters using analytic relations. The luminosity is assumed to trace the fallback rate measured from these simulations, but with delays from the time for the debris to circularize into an accretion disk, as well as the viscosity in that accretion disk. The accretion-power is

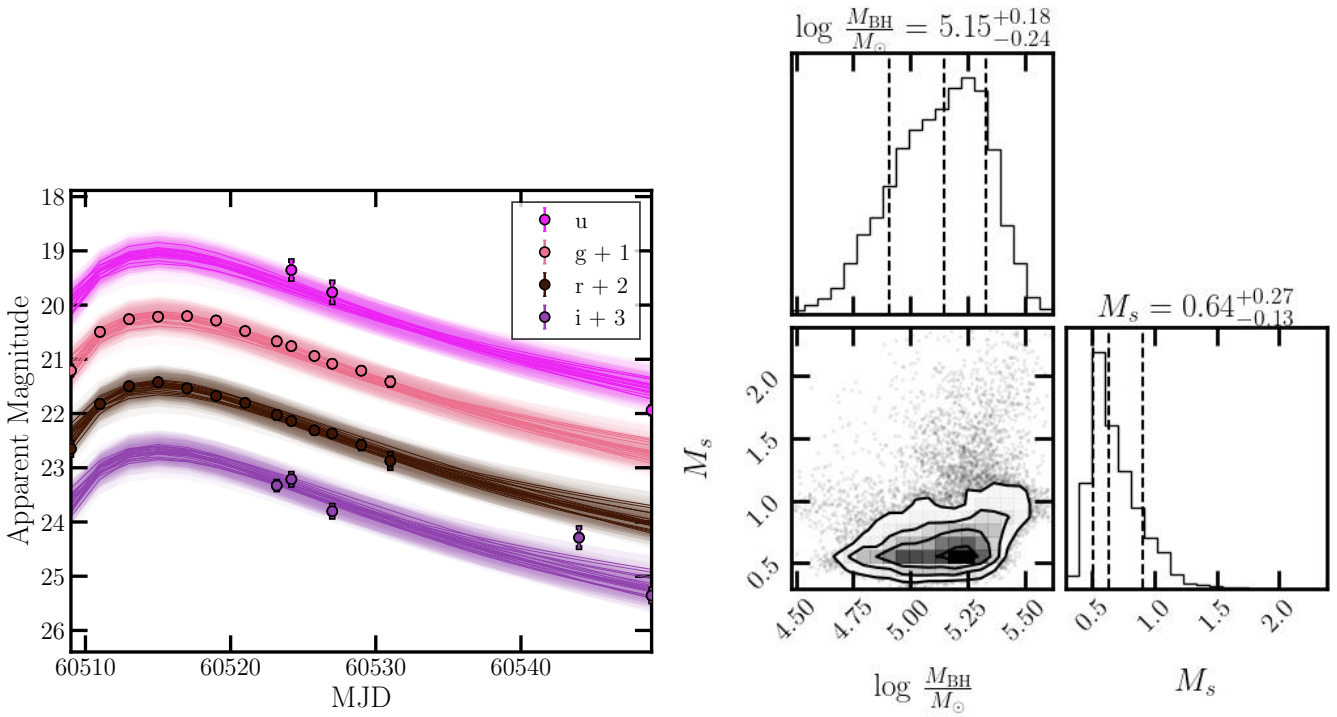

Figure 12. Summary of results from the MOSFIT TDE modeling. Realizations from the MCMC samples are overlaid on select observations in the left panel. We only include observations in representative bands for clarity, but perform the fit with all data. The constraints on BH ($M_{\rm BH}$) and disrupted star mass (M_s) are shown in the right panel.

then reprocessed into a blackbody by a reprocessing layer with power-law evolution in the photospheric radius.

We performed an initial MOSFIT fit with default settings, using the dynesty sampler and the default priors for the TDE model, except that we set the BH mass lower limit to $50\,M_\odot$. As found by D. A. Perley et al. (2019) in their analysis of the LFBOT AT 2018cow, the model was unable to fit 24puz because the observed radiation is super-Eddington for $M_{\rm BH} \lesssim 10^7\,M_\odot$, but such BH masses are not expected to produce the short-timescale flares observed. Following D. A. Perley et al. (2019), the only way to obtain a good fit was to turn off the Eddington radiation limit. However, MOSFIT does not include a proper treatment of super-Eddington radiation, and thus, the results should be taken very cautiously. We otherwise ran with the default settings. The results are shown in Figure 12. A full corner plot with the results is shown in Figure 18 in Appendix G. The best-fit model invokes a BH with $\log M_{\rm BH}/M_\odot = 5.15^{+0.18}_{-0.24}$ that is partially disrupting a relatively low-mass star $M_* = 0.64^{+0.27}_{-0.13}\,M_\odot$.

This suggests that a TDE-like model could work for 24puz, but only with highly super-Eddington radiation. Since MOSFIT is not designed to include these physics, we cannot be confident in the exact fit parameters, so we do not attempt to interpret the results in detail. Instead, we simply conclude that 24puz may be interpretable within a TDE-like model if the peak optical/UV luminosity is highly super-Eddington. Simulations are increasingly a suggestion that super-Eddington radiation and accretion are feasible (Y. F. Jiang et al. 2014; J. C. McKinney et al. 2015; E. Takeo et al. 2019; Y.-F. Jiang & L. Dai 2024). The accretion-power may be in the form of mechanical energy carried by optically thick outflows, which then convert the kinetic energy into radiation.

Observations of ultraluminous X-ray sources find luminosities up to $10^{42}\,{\rm erg\,s^{-1}}$, corresponding to Eddington ratios 10^{2-3} (A. King et al. 2023). Such highly super-Eddington radiation has not been observed from standard TDEs (e.g., Figure 12 of Y. Yao et al. 2023). However, the TDE accretion rate becomes more super-Eddington as $M_{\rm BH}$ decreases, scaling as $\frac{L_{\rm acc.}}{L_{\rm Edd.}} \sim 20\left(\frac{M_{\rm BH}}{10^6\,M_\odot}\right)^{-1.46}$ (S. Wu et al. 2018). Most TDEs have been observed with $M_{\rm BH} \gtrsim 10^6\,M_\odot$, where $\frac{L_{\rm acc.}}{L_{\rm Edd.}} \sim 20$. If 24puz has $M_{\rm BH}/M_\odot \lesssim 10^5$, then $\frac{L_{\rm acc.}}{L_{\rm Edd.}} \gtrsim 600$. We require a radiative efficiency of $\sim 0.2\left(\frac{M_{\rm BH}}{10^6\,M_\odot}\right)^{0.46}$, which is consistent with the results from simulations of super-Eddington disks for $M_{\rm BH} \lesssim 10^4\,M_\odot$ (radiative efficiencies of $\sim$0.3%; A. Sadowski & R. Narayan 2016). A low BH mass thus may explain the higher radiation Eddington ratio observed for 24puz relative to typical observations. This result will be supported by our analysis of the host galaxy in Section 6.

If we are observing emission from gas that is photoionized by an accretion source, then we must consider the lightcurve shape, which begins with a $\sim$day rapid rise. The lightcurve then shows a slow rise or a plateau for $\sim$10 days before rapidly decaying. The initial turn-on may correspond to accretion beginning. The slow rise/plateau could be explained if the radiation Eddington ratio is not truly unlimited, but reaches a cap above $\sim$100–1000 (or see B. D. Metzger 2022, for an accretion-powered model that could produce similar emission; we will discuss this model in more detail shortly). If 24puz has reached such a limit of super-Eddington radiation, the observed radiation may appear as a plateau until the accretion rate has dropped to sufficiently low values so that the radiation begins to trace the accretion rate. Extrapolating from the

power-law decay to early times, this implies a remarkable peak accretion rate of $\gtrsim 10^{46}\,\mathrm{erg\,s^{-1}}$. Alternatively, the central source may have a plateau in its accretion rate.

We conclude that an accretion-powered model may be able to explain our observations, although with significant uncertainties due to the requirement of super-Eddington radiation.

We next consider a shock breakout. This discussion closely follows D. K. Khatami & D. N. Kasen (2024). Let us define $M_{\rm ctm} = M_{\rm ctm,\odot} M_\odot$ as the mass of the circumtransient material, $R_{\rm ctm} = R_{\rm ctm,16} \times 10^{16}\,\mathrm{cm}$ as the edge of the circumtransient material, $M_{\rm ej}$ as the ejecta mass, and $v_{\rm ej} = \beta_{\rm ej} c$ as the ejecta velocity. Define $\eta = M_{\rm ctm}/M_{\rm ej}$. The shock velocity at $R_{\rm ctm}$ is related to the ejecta velocity as $v_{\rm sh} = \beta_{\rm sh} c = v_{\rm ej} \eta^{-\alpha}$.

As discussed in detail in D. K. Khatami & D. N. Kasen (2024), there are four regimes that produce separate lightcurve behavior, determined by (1) whether the shock breakout occurs within or at the edge of the circumtransient medium and (2) whether η is large ($\gtrsim 1$) or small ($\ll 1$). The optical emission from the LFBOT AT 2018cow was reproduced by a shock model for the case of edge shock breakout with a small circumtransient medium ($\eta \ll 1$). 24puz rises rapidly in the optical for a few days, and then, the rise rate slows for $\sim$1 week. The luminosity then rapidly drops. Unlike AT 2018cow, the behavior of 24puz is expected in a model where the shock breakout occurs inside the circumtransient material, but still with a light circumtransient medium ($\eta \ll 1$). In this case, the initial, rapid rise corresponds to the shock breakout. The slow rise traces the shock kinetic luminosity and, as we will show, implies a shallow circumtransient medium density profile. The rapid drop begins once the shock reaches $R_{\rm ctm}$. At this point, we would expect to detect some cooling of the emission, which is not the case for 24puz, so we would require a secondary component to heat the ejecta at late-times. We will discuss this later in this section.

We assume a slope $s = 1$ fiducially. To reproduce the slope of the slow luminosity rise, we require an ejecta profile $\rho_{\rm ej} = r^{-n}$ with $n = 12$. A shallower slope s is also allowed, in which case the ejecta profile will also be slightly shallower (e.g., for $s = 0$, we have $n = 10$). We tested values of $s = 0$ and $s = 1$, and our general conclusions do not change. We do not perform any quantitative fitting and instead attempt to roughly reproduce the lightcurve using analytic estimates from D. K. Khatami & D. N. Kasen (2024); we encourage work quantitatively fitting the lightcurve to light, interior shock interaction models.

The start date is not directly observable, so we constrain it (and thus $t_{\rm bo}$ and $t_{\rm se}$) as follows. This procedure is imperfect, and constraining the physical parameter using a simulated model grid instead would be ideal. First, we use the analytic expression in D. K. Khatami & D. N. Kasen (2024) to solve for the ejecta velocity $v_{\rm ej} = \beta_{\rm ej} c$, the circumtransient medium mass $M_{\rm ctm}$, the outer radius of the circumtransient medium $R_{\rm ctm}$, and the breakout luminosity $L_{\rm bo}$ as a function of breakout time $t_{\rm bo}$, shock emergence time $t_{\rm se}$, and η. We find

$$v_{\rm ej} = \eta^{\alpha} \left(\frac{\kappa L_p}{4\pi c t_{\rm bo}} \right)^{1/3}; \tag{6}$$

$$M_{\rm ctm} = L_p t_{\rm se} \left(\frac{4\pi c t_{\rm bo}}{\kappa L_p} \right)^{2/3}; \tag{7}$$

$$R_{\rm ctm} = \left(\frac{\kappa L_p t_{\rm se}^3}{4\pi c t_{\rm bo}} \right)^{1/3}; \tag{8}$$

$$L_{\rm bo} = L_p \left(\frac{t_{\rm bo}}{t_{\rm se}} \right)^{\frac{(5-s)(n-3)}{n-s} - 3}. \tag{9}$$

Here, we have defined $\alpha = \frac{1}{n-3}$ and the electron-scattering absorption coefficient $\kappa = 0.34\,\mathrm{cm^2\,g^{-1}}$. We pick combinations of $t_{\rm bo}$ and $t_{\rm se}$ such that (1) $t_{\rm se}$ corresponds to 9.6 rest-day post-discovery, which is when the luminosity began to decay, and (2) the luminosity at time $t_{\rm bo}/2$ is approximately equal to $0.1 L_{\rm bo}$. We consider two extreme values of $t_{\rm bo}$ and $t_{\rm se}$, corresponding to early and late start dates, to highlight the range of possible parameters. Earlier start times relative to the detection epoch will bring the ratio of $t_{\rm se}$ and $t_{\rm bo}$ close to 1 to satisfy condition (2), while later start times would always overproduce the $t_{\rm bo}/2$ luminosity.

The corresponding circumtransient medium parameters are $R_{\rm ctm} \approx 10^{15}\,\mathrm{cm}$, which roughly matches the maximum measured blackbody radius, and $M_{\rm ctm} \approx 0.1$–$1\,M_\odot$. We cannot tightly constrain the ejecta mass without a direct observation of the wind velocity. We have assumed $\eta \ll 1$, so we have $M_{\rm ej} \gg 0.1\,M_\odot$. This corresponds to a shock velocity $\beta_{\rm sh} \gg 0.06$ at $R_{\rm ctm}$, implying a fast shock. If we assume the ejecta mass is not huge, which we will define as $\lesssim 100\,M_\odot$, we can set a lower limit on the shock velocity $\beta_{\rm sh} \gg 0.03$. The limits for the case of small $t_{\rm bo}$ are shown in Figure 13. Note that these parameters are consistent with the radio upper limits: the implied densities are sufficiently high ($\sim 10^{10}\,\mathrm{cm^{-2}}$) that free–free absorption will prevent detection of synchrotron emission, or the density may fall as a steeper power law outside $R_{\rm ctm}$.

The shock breakout model explains the optical/UV lightcurve shape at early times, and such a model has been used for events with similar lightcurve evolution, although generally on much longer timescales and with lower luminosities (e.g., E. Karamehmetoglu et al. 2017). We encounter two problems at later times: the lack of cooling and transient spectral features. The lack of cooling may require an additional ionizing source that dominates by $\sim$20 days (E. Nakar & A. L. Piro 2014; R. Margutti et al. 2019), but we may expect a contribution from reprocessing of a central source given the luminous X-rays detected (e.g., R. Margutti et al. 2019; W. Lu & C. Bonnerot 2020; B. D. Metzger 2022). The lack of lines could also be explained by an additional ionizing source, if it is sufficient to keep the emitting region fully ionized, or if the circumtransient medium has a rapid density drop-off at the photosphere so that the line-emitting region is small. Full radiative transfer simulations of the shock model with similar physical parameters to those of 24puz would determine whether the lack of cooling and lines are prohibitive.

In summary, the early time optical/UV lightcurve could be explained using both accretion-powered and shock breakout models. In the accretion-dominated case, we have invoked highly super-Eddington radiation to explain the large luminosities. While such radiation is feasible within the current state of the theory of super-Eddington accretion, this regime has yet to be fully understood. The shock breakout model can more easily explain the early time emission, as such emission is not Eddington limited. At late-times, the shock breakout model does not naturally explain the lack of cooling and spectral features, but detailed simulations are required to assess the significance of this problem. We expect that the reality is a

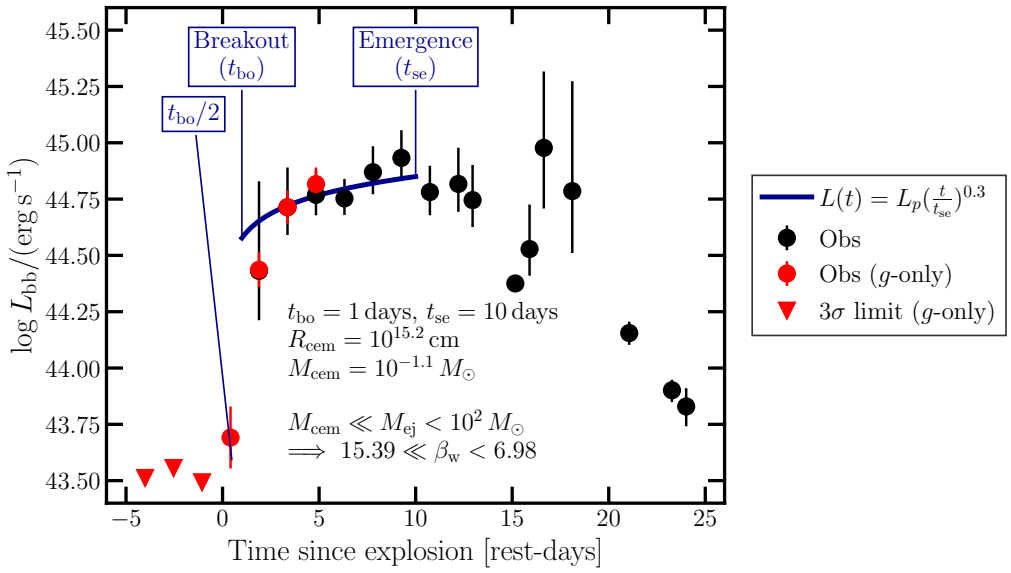

Figure 13. Constraints on a shock breakout model for the optical/UV emission from 24puz, assuming that the ejecta mass (M_{ej}) is much larger than the circumtransient medium mass (M_{ctm}), and the circumtransient medium has a power-law density profile with slope $s = 1$. The optical/UV blackbody luminosity is shown as a function of time in black in both panels. The red points show the luminosity obtained from early g-band-only detections of 24puz, for which we could not fully constrain the luminosity. We assume the temperature is the average of over the first ∼5 days. We show the case of small t_{bo} for illustration. The shock emergence is assumed to occur on the same day in both panels, corresponding to the time at which the luminosity begins to decrease. The blue solid line shows the expected power-law evolution of the lightcurve within the shock breakout model, from Equation (9). The resulting inferred physical parameters (circumtransient medium radius R_{ctm} and mass M_{ctm}) are listed on the bottom, including a range of possible shock velocities inferred from the assumption that $M_{ej} \gg M_{ctm}$, and the ejecta mass is reasonably small $\lesssim 10^2\,M_\odot$.

combination of the two forms of emission. At early times, strong shock emission can alleviate the requirement of extremely super-Eddington radiation, while, at late-times, a contribution from accretion-power can prevent the formation of spectral lines. Such a combination may also be consistent with simulations, where highly super-Eddington accretion disks are expected to release most of their energy in the form of winds (A. Sadowski & R. Narayan 2016), and so, shock emission is not unexpected. As the Eddington ratio drops, the radiative component becomes more important (A. Sadowski & R. Narayan 2016).

5.1.2. The Red Excess

In addition to the optical/UV flare, 24puz showed a red excess above a single blackbody fit in the final two epochs of observations (31–56 rest-day postdiscovery). There are a few models that are typically considered for similar sources: thermally emitting gas/dust, re-processing of high-energy emission by gas, gamma-ray burst-like nonthermal emission, and radioactive decay. We consider the agreement with each of these models with our HST observations, which have the best coverage of the red excess.

We begin with a thermally emitting region. We first modeled the UVOIR emission as two blackbodies. The temperature of the cooler blackbody was $\log T_r \approx 3600$ K, which is above the sublimation of all dust grains, but too cool to be consistent with photoionized gas. If the red excess is produced by dust, the temperature inconsistency can be improved by modeling the emission as a hot blackbody and a modified blackbody that accounts for dust absorption (B. D. Metzger & D. A. Perley 2023; S. Tuna et al. 2025). We test both the graphite and silicate models from B. T. Draine & A. Li (2007) and report the results for the more conservative graphite model in Table 13. The temperature is still ∼3500 K; i.e., significantly above the sublimation temperature of graphite grains (∼2000 K). This discrepancy is highlighted in Figure 14, where we show our HST observations in black and an example SED for a hot blackbody with additional graphite thermal emission in dashed blue. The model shown is not fit to the data, but demonstrates that graphite emission causes a peak redward of the observed red excess (near 2 μm), whereas the observed red excess is present by 9000 Å. We thus exclude dust as the main source of the red excess.

We next consider gamma-ray burst-like nonthermal emission. This model is immediately disfavored by the long timescale of the emission, which is much slower evolving than gamma-ray burst-like afterglows. Moreover, a power-law + hot blackbody fit provides a poor model of the HST data, as seen in the bottom right panel of Figure 16. In the right panel of Figure 14, the best-fit power law+blackbody to the HST data predicts a radio luminosity that is comparable to our 5σ upper limits, which are described in Section 4.5. However, our HST data were obtained ∼40–60 rest-days after the radio observations. If the emission is caused by an on-axis jet, then the jet emission should be brighter at earlier times: this is ruled out by the luminous radio emission predicted at late-times by the power-law extrapolation from the HST data. If the emission is caused by an off-axis jet that is now wide-angle and nonrelativistic, allowing us to view its emission, it is feasible for the radio emission to be brighter at ∼80 days than at early times. The shallow observed slope disfavors this scenario. As discussed, we have $\nu F_\nu \sim \nu$, or $F_\nu \sim$ const. This slope is inconsistent with typical gamma-ray burst synchrotron frameworks. Because of the poor fit, the lack of a radio detection, and the shallow observed slope, we rule out this model.

We next consider high-energy emission that has been reprocessed by gas in the circumtransient medium. We will leave detailed models of this reprocessing to future work, but use simple estimates to assess agreement with our

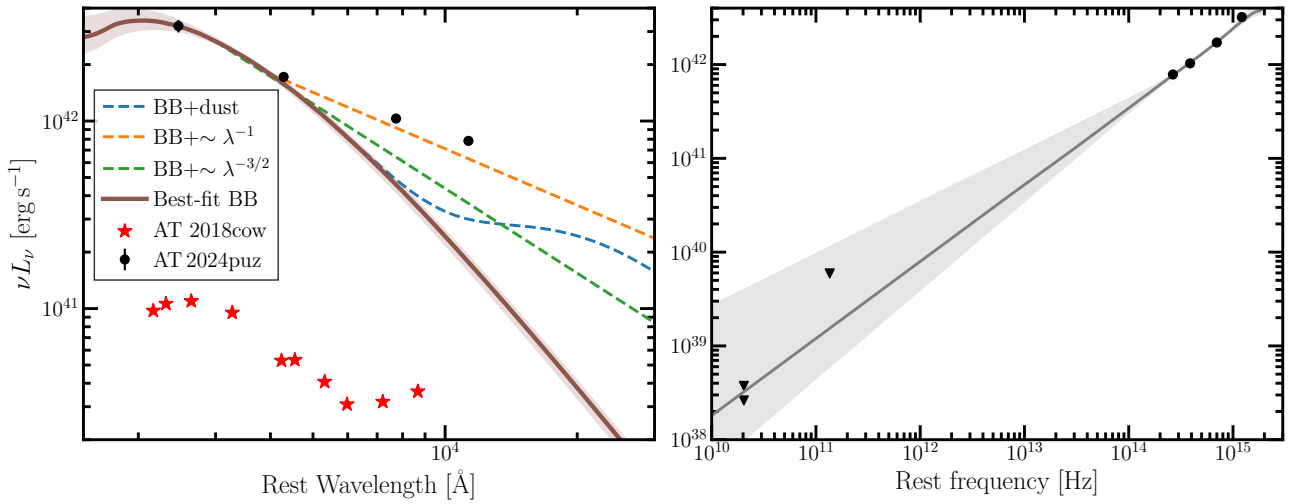

Figure 14. Constraints on the origin of the red excess from 24puz. The left panel shows the HST spectral energy distribution of 24puz in black and, for comparison, an epoch of observations of the red excess from AT 2018cow in red. A best-fit hot blackbody is shown in brown. The dashed lines show the hot blackbody with potential red excess emission added on. These are not fits but are meant to guide the eye. In orange, a λ^{-1} power law was added to represent reprocessing in a shallow medium; in green, a $\lambda^{-3/2}$ power law is summed to represent reprocessing in a wind-like medium. In blue, we add a dust blackbody to show that this model peaks redward of the excess. The right panel shows our radio upper limits as black triangles. The gray band shows an extrapolation of a power-law fit to the HST data to radio frequencies. Considering that the HST data is taken at later times than the radio, so we would expect it to have faded with time, the power-law extrapolation overpredicts the radio limits.

observations. We follow C. Chen & R.-F. Shen (2024) and W. Lu & C. Bonnerot (2020).

In this model, the red excess is caused by a change in the dominant opacity at longer wavelengths, as detailed in W. Lu & C. Bonnerot (2020). At near-infrared wavelengths, free–free absorption dominates. This absorption coefficient is given by

$$\kappa_{ff} = 0.018 T^{-3/2} \nu^{-2} \rho^2 m_p^{-2} \ [\mathrm{cm^2\ g^{-1}}], \tag{10}$$

where T is the temperature of the emitting region, ν is the frequency under consideration, ρ is the density, and m_p is the proton mass. We have assumed that we are in the Rayleigh–Jeans limit and neglected the Gaunt factor.

We assume a power-law density profile

$$\rho = \rho_0 \left(\frac{r}{r_0}\right)^{-s}. \tag{11}$$

In the near-infrared, free–free absorption dominates the opacity, so the thermalization radius is given by the radius at which the effective optical depth, or the product of the free–free optical depth ($\tau_{ff} \approx \kappa_{ff} \rho r$) and electron-scattering optical depth ($\tau_{es} \approx \kappa_{es} \rho r$), is 1. Quantitatively,

$$\tau_{ff}\, \tau_{es} \approx \kappa_{ff}\, \kappa_{es}\, \rho^2 r_{th,\nu}^2 \approx 1. \tag{12}$$

Here, $\kappa_{es} = 0.34\ \mathrm{cm^2\ g^{-1}}$ is the electron-scattering opacity. The luminosity is then given by

$$\nu L_\nu = 4\pi r_{th,\nu}^2 \frac{4\pi \nu B_\nu(T(r_{th,\nu}))}{\kappa_{es} \rho(r_{th,\nu}) r_{th,\nu} (s-1)}. \tag{13}$$

Combining these four equations, we find

$$\nu L_\nu = \frac{32\pi^2 k_B}{\kappa_{es} c^2 (s-1)} \left(\frac{0.018 \kappa_{es}}{m_p}\right)^{\frac{1+s}{3s-2}} \times T^{\frac{7-3s}{4-6s}} (\rho_0 r^s)^{\frac{5}{3s-2}} \left(\frac{c}{\lambda}\right)^{\frac{7s-8}{3s-2}}. \tag{14}$$

For a wind-like density profile ($s = 2$), we have $\lambda L_\lambda \sim \lambda^{-3/2}$. As shown by the dashed green line in Figure 14, this slope is steeper than the observed red excess, although note that our transition from the hot blackbody to a slope $-3/2$ power law is ad hoc and not quantitatively accurate. For a shallow density profile $\rho \sim r^{-1}$, we have $\lambda L_\lambda \sim \lambda^{-1}$, which is closer to the observed slope and is consistent with our optical/UV shock interaction analysis. Many of the approximations quoted above, however, break down for slopes that are much shallower than $s = 2$. We will thus adopt an intermediate slope $s = 1.5$ for the following analysis to prevent divergences, but urge simulations of the $s = 1$ case to test if our conclusions hold.

We can evaluate the required density by matching the red excess luminosity to that predicted by Equation (14). For a luminosity $\nu L_\nu \sim 10^{42}\ \mathrm{erg\ s^{-1}}$ at $\sim$7000 Å and $s = 1.5$, we find that the density is $10^{10.5}\ \mathrm{cm^{-3}}$ at 10^{15} cm, and the total mass must be $\sim 0.2\, M_\odot (R_{\rm out}/10^{15.1}\ \mathrm{cm})$. This is consistent with the circumtransient medium mass that was inferred in our shock interaction analysis $M_{\rm ctm} \lesssim 1\, M_\odot$ for $R_{\rm ctm} \approx 10^{15}$ cm. If this density profile extends farther out, our radio analysis may pose a problem as we find $\rho(R = 10^{16}\ \mathrm{cm}) \approx 10^9\ \mathrm{cm^{-3}}$, which is on the border of our excluded region in Figure 11 unless the outflow velocity is $\lesssim 0.1c$. Free–free absorption would remove this limit. Alternatively, if the density profile drops rapidly at 10^{15} cm, then the allowed outflow velocity is higher. Given that the implied mass of this profile extends to 10^{16} cm is $\sim 20\, M_\odot$, which is very large, we believe this latter explanation is likely.

The lack of any significant absorption in the X-ray spectrum poses a problem: the implied column density is $\gtrsim 10^{25}\ \mathrm{cm^{-2}}$ for an outer radius $R_{\rm ctm} \sim 10^{15.1}$ cm and an inner radius corresponding to the smallest radius measured from our blackbody fitting in Table 13, $R_{\rm in} \sim 10^{14.4}$ cm. A smaller $R_{\rm in}$ corresponds to a larger column density. We can alleviate this discrepancy if the emitting region is aspherical. If we are viewing the system along a line of sight without significant gas/dust, then the X-rays would appear unabsorbed, as is

observed. Alternatively, if the emitting region is fully ionized, it is effectively transparent to X-rays.

There are a number of key caveats to this analysis. First, we adopted common approximations to the photon diffusion time and optical depth that break as the density profile becomes shallower. Moreover, this analysis assumes a spherical, homogeneous medium. If the material is anisotropic or clumpy, then the total mass will be reduced by the volume filling factor (C. Chen & R.-F. Shen 2024). Finally, we have adopted an outer radius based on our optical/UV shock analysis, but accretion-power likely contributes to this emission, and this was not included in our modeling.

5.1.3. The X-Ray Emission

We next consider the origin of the X-ray emission. The X-ray spectrum, luminosity evolution, and variability are both very similar to that of the soft component of AT 2018cow. The X-rays from AT 2018cow are considered to be associated with a shock or central engine (R. Margutti et al. 2019).

We first consider a central engine model. In this case, the rapid variability is expected given the small scales of an accretion disk. The implied maximum X-ray luminosity is highly super-Eddington for a compact object of a mass $\lesssim 10^6 M_\odot$. The typical X-ray luminosity, however, is $L_X \sim 3 \times 10^{43}\,\mathrm{erg\,s^{-1}}$, which is super-Eddington for masses $\lesssim 10^5$ for the compact object masses we will favor in the following section. As discussed earlier, super-Eddington radiation has been observed, up to $\sim 10^3 L_{\rm edd}$ (A. King et al. 2023). The luminous optical/UV emission suggests that most of the X-rays, in a central engine model, are reprocessed. A fraction escapes either due to inhomogeneities in the surrounding medium or because they have ionized the ejecta along our line of sight.

We next consider a shock origin of the X-rays. This model faces two problems. First, as discussed in Section 4.4, our Bremsstrahlung modeling suggests a best-fit temperature of 7 ± 1.5 keV, which is lower than typical X-ray emission from shocks (C. Fransson et al. 1996). It is also challenging for a shock to produce the ∼day timescale variability observed from 24puz: this would require significant density variations in the circumtransient medium. Variability on a timescale of days for a shock traveling at $0.1c$ implies spatial variability scales of $\sim 10^{14}$ cm. Some circumstellar media do show such variability, but it is not clear whether this is natural for a system like 24puz (e.g., see similar discussion for the LFBOT AT 2018cow in L. E. Sandoval et al. 2018). We encourage simultaneous modeling of the optical/UV and X-ray emission within a shock framework to assess whether shocks can dominate the observed emission, but we currently disfavor shocks as the dominant source of X-ray emission.

We conclude that a central engine model for 24puz can explain the observed X-rays. A shock model may be feasible, but faces significant challenges (low best-fit temperature and rapid variability).

6. Discussion

6.1. Comparison with Known Transients

The persistently blue optical colors and featureless spectra place 24puz in the section of optical transient parameter space occupied by two observational classes: LFBOTs (S. J. Prentice et al. 2018; B. D. Metzger 2022) and TDEs (J. G. Hills 1975; V. V. Lidskii & L. M. Ozernoi 1979; E. S. Phinney 1989). Supernovae are excluded by the rapid evolution and persistently featureless spectra, with a lack of interaction signatures and the high radiated energy ($>10^{51}$ erg). The luminous, fast-cooling transients presented by M. Nicholl et al. (2023) occupy a similar location in luminosity-timescale space, but show rapid cooling that is excluded for 24puz. They are also not X-ray and radio bright.

TDEs occur when a star is disrupted by an MBH (M. J. Rees 1988; C. R. Evans & C. S. Kochanek 1989; A. Ulmer 1999). Like LFBOTs, TDEs typically produce blue, constant-color optical lightcurves, but they evolve more slowly, rising over few-week timescales and fading over months (S. Gezari et al. 2006, 2008; I. Arcavi et al. 2014; S. van Velzen et al. 2019, 2021). Most TDEs produce broad ($\sim 10^4\,\mathrm{km\,s^{-1}}$) Balmer and helium spectroscopic features (E. Hammerstein et al. 2023; Y. Yao et al. 2023; S. van Velzen et al. 2021), but two possibly connected subclasses of TDEs produce featureless spectra: featureless TDEs (F-TDEs; E. Hammerstein et al. 2023) and jetted TDEs (I. Andreoni et al. 2022). F-TDEs have spectra that are featureless for months post-TDE (E. Hammerstein et al. 2023; Y. Yao et al. 2023). Jetted TDEs are best known for launching collimated, relativistic jets (J. S. Bloom et al. 2011; D. N. Burrows et al. 2011; S. B. Cenko et al. 2012; G. C. Brown et al. 2015; D. R. Pasham et al. 2023), and there is some evidence that they also produce featureless spectra and blue, constant-color thermal emission (in addition to luminous, nonthermal emission from the jet; I. Andreoni et al. 2022). By selection, TDEs are traditionally detected in the nuclei of their host galaxies (typically within 1″; S. van Velzen et al. 2019, 2021; E. Hammerstein et al. 2023; Y. Yao et al. 2023).

LFBOTs rise on few-day timescales and fade over ∼1 week (D. L. Coppejans et al. 2020; D. A. Perley et al. 2021; Y. Yao et al. 2022; A. Y. Q. Ho et al. 2023, 2020, 2022; D. Matthews et al. 2023; A. A. Chrimes et al. 2024b). LFBOTs produce hot ($\sim 10^{4-5}$ K) optical flares without substantial cooling and absolute magnitudes brighter than approximately −20.5 mag. They evolve fast (≲week timescale), with no detectable optical spectral lines at early times. LFBOTs never show nebular features, and instead have hydrogen and helium features, unlike stellar explosions. They are luminous in the millimeter, suggestive of outflows into dense media ($\sim 10^5\,\mathrm{cm^{-3}}$). LFBOTs have hard X-rays ($\nu F_\nu \sim \nu^{-0.5}$) likely from the central engine that is also responsible for powering the transients, which could be explained by invoking an asymmetric circumtransient medium and a weak, decelerating jet. They often have a Compton hump feature detected in the hard X-ray, which is common among accretors like X-ray binaries and active galactic nucleus, and is associated with cold, optically thick gas (C. S. Reynolds & S. C. Reynolds 1999). The X-ray spectra have been detected to soften at late-times (G. Migliori et al. 2024). LFBOTs are hosted in a range of environments, although most have been offset within galaxies near the star-forming main sequence. LFBOTs have featureless blue optical spectra that, in some cases, develop broad ($\sim 10^4\,\mathrm{km\,s^{-1}}$) hydrogen/helium emission after ∼10 s of days and intermediate width ($\sim 10^3\,\mathrm{km\,s^{-1}}$) lines after ∼1 month. HST observations of one LFBOT, AT 2018cow, show a late-time (years) plateau in the UV and soft X-ray (N. C. Sun et al. 2022; Y. Chen et al. 2023a; A. Inkenhaag et al. 2023; G. Migliori et al. 2024). The most offset LFBOT detected thus far is at

1 kpc $\approx 3.5 r_e$ from its host galaxy, where r_e is the galaxy half-light radius (A. A. Chrimes et al. 2024a).

The physical origin of LFBOTs is unknown. The late-time UV and possible X-ray plateau detected for AT 2018cow is reminiscent of late-time emission from the compact accretion disks produced during TDEs (N. C. Sun et al. 2022; Y. Chen et al. 2023a; A. Inkenhaag et al. 2023; G. Migliori et al. 2024), suggesting that LFBOTs may be TDEs. The faintness of the plateau, combined with the off-nuclear location of the transients, requires TDEs by IMBHs. LFBOTs may alternatively be extreme stellar explosions/mergers. Models are typically required to produce an extended, dense, aspherical medium and a highly energetic and compact central engine. B. D. Metzger (2022) proposes the delayed merger of a BH and a Wolf–Rayet star. R. Margutti et al. (2019) consider a failed explosion of a blue supergiant star, resulting in a stellar-mass BH surrounded by the remains of the star, although G. Migliori et al. (2024) revise this model to prefer a super-Eddington accreting source. Both models require the presence of massive stars ($\gtrsim 20\,M_\odot$). A millisecond magnetar formed after the electron capture supernova of a $\sim$8–10 $M_\odot$ star is consistent with observations, but still invokes a relatively massive star. Attempts to model the LFBOT AT 2018cow as a magnetar require NSs with near maximal masses and may not be able to explain the multiwavelength emission (e.g., fast X-ray variability, late-time UV plateau; L. Li et al. 2024).

24puz has multiwavelength properties that are consistent with both TDEs and LFBOTs. In Figure 2, we compare the optical/UV blackbody luminosity evolution of 24puz, TDEs, and LFBOTs. The left panel shows the blackbody luminosity as a function of time for these objects. 24puz has a lightcurve evolution that is generally consistent with LFBOTs, with a rapid rise followed by a power-law decay. 24puz peaks at a later time relative to other LFBOTs and has a slower rise. This is highlighted in the right panel, which shows the time above half-peak luminosity on the x-axis and the peak g-band luminosity on the y-axis. 24puz is slower than all LFBOTs. Selection effects likely play a role in this trend: LFBOTs are selected to be fast evolving, with generally faster than $\sim$1 week timescales (e.g., A. Y. Q. Ho et al. 2023). 24puz may be a slow-evolving LFBOT, suggesting that LFBOT searches should be performed with looser timescale cuts. LFBOTs typically show an early time blackbody temperature of $\sim 10^{4.5-4.6}$ K, which later plateau at $\sim 10^{4.3}$ K. 24puz shows a similar evolution, but is potentially cooler at early times (although note the large uncertainties in Figure 9).

The lightcurve shape of 24puz is also consistent with TDEs, although these events show more variation in their blackbody luminosity evolution relative to LFBOTs. The blackbody temperature evolution is fully consistent with TDEs, which show typical early time temperatures of $10^{4-4.5}$ K (see Figure 5 of J. J. Somalwar et al. 2025). The location of 24puz in luminosity-timescale space is unprecedented for TDEs, which generally show a positive correlation between luminosity and timescale. F-TDEs break this correlation, but have long timescales ($\gtrsim$30 days). There are no obvious selection effects that would prevent events like 24puz from being discovered in TDE searches, if 24puz-like objects can occur in galactic nuclei, suggesting that such events are rare.

The featureless optical spectra detected from 24puz are consistent with both early time LFBOT observations and with F-TDEs and jetted TDEs. LFBOTs generally produce some spectral features at late-times (both broad and narrow interaction lines). If 24puz is an LFBOT, the lack of lines could be consistent with the high luminosity, as discussed above, but this would be unprecedented for this class. F-TDEs remain featureless at all times, consistent with 24puz.

A red excess like that from 24puz has been detected for the LFBOT AT 2018cow (D. A. Perley et al. 2019). The origin of this excess is also unknown, although similar models were proposed as we have explored for 24puz. The optical-IR SED of AT 2018cow is shown as red stars in Figure 14. The peak of the AT 2018cow excess is redder than that of 24puz, and so, a thermally emitting dust origin is still consistent with the observations (B. D. Metzger & D. A. Perley 2023). Reprocessing can also reproduce the red excess, but requires $\gtrsim 5\,M_\odot$ of material (C. Chen & R.-F. Shen 2024). TDEs have been theorized to produce near-infrared excesses due to reprocessing (W. Lu & C. Bonnerot 2020), with one known example that showed a red excess likely due to reprocessing by a disklike structure (N. Earl et al. 2025). Thermally emitting dust has been detected for multiple TDEs, but this emission peaks in the mid-infrared and on year-long timescales and is inconsistent with the observations of 24puz.

The radio and millimeter limits from 24puz are consistent with both TDEs and LFBOTs. $\gtrsim$30% of optically selected TDEs produce radio emission at $\gtrsim$3 yr postdisruption. The fraction detected at early times is lower, suggesting that most TDEs do not produce luminous radio emission at this point ($\lesssim 10^{38}$ erg s^{-1}). This is consistent with the 24puz limits. It is also important to note that most radio-observed TDEs are not F-TDEs, which are generally at higher redshifts. A more detailed study of the early time radio properties of these events would be required to compare to 24puz.

LFBOTs ubiquitously produce radio and millimeter emission. As shown by the stars in Figure 11, the parameter space occupied by the radio/millimeter luminous LFBOT AT 2018cow is excluded for 24puz, but if 24puz has a moderately less dense ambient medium relative to AT 2018cow, the lack of radio/millimeter emission is expected. The lack of transient spectral features would also be expected in this case.

The X-ray lightcurve from 24puz is fully consistent with LFBOTs, as shown in Figure 15. The high variability and rapid decline have been observed for multiple LFBOTs. 24puz is among the most X-ray luminous LFBOTs. The hard spectral index $\Gamma = 1.7$ is also consistent with observations of X-rays from LFBOTs. The rapid evolution and hardness of LFBOT X-rays have been used to argue for the presence of a compact central engine from these sources.

The X-ray properties of TDEs are much more heterogeneous than those of LFBOTs. Most X-ray-detected TDEs have soft spectra $\Gamma \gtrsim 3$, although exceptions do exist (Y. Yao et al. 2022; M. Guolo et al. 2024; A. Y. Q. Ho et al. 2025). There are also X-ray-detected TDEs that show rapid variability and fading (M. Guolo et al. 2024), although this behavior is not as ubiquitous as for LFBOTs. Jetted TDEs, in particular, show hard, variable X-rays like 24puz (J. S. Bloom et al. 2011; D. N. Burrows et al. 2011; I. Andreoni et al. 2022). As shown by the blue lightcurve in Figure 15, the X-ray luminosities of these events are much higher than that from 24puz due to beaming effects, but the lightcurve evolution is otherwise similar. X-ray constraints on F-TDEs are weak.

The host galaxy of 24puz is also fully consistent with LFBOT hosts in terms of stellar mass, SFR, and offset from

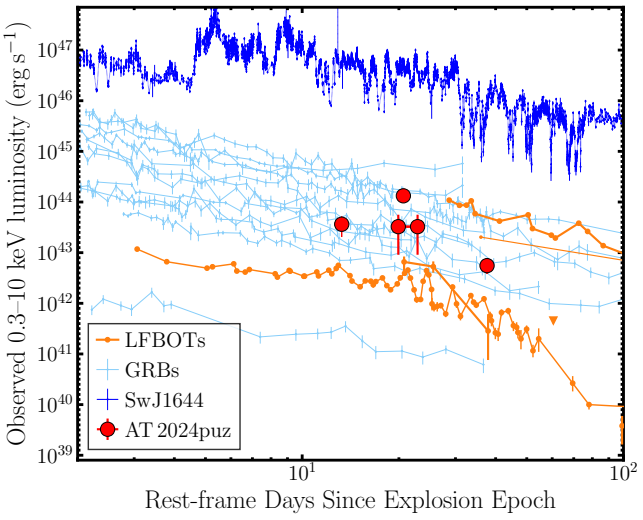

Figure 15. X-ray lightcurve comparison, adapted from Y. Yao et al. (2022). 24puz is shown in red, and LFBOTs in orange. For completeness, a population of gamma-ray bursts (GRBs) is shown in light blue, as these are common comparison points for X-ray transient emission. The jetted TDE SwJ1644 is shown in blue. 24puz is among the most X-ray luminous LFBOTs. It shows a variability and evolution timescale comparable to both LFBOTs and the jetted TDE.

the transient. LFBOT host galaxies are shown relative to that of 24puz and the star-forming main sequences in Figure 8. While the LFBOT hosts show a range of stellar masses, they tend to lie near the star-forming main sequence, and there are three events at comparable host galaxy masses to that of 24puz. As shown in the right panel of Figure 8, 24puz would be among the most offset LFBOTs relative to its host, but the LFBOT AT 2023fhn is at a similarly large offset (A. A. Chrimes et al. 2024a, 2024b). 24puz and AT 2023fhn both have large offsets given expectations based on their stellar mass, if they are associated with star formation, as is seen when comparing to the core-collapse supernovae shown in Figure 8.

TDE host galaxies, in contrast, are inconsistent with the 24puz host. TDE hosts are shown as blue scatter in Figure 8. These hosts are generally more massive than that of 24puz and lie below the star-forming main sequence (E. Hammerstein et al. 2021; Y. Yao et al. 2023). Selection effects likely play a role here. TDEs are required to be nuclear, whereas massive BHs in dwarf galaxies are often wandering due to a poorly defined gravitational potential. If TDEs from low-mass galaxies tend to be off-nuclear, like 24puz, they will not be included in current selections. F-TDE host galaxies are the most discrepant from that of 24puz, as they tend to be the reddest and most massive ($M_* \gtrsim 10^{10}\,M_\odot$) of the TDE hosts (E. Hammerstein et al. 2023).

We conclude that 24puz closely resembles LFBOTs, except that it is more luminous in the X-ray through optical, is slower evolving, and has no spectral features at late-times. 24puz is similar to TDEs in many ways, but that it is fast and luminous in the optical/UV, off-nuclear from a low-mass galaxy, and has harder, faster-evolving X-ray emission than most TDEs.

6.2. The Rate of 24puz-like Transients

Our search that produced 24puz was incomplete, and a sample size of one leads to large statistical uncertainties in a rate estimate. However, we can set an upper limit on the rate using the ZTF bright transient survey (BTS; C. Fremling et al. 2020; D. A. Perley et al. 2020), which has produced complete samples of transients above $m < 18.5$ mag. No sources have been reported as blue, constant colors, extragalactic redshifts, and a timescale of ∼10 days. We thus use the lack of 24puz-like objects reported in the BTS sample to constrain the rate of such events. Given the peak magnitude of 24puz ($m_g = 19.2$ mag), the magnitude limit of BTS, and the completeness reported by D. A. Perley et al. (2020), we find a 3σ upper limit on the rate of 24puz-like objects of $<4.6 f_c^{-1}$ Gpc^{-3} yr^{-1}. Here, f_c is the completeness fraction.

The optical TDE rate is 310^{+60}_{-100} Gpc^{-3} yr^{-1} (Y. Yao et al. 2023), which is higher than the 24puz rate, but is consistent if 24puz-like objects are a subset of TDEs. The jetted TDE rate is $2^{+4}_{-1}(f_b/1\%)^{-1}$ Gpc^{-3} yr^{-1} for a beaming fraction $f_b = 1\%$ (I. Andreoni et al. 2022), which is consistent with the rate of 24puz-like objects. The rate of LFBOTs has been estimated as 0.3–420 yr^{-1} Gpc^{-3} (A. Y. Q. Ho et al. 2023), < 300 yr^{-1} Gpc^{-3} (D. L. Coppejans et al. 2020, extrapolated from Palomar Transient Factory data), and 700–1400 yr^{-1} Gpc^{-3} (D. L. Coppejans et al. 2020, extrapolated from PS1 Medium-Deep Survey data). These are generally consistent with the rate of 24puz-like objects, although the LFBOT rate from the PS1 Medium-Deep Survey is higher.

6.3. Nature of the Powering Source

We next consider possible explanations to account for the nature of the source powering 24puz. We require a system that can produce $\gtrsim 10^{51}$ erg of radiated energy, largely in a ∼2 week span. In the shock model, this energy could be produced in a shorter, ∼day time span (∼10^5 s), corresponding to the lightcurve rise time. From the observation of a red excess, we infer that the source may be surrounded by a dense ∼10^{10} cm^{-3} medium extending to at least 10^{15} cm, with a shallow density profile scaling as $\sim r^{-1}$. The source produces hard ($\Gamma = 1.7$) X-ray emission that is variable on short, ∼3 day timescales.

First, from the short-timescale variability and hard X-ray emission, we conclude that 24puz has a compact central engine, as has been argued for LFBOTs and given the concordance with the observed properties. We now consider the type of compact source.

We immediately rule out magnetars, massive stars, and NSs based on the low mass of and lack of strong star formation in the host galaxy. Events associated with such objects should be orders of magnitude more common in star-forming and massive galaxies. Selection effects may play a role here: we required a faint host galaxy in our search. Star-forming galaxies are detectable to higher redshifts than quiescent galaxies, due to their higher luminosities, and likewise massive galaxies are more detectable. If this selection effect is the reason that we have not detected star formation, then the lack of 24puz-like transients identified thus far in, e.g., the BTS sample or supernovae searches is a puzzle, as these searches are in principle sensitive to 24puz-like sources in massive/star-forming galaxies. A similar argument holds if 24puz is associated with a globular cluster or an NS, which should be more common in massive galaxies. Note that this does not rule out a *nuclear* stellar cluster as a putative host.

The only remaining compact object is a BH, and we can use similar arguments to those above to constrain the mass of the BH. If 24puz is associated with a $<50\,M_\odot$ stellar-mass BH,

such events should be orders of magnitude more abundant in massive galaxies $\sim 10^{11}\,M_{\odot}$ (O. D. Elbert et al. 2018; A. Sicilia et al. 2022). If 24puz is associated with SMBHs $>10^{6}\,M_{\odot}$, TDE searches should have discovered analogous events, although they have not been focused on off-center events. Moreover, the proximity of a putative dwarf galaxy host and the empirically derived local scaling relations between central BH mass and stellar mass of galaxies suggests that the BH mass in 24puz is firmly in the IMBH mass range (A. E. Reines & M. Volonteri 2015). Hence, if 24puz is associated with a BH, it must be associated with a BH of the mass $M_{\rm BH}$ such that $50 \lesssim M_{\rm BH}/M_{\odot} \lesssim 10^{5}\,M_{\odot}$.

A BH at the lower end of this mass range is consistent with the highly offset position of 24puz, but the expected location of a more massive IMBH remains uncertain. The BH, in either case, must be recoiling and/or has been ejected. BHs formed from stellar deaths (i.e., in the stellar-mass regime) are expected to have a natal kick similar to that of an NS (S. Repetto et al. 2012). If the BH is formed at the time that most of the stars in the galaxy formed ($\sim$100 Myr ago, based on our host stellar population modeling) and receives a kick of $\sim 100\,{\rm km\,s^{-1}}$, it will travel 10 kpc by the time of our observation. Thus, the projected offset observed of 5 kpc is feasible.

In the more massive IMBH regime, the offset is less natural, but not impossible. If IMBHs are formed via the direct collapse of a gas cloud in situ, they should not necessarily have an associated kick. They are however expected to wander throughout their host galaxy (A. Ricarte et al. 2021a, 2021b), particularly if the host is a dwarf galaxy with a poorly defined gravitational potential (E. J. Weller et al. 2022). This BH is very offset from any light from the host galaxy, which, depending on the simulation suite analyzed, may or may not be expected frequently: the predictions from the ROMULUS simulation (A. Ricarte et al. 2021b) are different from those from the ASTRID simulation wherein wanderer offset distributions are smaller (E. J. Weller et al. 2022). Still, assuming the dark matter traces the stellar matter, it is unlikely that the BH is close to even a local minimum in the gravitational potential, but this model is currently unsettled. The IMBH could recoil if it has undergone a merger with another IMBH (J. A. González et al. 2007), which is feasible if the disturbed morphology of G1 indicates a merger. Deep follow-up imaging can confirm or exclude evidence of a merger, but note that the galaxies of the stellar mass $10^{8}\,M_{\odot}$ are not expected to undergo many mergers, especially at late-times, with an expected rate of $<0.01\,{\rm Gyr^{-1}}$ (V. Rodriguez-Gomez et al. 2015).

We conclude that the compact central engine is a BH of a mass $50 \lesssim M_{\rm BH}/M_{\odot} \lesssim 10^{5}\,M_{\odot}$, although the high offset may pose problems at higher masses. We now need to determine the reason for its outburst.

From the energy budget point of view, accretion events onto massive BHs can readily produce the amount of energy observed. One possible cause of the accretion flare is a TDE. As discussed, we were able to fit the optical/UV emission with the `MOSFIT` code. However, we had to turn off the super-Eddington radiation limit to model the emission accurately, and `MOSFIT` was not designed for this regime. The red excess and the high optical/UV luminosity can be readily explained by shocks within a dense ($\sim 10^{10}\,{\rm cm^{-3}}$), extended ($10^{15}\,{\rm cm} \approx 10^{4}\,{\rm au}$) medium surrounding the transient, but such a medium is not expected for a TDE. This is much denser than typical environments around nuclear supermassive BHs (see Figure 2 of K. D. Alexander et al. 2020), and there is no a-priori reason to expect IMBHs to have such dense local environments. There is no obvious origin of the red excess with this model, and the optical/UV emission must be highly super-Eddington. Moreover, some simulations of main-sequence TDEs suggest that the circularization timescale may be much longer for IMBHs due to weak apsidal precession (L. Dai et al. 2015), which is in contrast to the fast, luminous observed flare. One possible resolution is the tidal disruption of a white dwarf, which is expected to evolve rapidly (K. Maguire et al. 2020). We cannot rule out this model, but many uncertainties, particularly due to the origin of the red excess, remain.

In contrast, the high circumtransient medium density and energetics of the event can be accommodated by the model from B. D. Metzger (2022). This model nominally invokes a BH or NS in a binary with a massive, Wolf–Rayet star. The compact object enters into a common envelope phase with the massive star and begins inspiraling until it disrupts the stellar core. The lack of star formation from 24puz disfavors a massive star companion, but a main-sequence or evolved stellar companion should produce a similar signal. If the evolved star is a (sub)giant with a large radius, then the timescale may be too long to produce the very short rise time of 24puz. A tidally disrupted main-sequence star may better match the timescale (K. Kremer et al. 2021). We encourage efforts to simulate the emission from 24puz within this model, in particular, taking into account the requirements of an evolved or main-sequence stellar companion and a low binary mass ratio.

We finally consider the case that our assumption that the source cannot be produced by an NS or low-mass, stellar-mass BH due to the host galaxy stellar mass does not hold up to continued searches for 24puz-like sources. Another possible scenario is that the event comes from the explosion of a low-mass helium star with a main-sequence companion star, and that the newly born NS happens to tidally disrupt the companion star (D. Tsuna & W. Lu 2025). The low-mass helium star undergoes extreme mass loss before the SN explosion (S. C. Wu & J. Fuller 2022), creating the dense circumtransient medium. Such an explosion may be produced after a delay up to 50 Myrs that is consistent with the stellar population age in G1. D. Tsuna & W. Lu (2025) also showed that the rate of such events is $\sim$(0.1%–2%) of Type Ibc SNe, which is consistent with the LFBOT rate from A. Y. Q. Ho et al. (2023), and thus also with our highly uncertain estimates of the 24puz rate.

7. Conclusions

In this paper, we have presented 24puz, a luminous, multi-wavelength transient associated with a dwarf galaxy. 24puz was discovered as a hostless, blue optical flare by the ZTF survey. Deep imaging and spectroscopy showed that it is associated with a dwarf galaxy of a mass $\sim 10^{8}\,M_{\odot}$ at $z = 0.35614 \pm 0.00009$ that lies below the star formation main sequence. The spectra show no features associated with the transient.

The optical transient was accompanied by luminous UV, IR, and X-ray emission. The early time optical/UV emission is consistent either with an accretion flare that produces highly super-Eddington radiation or with a shock that is breaking out within the circumtransient medium. In the latter case, the circumtransient medium mass is $\lesssim 1\,M_{\odot}$, and it extends to a radius $\sim 10^{15}\,{\rm cm}$ with a shallow density profile. The shock

breakout model may not explain the lack of late-time cooling and line emission, and so would require an additional ionizing source, such as accretion, at ∼20 days. A near-infrared excess is seen at late-times ∼80 days that may be consistent with a reprocessing layer. The X-ray emission could be produced by a shock or a compact central engine, but the rapid evolution and variability are challenging to accommodate within a shock model.

Based on the lack of star formation and low stellar mass in the host galaxy, we favor a model invoking a BH with a mass $\gtrsim 50\,M_{\odot}$ (i.e., high-mass stellar-mass BH or IMBH), although we mildly prefer a BH formed in a stellar explosion to accommodate the high observed offset from the host galaxy. A similar model has been proposed by B. D. Metzger (2022), who postulate a stellar-mass BH consuming a massive star. Given the low SFR of G1, we prefer a main sequence or evolved companion, and we encourage more detailed consideration of this model. However, models that involve ejected IMBHs also remain plausible, in which case we favor the tidal disruption of a white dwarf to match the observed timescale of 24puz. The tidal disruption of a star by an IMBH does not naturally explain the red excess, which may require a denser circumtransient medium than expected for such sources. Further work is needed to explore whether an IMBH TDE can consistently explain the observations.

Pinning down the trigger of 24puz requires a sample of similar sources. The portion of parameter space occupied by this transient has, to our knowledge, barely been explored, and the discovery of 24puz opens up a new section of the landscape of hot, blue transients. These objects are proving to offer a powerful probe of discovering massive stellar-mass BHs, IMBHs, and NSs. Instruments and telescopes such as the upcoming Rubin Observatory, the Einstein Probe, and the Ultraviolet Explorer should be sensitive to thousands of these hot blue transients. However, archival searches in ZTF show great promise for identifying and characterizing such previously unexplored transient classes.

In addition to identifying a sample of 24puz-like events, a deep late-time follow-up may be able to pin down the event trigger. In particular, deep, multiband imaging would enable detailed constraints on the star formation history both of G1 and at the location of 24puz, strengthening our arguments against massive star and NS progenitors. Late-time radio constraints would exclude the late-time emergence of any collimated jet, as is sometimes observed for TDEs and thus may favor an IMBH progenitor (Y. Cendes et al. 2024). Deep space-based spectroscopy can rule out any late-time interaction features, which would provide an additional handle on the circumtransient medium spectrum.

We conclude by briefly considering implications for LFBOT searches and models, if 24puz is a member of this population, and our analysis of the likely progenitor is correct (accreting, $\gtrsim 50\,M_{\odot}$ stellar-mass BH in a binary). 24puz adds to the increasing fraction of LFBOTs detected in low-mass galaxies near the star-forming main sequence, and is the second LFBOT with a very high offset. Models that implicate massive stars in LFBOT models should be reassessed. 24puz suggests that LFBOTs need not be as fast evolving as previously found, and they can be even more luminous than thought. If this high luminosity is a function of the circumtransient medium parameters, it might suggest that LFBOT luminosity will be correlated with the properties of the companion star from which the BH is accreting. While the radio/millimeter constraints from 24puz offer poor constraints at present, they do suggest that, despite the high optical/UV and X-ray luminosities from this event, the radio/millimeter luminosity was not correspondingly high. LFBOTs may not be ubiquitously associated with luminous emission at these frequencies, as was once thought.

Acknowledgments

We would like to thank the referee for the valuable comments on the manuscript. We would like to thank Stella Ocker for the use of her WIRC time. We would like to thank Eliot Quataert and Xiaoshan Huang for useful discussions.

This research is based on observations made with the NASA/ESA Hubble Space Telescope obtained from the Space Telescope Science Institute, which is operated by the Association of Universities for Research in Astronomy, Inc., under NASA contract NAS 5–26555. These observations are associated with program 17854.

Some/all of the data presented in this paper were obtained from the Mikulski Archive for Space Telescopes (MAST) at the Space Telescope Science Institute. The specific observations analyzed can be accessed via doi:10.17909/3kvv-bv86.

This work made use of data supplied by the UK Swift Science Data Centre at the University of Leicester.

This work is based on observations obtained with the Samuel Oschin Telescope 48 inch and the 60 inch Telescope at the Palomar Observatory as part of the Zwicky Transient Facility project. ZTF is supported by the National Science Foundation under grant No. AST-2034437 and a collaboration including Caltech, IPAC, the Oskar Klein Center at Stockholm University, the University of Maryland, University of California, Berkeley, the University of Wisconsin at Milwaukee, University of Warwick, Ruhr University Bochum, Cornell University, Northwestern University, and Drexel University. Operations are conducted by COO, IPAC, and UW.

The ZTF forced-photometry service was funded under the Heising-Simons Foundation grant #12540303 (PI: Graham).

The Gordon and Betty Moore Foundation, through both the Data-Driven Investigator Program and a dedicated grant, provided critical funding for SkyPortal.

SED Machine is based upon work supported by the National Science Foundation under grant No. 1106171.

Some of the data presented herein were obtained at the W. M. Keck Observatory, which is operated as a scientific partnership among the California Institute of Technology, the University of California, and the National Aeronautics and Space Administration. The Observatory was made possible by the generous financial support of the W. M. Keck Foundation.

The authors wish to recognize and acknowledge the very significant cultural role and reverence that the summit of Maunakea has always had within the indigenous Hawaiian community. We are most fortunate to have the opportunity to conduct observations from this mountain.

This material is based upon work supported by the National Science Foundation Graduate Research Fellowship under grant No. DGE-1745301. M.W.C. acknowledges support from the National Science Foundation with grant Nos. PHY-2010970 and OAC-2117997. M.N. is supported by the European Research Council (ERC) under the European Union's Horizon 2020 research and innovation program (grant agreement No. 948381) and by UK Space Agency grant No. ST/Y000692/1.

P.N. acknowledges support from the Gordon and Betty Moore Foundation and the John Templeton Foundation that

fund the Black Hole Initiative (BHI) at Harvard University where she serves as an external PI.

M.W.C. acknowledges support from the National Science Foundation with grant Nos. PHY-2308862 and PHY-2117997.

Facilities: ATLAS, HST (WFC3, ACS), VLA, Keck:1, Keck:2, Hale, XMM, LDT, HEASARC, Swift, NuSTAR, PS1, IRAM:NOEMA.

Software: astropy (The Astropy Collaboration et al. 2018, 2022; T. P. Robitaille et al. 2013), scipy (P. Virtanen et al. 2020), emcee (D. Foreman-Mackey et al. 2013), dynesty (J. S. Speagle 2020), MOSFIT (J. Guillochon et al. 2018), numpy (S. Van Der Walt et al. 2011; C. R. Harris et al. 2020), linetools, photutils (L. Bradley et al. 2025), casa (CASA Team et al. 2022), lpipe (D. A. Perley 2019), spectres (A. C. Carnall & C. A. Carnall 2017), prospector (B. D. Johnson et al. 2021), fsps (C. Conroy et al. 2010), python-fsps (B. Johnson et al. 2024), sfdmap, swifttools,[23] heasoft (NASA High Energy Astrophysics Science Archive Research Center (HEASARC) 2014), extinction, sedpy (D. B. Johnson 2019), statsmodels (S. Seabold & J. Perktold 2010), scamp (C. Gabriel et al. 2006), swarp (E. Bertin 2010).

Appendix A
Details of Observations

In Tables 4, 5, 6, 7, 8, 9, 10, 11, and 12, we provide the details of our observations, as described in Section 5.1.2.

Table 4
P60/SEDM Observation Summary

Date	MJD	Filter	Mag	Mag Error	Limiting Mag
2024-08-01	60523.2	*u*	19.58	0.13	20.14
		u	19.58	0.45	18.78
		r	20.066	0.049	21.69
		i	20.391	0.077	21.52
2024-08-02	60524.2	*u*	19.51	0.16	19.87
		u	19.51	0.18	19.75
		r	20.152	0.063	21.49
		i	20.28	0.11	21.03
2024-08-14	60536.2	*g*	21.16	0.19	21.32
	60543.2	*g*	21.52	0.20	21.61
2024-08-22	60544.2	*g*	21.78	0.22	21.75
		i	21.35	0.18	21.55

Note. Summary of P60/SEDM Observations. Limiting mags correspond to the 5σ sensitivity of each observation.

Table 5
Lowell Discovery Telescope Observations

Filter	Mag	Mag Error
u	22.101	0.068
g	22.220	0.054
r	22.417	0.062
i	22.43	0.12
z	21.94	T0.31

Note. Summary of Lowell Discovery Telescope Observations on 2024 August 27 (MJD 60549).

Table 6
Liverpool Telescope Observations

Date	MJD	Filter	Mag	Mag Error	Limiting Mag
2024-08-05	60527.97	*u*	19.85	0.15	19.27
		g	20.27	0.08	20.71
		r	20.53	0.08	21.15
		i	20.9	0.1	21.26
2024-08-06	60528.96	*u*	19.92	0.11	19.98
		g	20.33	0.05	21.3
		r	20.91	0.07	21.61
		i	21.04	0.06	21.98
2024-08-08	60530.96	*u*	20.2	0.13	20.07
		g	20.61	0.06	21.36
		r	21.15	0.09	21.63
		i	21.09	0.07	21.86
2024-08-15	60537.89	*u*	20.84	0.31	19.59
		g	21.83	0.29	20.86
		r	21.58	0.2	21.17
		i	21.32	0.13	21.5
2024-08-16	60538.96	*u*	19.97	0.26	18.53
		g	20.78	0.19	20.2
		r	21.6	0.32	20.36
		i	21.62	0.28	20.54
2024-08-18	60540.87	*g*	20.41	0.22	20.1
		r	21.45	1.07	20.4
		i	22.52	0.92	20.87
2024-08-19	60541.87	*u*	20.34	0.45	25.93
		g	21.1	0.51	27.14
		i	21.33	0.54	27.84
2024-08-20	60542.88	*i*	21.43	0.22	19.16

Note. Summary of Liverpool Telescope Observations.

[23] https://www.swift.ac.uk/API

Table 7
Swift/UVOT Observations

Date	MJD	ObsID	Band	Exposure (s)	Mag	Mag Error	Limiting Mag
2024-08-03	60525.8	0016746001	*u*	165.1	19.9	0.2	⋯
⋯	⋯	⋯	*u*	165.2	19.7	0.2	⋯
⋯	⋯	⋯	*m*2	495.8	20.6	0.2	⋯
⋯	⋯	⋯	*w*2	601.5	20.8	0.1	⋯
2024-08-12	60535.0	0016746002	*u*	148.4	⋯	⋯	20.2
⋯	⋯	⋯	*m*2	444.7	⋯	⋯	20.4
⋯	⋯	⋯	*w*1	296.0	⋯	⋯	20.6
⋯	⋯	⋯	*w*2	544.8	21.4	0.2	⋯
2024-08-16	60538.5	0016746003	*m*2	323.6	⋯	⋯	20.8
⋯	⋯	⋯	*w*2	403.0	⋯	⋯	21.5

Note. Summary of Swift/UVOT Observations. We report 5σ limiting magnitudes for the cases where the detection significance is $<5\sigma$.

Table 8
Swift/XRT Observations

Date	MJD	ObsID	Exposure (s)	Counts s^{-1}	Flux (10^{-13} erg cm^{-2} s^{-1})
2024-08-03	60525.8	16746001	3671.3	$0.0019^{+0.0011}_{-0.0008}$	$0.8^{+0.5}_{-0.4}$
2024-08-12	60535.0	16746002	1476.8	$0.001^{+0.0019}_{-0.001}$	<4.1
2024-08-16	60538.5	16746003	2783.2	$0.0023^{+0.0017}_{-0.0012}$	<3.8
2024-08-20	60542.6	16746004	2482.2	$0.0005^{+0.001}_{-0.0005}$	<2.2
2024-10-30	60613.0	16746005	2061.1	$0.0009^{+0.0012}_{-0.0007}$	<2.7
2024-11-02	60616.2	16746006	2805.7	$0.0006^{+0.0008}_{-0.0005}$	<1.9
2024-11-05	60619.0	16746007	2657.9	$0.0^{+0.0009}_{0.0}$	<1.6
2024-11-08	60622.4	16746008	2710.4	$0.0034^{+0.0024}_{-0.0017}$	<5.5

Note. Summary of Swift/XRT Observations. Fluxes are computed assuming $\Gamma = 1.7$. Upper limits are 3σ.

Table 9
XMM-Newton Observations

Date	MJD	ObsID	Instrument	Exposure (s)	Count Rate (10^{-2} ct s^{-1})	Flux (10^{-13} erg cm^{-2} s^{-1})
2024-08-14	60536	0953011201	EPIC-PN	3873	4.04 ± 0.35	2.65 ± 0.15
			EPIC-MOS1	12,370	1.19 ± 0.12	⋯
			EPIC-MOS2	13,660	0.98 ± 0.09	⋯
2024-09-05	60558	0953011301	EPIC-PN	12,940	0.34 ± 0.12	0.12 ± 0.04
			EPIC-MOS1	23,700	0.033 ± 0.033	⋯
			EPIC-MOS2	27,790	0.017 ± 0.042	⋯
2024-11-30	60644	0953012101	EPIC-PN	27,090	0.175 ± 0.052	0.12 ± 0.02
			EPIC-MOS1	37,470	0.045 ± 0.020	⋯
			EPIC-MOS2	39,130	0.050 ± 0.020	⋯

Note. Summary of XMM-Newton Observations. Exposure times are quoted after accounting for good time interval flagging. We compute unabsorbed fluxes from (observed) 0.3–10 keV by jointly fitting the spectra to a power-law model with a photon-index tied between observations and flux tied between instruments for each observation.

Table 10
NuSTAR Observations

Date	MJD	ObsID	FPM	Exposure (s)	Counts		Flux 90% Upper Limit (10^{-13} erg cm^{-2} s^{-1}]
					src	bkg	
2024-09-06	60559.2	91001632002	A	24,879.3	205	207	0.52
			B	24,622.1	242	251	0.57
2024-09-07	60560.7	91001632004	A	37,667.2	302	294	0.70
			B	37,284.5	376	370	0.73

Note. Summary of NuSTAR Observations. Flux upper limits are at the 90% confidence level, computed assuming an unabsorbed power law with $\Gamma = 1.77$ for the 3–79 keV band.

Table 11
Keck I/LRIS Observations

Date	MJD	Exposure (s)	Airmass	Standard (Spec.)	Slit Width (Spec.)
2024-07-29	60520.4	600	1.33	BD+28	1.″0
2024-08-05	60527.3	1800	1.20	BD+28	1.″0
2024-09-07	60560.3	4500	1.42	Feige 110	1.″0
2024-10-07	60590.2	7200	1.82	G191-B2B	1.″0

Note. Summary of Keck I/LRIS observations.

Table 12
HST/WFC3 Observation Summary

Date	MJD	Detector	Filter	Exposure (s)
2024-09-30	60583	UVIS	F606W	994
2024-09-30	60583	UVIS	F336W	1073
2024-09-30	60583	UVIS	F105W	1059
2024-09-30	60583	UVIS	F160W	1059

Appendix B
Chance Association Probability

In this section, we compute the probability that 24puz randomly lies at its location with respect to nearby galaxies. If 24puz were associated with an unrelated background source, it would have a uniform probability of lying at any location in the field. We assess the probability that 24puz, if unassociated with any detected galaxy, would be located at the observed position with respect to the detected galaxies. Because of the limited field of view of our HST observation, we perform this experiment using observations of the Cosmological Evolution Survey (COSMOS; N. Scoville et al. 2007) field as part of the Cosmic Assembly Near-infrared Deep Extragalactic Legacy Survey (CANDELS; N. A. Grogin et al. 2011; A. M. Koekemoer et al. 2011), which were performed with the HST Advanced Camera for Surveys (ACS)/WFC instrument and include F606W measurements. While the filter throughputs and pixel scales are slightly different for ACS/WFC F606W and WFC3/UVIS F606W images, we estimate that they cause percent-level changes in the measured fluxes and Kron radii, which are negligible for our purposes. We retrieved `sextractor` catalogs for the CANDELS field from H. Nayyeri et al. (2017).

We compute the random association probability as follows. First, we correct for the increased depth of the CANDELS image. We randomly assign each COSMOS source a per-pixel rms noise from the observed per-pixel noises in our observations and define detectable sources as those with a total signal-to-noise (i.e., integrated over the entire source rather than per-pixel) larger than 3, which is our detection threshold.

We treat the undetected sources as a random sample of background sources and compute the distances from each to the nth nearest neighbors, in units of Kron radii, for $n = 1$–10. We only consider galaxies within 20″ given the distance from 24puz to the edge of the observation field. We use these distances to compute two probabilities. First, we consider the nearest galaxy to 24puz, which we will denote "G1" hereafter. We compute the probability of finding the nearest neighbor closer than the distance G1 for randomly located sources. We find a probability $p_1 = 3 \times 10^{-4}$ of the nearest neighbor being closer than G1. Second, we compute the probability that all the second through 10th-nearest neighbors are closer than those observed for 24puz: $p_{2-10} = 1.3 \times 10^{-3}$. It is thus unlikely both that 24puz lies close to the observed galaxies by chance (3σ) or that 24puz lies close to G1 by chance (3.4σ).

Appendix C
Implications If AT 2024puz Is at $z > 0.356$

We briefly consider the possibility that 24puz is a background source, and so at $z > 0.356$. In this case, the rest-frame timescale of 24puz could be more consistent with typical LFBOTs, but the luminosity would become even more extreme (at $z = 1$, $L_{\rm optUV} \approx 10^{46}$ erg s^{-1}). Moreover, the intrinsic temperature of the optical/UV would become hotter with increasing redshift. The best-fit X-ray power-law slope would be softer—leading to better consistency with TDEs—and the X-ray variability timescale would shorten. The red excess would move to bluer wavelengths. Importantly, if 24puz is at sufficiently high redshift, a massive, quenched host galaxy is allowed, in which case we can invoke an SMBH to explain the event. However, to our knowledge, there are no models to explain fast, luminous flares from SMBH. Instead, 24puz would more likely be an LFBOT, but at an even more extreme luminosity.

Appendix D
Ultraviolet-infrared Spectral Energy Distributions and Best-fit Parameters

In Figure 16, we show the multiepoch, best-fit blackbody models. In Table 13, we tabulate the best-fit parameters.

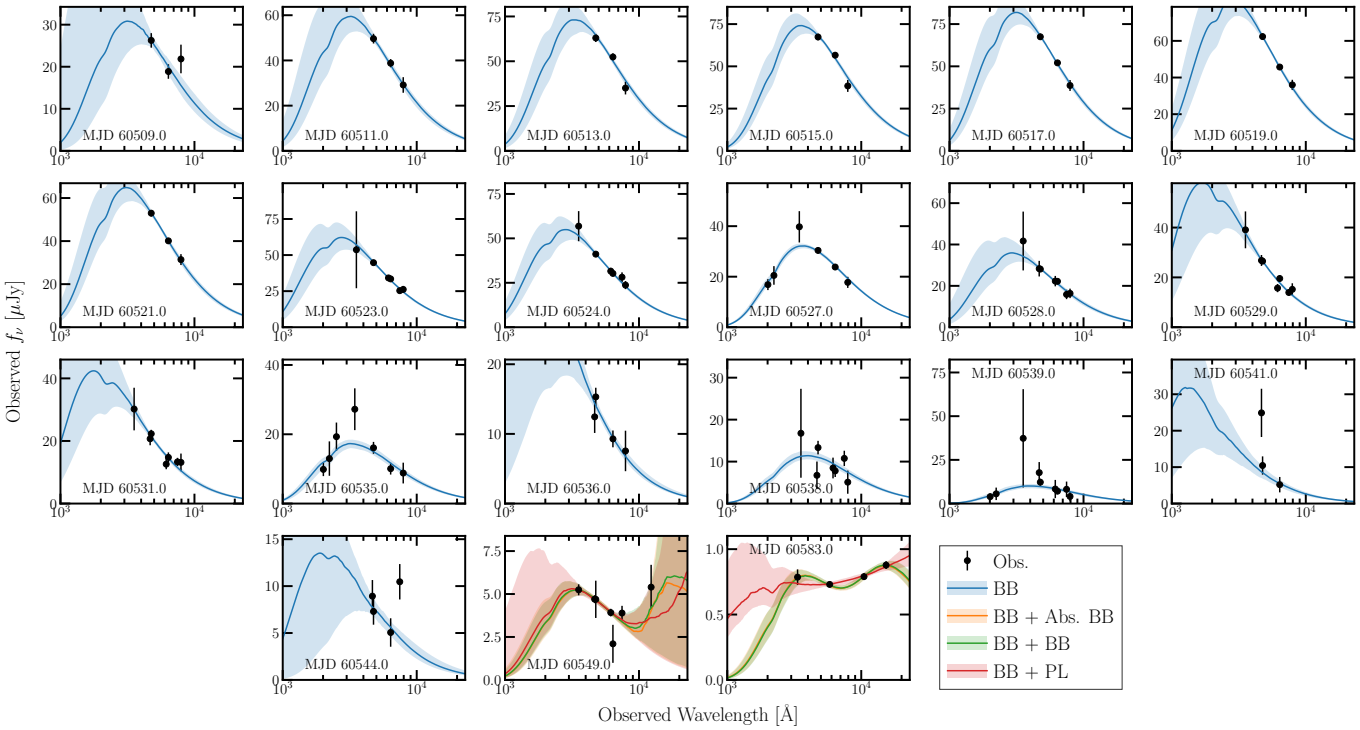

Figure 16. Blackbody fits to each epoch of UV/optical imaging of 24puz, as described in Section 4.2. The fits are shown as colored bands, and the data as black scatter points.

Table 13
UVOIR Blackbody Modeling

Date	MJD	Model	$\log \frac{T_{bb}}{\mathrm{K}}$	$\log \frac{R_{bb}}{\mathrm{cm}}$	$\log \frac{L_{bb}}{\mathrm{erg\ s^{-1}}}$	M_g (mag)	$\log \frac{T_{\mathrm{IR}}}{\mathrm{K}}$	$\log \frac{R_{\mathrm{IR}}}{\mathrm{cm}}$	Γ_{IR}	$\log \frac{L_{\mathrm{IR}}}{\mathrm{erg\ s^{-1}}}$
2024-07-18	60509	BB	$4.37^{+0.18}_{-0.13}$	$15.06^{+0.14}_{-0.17}$	$44.44^{+0.4}_{-0.24}$	$-20.56^{+0.101}_{-0.069}$	...	...	...	...
2024-07-20	60511	BB	$4.37^{+0.081}_{-0.064}$	$15.197^{+0.066}_{-0.074}$	$44.73^{+0.17}_{-0.13}$	$-21.249^{+0.052}_{-0.052}$	...	...	...	...
2024-07-22	60513	BB	$4.336^{+0.055}_{-0.046}$	$15.288^{+0.049}_{-0.054}$	$44.774^{+0.114}_{-0.091}$	$-21.55^{+0.032}_{-0.033}$	...	...	...	...
2024-07-24	60515	BB	$4.309^{+0.04}_{-0.039}$	$15.333^{+0.042}_{-0.042}$	$44.751^{+0.08}_{-0.067}$	$-21.646^{+0.035}_{-0.033}$	...	...	...	...
2024-07-26	60517	BB	$4.377^{+0.056}_{-0.048}$	$15.257^{+0.046}_{-0.054}$	$44.871^{+0.118}_{-0.094}$	$-21.581^{+0.037}_{-0.035}$	...	...	...	...
2024-07-28	60519	BB	$4.425^{+0.056}_{-0.051}$	$15.189^{+0.046}_{-0.05}$	$44.93^{+0.12}_{-0.11}$	$-21.451^{+0.032}_{-0.027}$	...	...	...	...
2024-07-30	60521	BB	$4.384^{+0.057}_{-0.048}$	$15.195^{+0.048}_{-0.053}$	$44.775^{+0.124}_{-0.095}$	$-21.295^{+0.032}_{-0.031}$	...	...	...	...
2024-08-01	60523	BB	$4.436^{+0.073}_{-0.055}$	$15.106^{+0.05}_{-0.063}$	$44.81^{+0.17}_{-0.12}$	$-21.077^{+0.022}_{-0.026}$	...	...	...	...
2024-08-02	60524	BB	$4.423^{+0.068}_{-0.055}$	$15.102^{+0.051}_{-0.058}$	$44.75^{+0.15}_{-0.12}$	$-21.006^{+0.032}_{-0.037}$	...	...	...	...
2024-08-05	60527	BB	$4.299^{+0.014}_{-0.015}$	$15.164^{+0.019}_{-0.016}$	$44.377^{+0.029}_{-0.027}$	$-20.751^{+0.028}_{-0.039}$	...	...	...	...
2024-08-06	60528	BB	$4.397^{+0.086}_{-0.068}$	$15.046^{+0.069}_{-0.078}$	$44.54^{+0.19}_{-0.14}$	$-20.613^{+0.049}_{-0.038}$	...	...	...	...
2024-08-07	60529	BB	$4.61^{+0.15}_{-0.11}$	$14.84^{+0.09}_{-0.11}$	$44.96^{+0.37}_{-0.26}$	$-20.431^{+0.049}_{-0.038}$	...	...	...	...
2024-08-09	60531	BB	$4.58^{+0.18}_{-0.12}$	$14.82^{+0.11}_{-0.13}$	$44.8^{+0.46}_{-0.29}$	$-20.205^{+0.055}_{-0.061}$	...	...	...	...
2024-08-13	60535	BB	$4.345^{+0.03}_{-0.031}$	$14.966^{+0.041}_{-0.046}$	$44.157^{+0.052}_{-0.055}$	$-19.966^{+0.093}_{-0.084}$	...	...	...	...
2024-08-14	60536	BB	$4.66^{+0.23}_{-0.21}$	$14.66^{+0.17}_{-0.15}$	$44.83^{+0.6}_{-0.49}$	$-19.74^{+0.07}_{-0.11}$	...	...	...	...
2024-08-16	60538	BB	$4.268^{+0.028}_{-0.027}$	$14.987^{+0.04}_{-0.039}$	$43.903^{+0.047}_{-0.049}$	$-19.708^{+0.11}_{-0.073}$	...	...	...	...
2024-08-17	60539	BB	$4.253^{+0.05}_{-0.045}$	$14.982^{+0.059}_{-0.075}$	$43.83^{+0.083}_{-0.088}$	$-19.62^{+0.15}_{-0.13}$	...	...	...	...

Table 13
(Continued)

Date	MJD	Model	$\log \frac{T_{bb}}{\mathrm{K}}$	$\log \frac{R_{bb}}{\mathrm{cm}}$	$\log \frac{L_{bb}}{\mathrm{erg\ s^{-1}}}$	M_g (mag)	$\log \frac{T_{\mathrm{IR}}}{\mathrm{K}}$	$\log \frac{R_{\mathrm{IR}}}{\mathrm{cm}}$	Γ_{IR}	$\log \frac{L_{\mathrm{IR}}}{\mathrm{erg\ s^{-1}}}$
2024-08-19	60541	BB	$4.78^{+0.17}_{-0.25}$	$14.47^{+0.16}_{-0.11}$	$44.91^{+0.47}_{-0.64}$	$-19.19^{+0.25}_{-0.14}$	⋯	⋯	⋯	⋯
2024-08-22	60544	BB	$4.55^{+0.29}_{-0.25}$	$14.63^{+0.24}_{-0.21}$	$44.3^{+0.74}_{-0.55}$	$-19.15^{+0.14}_{-0.15}$	⋯	⋯	⋯	⋯
2024-08-27	60549	BB+BB	$4.33^{+0.07}_{-0.046}$	$14.728^{+0.055}_{-0.083}$	$43.624^{+0.118}_{-0.074}$	$-18.72^{+0.122}_{-0.063}$	$3.41^{+0.19}_{-0.26}$	$17.6^{+1.0}_{-1.4}$	$42.7^{+0.7}_{-5.8}$ ⋯	
⋯	⋯	BB+Dust	$4.33^{+0.07}_{-0.046}$	$14.728^{+0.055}_{-0.083}$	$43.624^{+0.118}_{-0.074}$	$-18.72^{+0.122}_{-0.063}$	$3.42^{+0.2}_{-0.27}$	$16.0^{+1.07}_{-0.68}$	⋯	$42.8^{+0.9}_{-1.2}$
⋯	⋯	BB+PL	$4.33^{+0.07}_{-0.046}$	$14.728^{+0.055}_{-0.083}$	$43.624^{+0.118}_{-0.074}$	$-18.72^{+0.122}_{-0.063}$	⋯	⋯	$2.3^{+1.7}_{-1.4}$	$44.6^{+4.8}_{-7.6}$
2024-09-30	60583	BB+BB	$4.284^{+0.045}_{-0.039}$	$14.385^{+0.051}_{-0.054}$	$42.756^{+0.078}_{-0.057}$	$-16.778^{+0.048}_{-0.064}$	$3.584^{+0.033}_{-0.032}$	$17.075^{+0.058}_{-0.055}$	$41.95^{+0.021}_{-0.034}$ ⋯	
⋯	⋯	BB+Dust	$4.284^{+0.045}_{-0.039}$	$14.385^{+0.051}_{-0.054}$	$42.756^{+0.078}_{-0.057}$	$-16.778^{+0.048}_{-0.064}$	$3.586^{+0.029}_{-0.032}$	$15.375^{+0.057}_{-0.049}$	⋯	$41.948^{+0.027}_{-0.028}$
⋯	⋯	BB+PL	$4.284^{+0.045}_{-0.039}$	$14.385^{+0.051}_{-0.054}$	$42.756^{+0.078}_{-0.057}$	$-16.778^{+0.048}_{-0.064}$	⋯	⋯	$0.23^{+0.24}_{-0.17}$	$42.684^{+0.058}_{-0.056}$

Appendix E
X-Ray Spectral Modeling

The best-fit spectral parameters of our MJD 60558 XMM-Newton observations are shown in Figure 17.

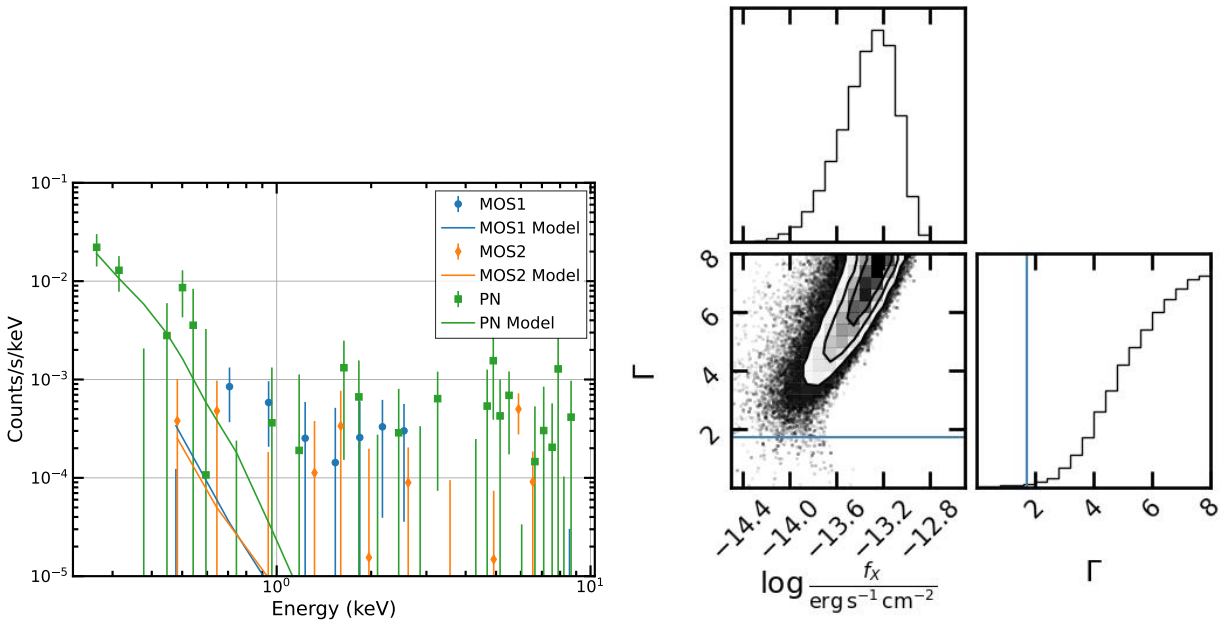

Figure 17. Spectral constraints from the MJD 60558 (37.6 rest-day) XMM-Newton observations, in the same format as Figure 10. We assume no absorption in this fit, based on the results from the higher signal-to-noise MJD 60536 observations. The photon-index from the first epoch is shown in blue. The photon-index has tentatively softened: the probability that the photon-index is consistent with the first epoch is $P(\Gamma \leqslant 1.73) = 1\%$.

Appendix F
The Compton Equilibrium Temperature

Given the strong X-ray source associated with 24puz, the electron temperature may be hotter than the standard photoionization equilibrium temperature $\sim 10^4$ K due to Compton heating (A. Y. Q. Ho et al. 2019). We compute the Compton equilibrium temperature T_C as follows. The Compton heating rate per unit density is given by S. Y. Sazonov et al. (2004) and A. Y. Q. Ho et al. (2019):

$$H(\nu) = \frac{\sigma_T}{m_e c^2} \int_0^\infty h\nu f_\nu a\left(\frac{h\nu}{m_e c^2}\right) d\nu, \tag{F1}$$

where f_ν is the incident flux density, ν is frequency, and all constants are given with standard symbols. The function $a\left(\frac{h\nu}{m_e c^2}\right)$ accounts for Klein–Nishina corrections and, for $k_B T_C \ll m_e c^2$, is given by

$$\begin{aligned} a(x) &= \frac{3}{8x^4}(x-3)(x+1)\ln(2x+1) \\ &\quad + \frac{-10x^4 + 51x^3 + 93x^2 + 51 + 9}{4x^3(2x+1)^3} \\ &\approx 1 - \frac{21x}{5} + \mathcal{O}(x^2). \end{aligned} \tag{F2}$$

For many astropysical systems, including 24puz, the heating is dominated by photons with $h\nu \gtrsim 10$ keV, i.e., hard X-rays.

The cooling rate is given by

$$C(\nu) = \frac{4k_B T \sigma_T}{m_e c^2} \int_0^\infty f_\nu b\left(\frac{h\nu}{m_e c^2}\right) d\nu. \tag{F3}$$

Here, T is the temperature of the irradiated region, and $b\left(\frac{h\nu}{m_e c^2}\right)$ accounts for Klein–Nishina corrections. The latter is given by

$$\begin{aligned} b(x) &= \frac{1}{4}\left(\frac{3(3x^2 2 - 4x - 13)}{16x^3}\ln(2x+1)\right. \\ &\quad + \frac{-216x^6 + 476x^5 + 2066x^4}{8x^2(2x+1)^5} \\ &\quad \left. + \frac{2429x^3 + 1353x^2 + 363x + 39}{8x^2(2x+1)^5}\right) \\ &\approx 1 - \frac{47x}{8} + \mathcal{O}(x^2). \end{aligned} \tag{F4}$$

Once again, this expression is valid for $k_B T_C \ll m_e c^2$. Compton cooling is dominated by photons with $h\nu \lesssim 10$ keV.

The temperature evolution is then given by $(3/2)k_B dT/dt = H(\nu) - C(\nu)$. The temperature reaches an equilibrium T_C when the heating and cooling rates are equal, or

$$T_C = \frac{1}{4k_B} \frac{\int_0^\infty h\nu f_\nu a\left(\frac{h\nu}{m_e c^2}\right) d\nu}{\int_0^\infty f_\nu b\left(\frac{h\nu}{m_e c^2}\right) d\nu}. \tag{F5}$$

Extrapolating from the optical/UV and X-ray observations of 24puz described in Sections 4.2 and 5.1.3 to typical values during our radio observation, we assume that f_ν is the sum of a blackbody with $T \approx 10^{4.3}$ K and $\log L_{\rm OptUV}/({\rm erg\ s^{-1}}) \approx 43.5$ and a power law with $\Gamma = 1.77$ and $L_X/({\rm erg\ s^{-1}}) \approx 42.2$, where we cut off the power law at 0.3 keV. These values are most appropriate during our final epoch of radio observations, but we verified that the equilibrium temperature does not change significantly by adopting values appropriate for earlier observations. We find $T_C = 4 \times 10^5$ K, and this equilibrium temperature is reached in $\sim$days. An increased optical/UV luminosity will decrease the temperature, while an increased X-ray component will increase the temperature. We tested a range of optical/UV and X-ray luminosity and found $T_C \gtrsim 10^5$ K for most reasonable assumptions. As can be seen from Equation (3) (or Equation (10.16) of B. T. Draine 2011), in the radio regime, where $h\nu \ll kT_e$, increasing the temperature tends to decrease τ_{ff}, so we conservatively adopt $T_e = 10^5$ K.

Appendix G
MOSFIT

In Figure 18, we show the full set of best-fit parameters found by `MOSFIT`. The parameter definitions are detailed in B. Mockler et al. (2019).

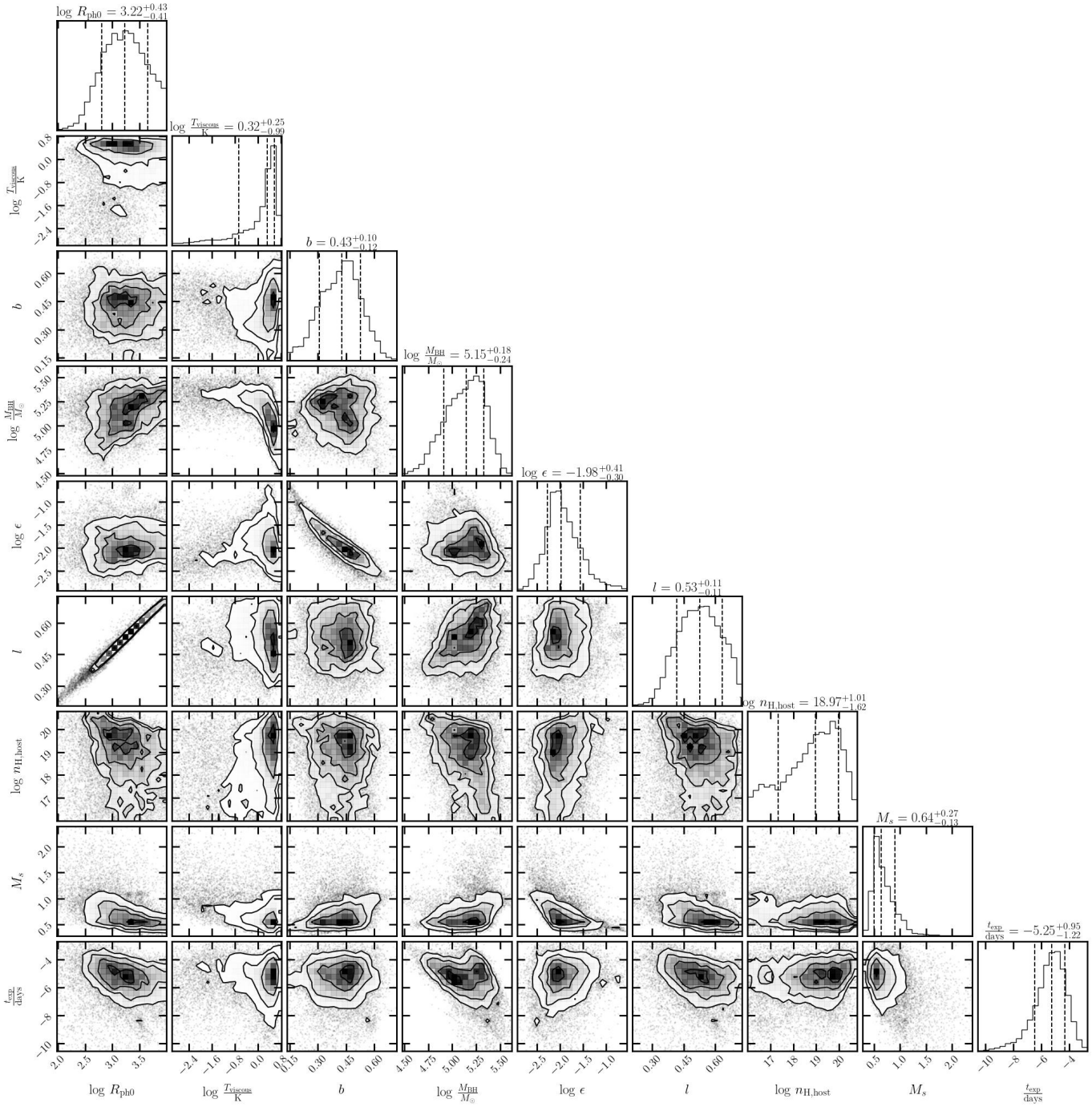

Figure 18. Corner plot showing the full `MOSFIT` parameter set.

ORCID iDs

Jean J. Somalwar https://orcid.org/0000-0001-8426-5732
Vikram Ravi https://orcid.org/0000-0002-7252-5485
Raffaella Margutti https://orcid.org/0000-0003-4768-7586
Ryan Chornock https://orcid.org/0000-0002-7706-5668
Priyamvada Natarajan https://orcid.org/0000-0002-5554-8896
Wenbin Lu https://orcid.org/0000-0002-1568-7461
Charlotte Angus https://orcid.org/0000-0002-4269-7999
Matthew J. Graham https://orcid.org/0000-0002-3168-0139
Erica Hammerstein https://orcid.org/0000-0002-5698-8703
Edward Nathan https://orcid.org/0000-0002-9633-9193
Matt Nicholl https://orcid.org/0000-0002-2555-3192
Kritti Sharma https://orcid.org/0000-0002-4477-3625
Robert Stein https://orcid.org/0000-0003-2434-0387
Frank Verdi https://orcid.org/0009-0005-3565-4164
Yuhan Yao https://orcid.org/0000-0001-6747-8509
Eric C. Bellm https://orcid.org/0000-0001-8018-5348
Tracy X. Chen https://orcid.org/0000-0001-9152-6224
Michael W. Coughlin https://orcid.org/0000-0002-8262-2924
Mansi M. Kasliwal https://orcid.org/0000-0002-5619-4938
Russ R. Laher https://orcid.org/0000-0003-2451-5482
Reed Riddle https://orcid.org/0000-0002-0387-370X
Jesper Sollerman https://orcid.org/0000-0003-1546-6615

References

Abbott, B. P., Abbott, R., Abbott, T. D., et al. 2019, ApJL, 882, L24
Ade, P. A., Aghanim, N., Arnaud, M., et al. 2016, A&A, 594, 63
Albareti, F. D., Allende Prieto, C., Almeida, A., et al. 2017, ApJS, 233, 25
Alexander, K. D., van Velzen, S., Horesh, A., & Zauderer, B. A. 2020, Radio Properties of Tidal Disruption Events (Berlin: Springer)
Alexander, T., & Natarajan, P. 2014, Sci, 345, 1330
Anand, A., Kauffmann, G., & Nelson, D. 2022, MNRAS, 513, 3210
Andreoni, I., Coughlin, M. W., Perley, D. A., et al. 2022, Natur, 612, 430
Angus, C. R., Baldassare, V. F., Mockler, B., et al. 2022, NatAs, 6, 1452
Arcavi, I., Gal-Yam, A., Sullivan, M., et al. 2014, ApJ, 793, 38
Arnett, W. D., & Arnett, D. W. 1982, ApJ, 253, 785
Barbary, K. 2016, JOSS, 1, 58
Bekenstein, J. D. 1973, ApJ, 183, 657
Bellm, E. C., Kulkarni, S. R., Barlow, T., et al. 2019a, PASP, 131, 068003
Bellm, E. C., Kulkarni, S. R., Graham, M. J., et al. 2019b, PASP, 131, 018002
Ben Bekhti, N., Flöer, L., Keller, R., et al. 2016, A&A, 594, A116
Bertin, E., 2010 Astrophysics Source Code Library, ascl:1010.068
Bertin, E., Arnouts, S., Bertin, E., & Arnouts, S. 1996, A&AS, 117, 393
Blagorodnova, N., Cenko, S. B., Kulkarni, S. R., et al. 2019, ApJ, 873, 92
Blagorodnova, N., Gezari, S., Hung, T., et al. 2017, ApJ, 844, 46
Blagorodnova, N., Neill, J. D., Walters, R., et al. 2018, PASP, 130, 035003
Bloom, J. S., Giannios, D., Metzger, B. D., et al. 2011, Sci, 333, 203
Bradley, L., Sipőcz, B., Robitaille, T., et al. 2025, zndo, Zenodo, doi:10.5281/ZENODO.596036
Bright, J. S., Margutti, R., Matthews, D., et al. 2022, ApJ, 926, 112
Brown, G. C., Levan, A. J., Stanway, E. R., et al. 2015, MNRAS, 452, 4297
Burrows, D. N., Kennea, J. A., Ghisellini, G., et al. 2011, Natur, 476, 421
Carnall, A. C., & Carnall, C. A. 2017, arXiv:1705.05165
CASA Team, Bean, B., Bhatnagar, S., et al. 2022, PASP, 134, 114501
Cash, W. 1979, ApJ, 228, 939
Cendes, Y., Berger, E., Alexander, K. D., et al. 2024, ApJ, 971, 185
Cenko, S. B., Krimm, H. A., Horesh, A., et al. 2012, ApJ, 753, 77
Chambers, K. C., Magnier, E. A., Metcalfe, N., et al. 2016, arXiv:1612.05560
Charalampopoulos, P., Pursiainen, M., Leloudas, G., et al. 2023, A&A, 673, A95
Chen, C., & Shen, R.-F. 2024, ApJ, 991, 10
Chen, Y., Drout, M. R., Piro, A. L., et al. 2023a, ApJ, 955, 43
Chen, Y., Drout, M. R., Piro, A. L., et al. 2023b, ApJ, 955, 42
Chrimes, A. A., Coppejans, D. L., Jonker, P. G., et al. 2024a, A&A, 691, A329
Chrimes, A. A., Jonker, P. G., Levan, A. J., et al. 2024b, MNRAS, 527, L47
Conroy, C., Gunn, J. E., Conroy, C., & Gunn, J. E., 2010 Astrophysics Source Code Library, ascl:1010.043
Coppejans, D. L., Margutti, R., Terreran, G., et al. 2020, ApJL, 895, L23
Coughlin, M. W., Bloom, J. S., Nir, G., et al. 2023, ApJS, 267, 31
Cutri, R. M., Skrutskie, M. F., van Dyk, S., et al. 2003, The IRSA 2MASS All-Sky Point Source Catalog, NASA/IPAC Infrared Science Archive (tmc)
Dai, L., McKinney, J. C., & Miller, M. C. 2015, ApJL, 812, L39
De, K., Hankins, M. J., Kasliwal, M. M., et al. 2020, PASP, 132, 025001
Dekany, R., Smith, R. M., Riddle, R., et al. 2020, PASP, 132, 038001
Devecchi, B., & Volonteri, M. 2009, ApJ, 694, 302
Draine, B. T. 2011, Physics of the Interstellar and Intergalactic Medium (Princeton Univ. Press)
Draine, B. T., & Li, A. 2007, ApJ, 657, 810
Earl, N., French, K. D., Ramirez-Ruiz, E., et al. 2025, ApJ, 983, 28
Elbert, O. D., Bullock, J. S., & Kaplinghat, M. 2018, MNRAS, 473, 1186
Evans, C. R., & Kochanek, C. S. 1989, ApJL, 346, L13
Fitzpatrick, E. 1999, PASP, 111, 63
Foreman-Mackey, D., Hogg, D. W., Lang, D., & Goodman, J. 2013, PASP, 125, 306
Fransson, C., Lundqvist, P., & Chevalier, R. A. 1996, ApJ, 461, 993
Fremling, C., Miller, A. A., Sharma, Y., et al. 2020, ApJ, 895, 32
Gabriel, C., Arviset, C., Ponz, D., Solano, E., & Bertin, E. 2006, ASPC, 351, 112
Gehrels, N., Chincarini, G., Giommi, P., et al. 2004, ApJ, 611, 1005
Gezari, S., Basa, S., Martin, D. C., et al. 2008, ApJ, 676, 944
Gezari, S., Martin, D. C., Milliard, B., et al. 2006, ApJL, 653, L25
González, J. A., Hannam, M., Sperhake, U., Brügmann, B., & Husa, S. 2007, PhRvL, 98, 231101
Graham, M. J., Kulkarni, S. R., Bellm, E. C., et al. 2019, PASP, 131, 078001
Greene, J. E., Strader, J., & Ho, L. C. 2020, ARA&A, 58, 257
Grogin, N. A., Kocevski, D. D., Faber, S. M., et al. 2011, ApJS, 197, 35
Guillochon, J., Nicholl, M., Villar, V. A., et al. 2018, ApJS, 236, 6
Guolo, M., Gezari, S., Yao, Y., et al. 2024, ApJ, 966, 160
Gutiérrez, C. P., Mattila, S., Lundqvist, P., et al. 2024, ApJ, 977, 21
Hammerstein, E., Gezari, S., van Velzen, S., et al. 2021, ApJL, 908, L20
Hammerstein, E., van Velzen, S., Gezari, S., et al. 2023, ApJ, 942, 9
Harris, C. R., Millman, K. J., van der Walt, S. J., et al. 2020, Natur, 585, 357
Harrison, F. A., Craig, W. W., Christensen, F. E., et al. 2013, ApJ, 770, 103
Hills, J. G. 1975, Natur, 254, 295
Hinkle, J. T., Holoien, T. W., Auchettl, K., et al. 2020, MNRAS, 500, 1673
Hinkle, J. T., Tucker, M. A., Shappee, B. J., et al. 2023, MNRAS, 519, 2035
Ho, A. Y. Q., Margalit, B., Bremer, M., et al. 2022, ApJ, 932, 116
Ho, A. Y. Q., Perley, D. A., Gal-Yam, A., et al. 2023, ApJ, 949, 120
Ho, A. Y. Q., Perley, D. A., Kulkarni, S. R., et al. 2020, ApJ, 895, 49
Ho, A. Y. Q., Phinney, E. S., Ravi, V., et al. 2019, ApJ, 871, 73
Ho, A. Y. Q., Yao, Y., Matsumoto, T., et al. 2025, ApJ, 989, 16
Holoien, T. W.-S., Auchettl, K., Tucker, M. A., et al. 2020, ApJ, 898, 161
Holoien, T. W. S., Kochanek, C. S., Prieto, J. L., et al. 2016, MNRAS, 463, 3813
Holoien, T. W. S., Prieto, J. L., Bersier, D., et al. 2014, MNRAS, 445, 3263
Holoien, T. W.-S., Vallely, P. J., Auchettl, K., et al. 2019, ApJ, 883, 111
Hoogendam, W. B., Hinkle, J. T., Shappee, B. J., et al. 2024, MNRAS, 530, 4501
Huang, Y.-H., Chen, H.-W., Shectman, S. A., et al. 2021, MNRAS, 502, 4743
Inayoshi, K., Visbal, E., & Haiman, Z. 2020, ARA&A, 58, 27
Inkenhaag, A., Jonker, P. G., Levan, A. J., et al. 2023, MNRAS, 525, 4042
Jiang, Y.-F., & Dai, L. 2024, arXiv:2408.16856
Jiang, Y. F., Stone, J. M., & Davis, S. W. 2014, ApJ, 796, 106
Johnson, B., Foreman-Mackey, D., Sick, J., et al. 2024, Zenodo, doi:10.5281/ZENODO.12447779
Johnson, D. B., 2019 Astrophysics Source Code Library, ascl:1905.026
Johnson, B. D., Leja, J., Conroy, C., & Speagle, J. S. 2021, ApJS, 254, 22
Karamehmetoglu, E., Taddia, F., Sollerman, J., et al. 2017, A&A, 602, A93
Kewley, L. J., Geller, M. J., & Jansen, R. A. 2004, AJ, 127, 2002
Khatami, D. K., & Kasen, D. N. 2024, ApJ, 972, 140
King, A., Lasota, J. P., & Middleton, M. 2023, NewAR, 96, 101672
Kirby, E. N., Cohen, J. G., Guhathakurta, P., et al. 2013, ApJ, 779, 102
Kochanek, C. S., Shappee, B. J., Stanek, K. Z., et al. 2017, PASP, 129, 104502
Koekemoer, A. M., Faber, S. M., Ferguson, H. C., et al. 2011, ApJS, 197, 36
Kraft, R. P., Burrows, D. N., & Nousek, J. A. 1991, ApJ, 374, 344
Kremer, K., Lu, W., Piro, A. L., et al. 2021, ApJ, 911, 104
Kremer, K., Spera, M., Becker, D., et al. 2020, ApJ, 903, 45
Leja, J., Johnson, B. D., Conroy, C., Dokkum, P. G. v, & Byler, N. 2017, ApJ, 837, 170
Leja, J., Speagle, J. S., Ting, Y.-S., et al. 2022, ApJ, 936, 165
Li, L., Zhong, S.-Q., Xiao, D., et al. 2024, ApJL, 963, L13
Lidskii, V. V., & Ozernoi, L. M. 1979, PAZh, 5, 28
Lodato, G., & Natarajan, P. 2006, MNRAS, 371, 1813
Loeb, A., & Rasio, F. A. 1994, ApJ, 432, 52
Lu, W., & Bonnerot, C. 2020, MNRAS, 492, 686
Madau, P., & Rees, M. J. 2001, ApJ, 551, L27
Maguire, K., Eracleous, M., Jonker, P. G., MacLeod, M., & Rosswog, S. 2020, SSRv, 216, 39
Margutti, R., Metzger, B. D., Chornock, R., et al. 2019, ApJ, 872, 18
Masci, F. J., Laher, R. R., Rusholme, B., et al. 2019, PASP, 131, 018003
Masci, F. J., Laher, R. R., Rusholme, B., et al. 2023, arXiv:2305.16279
Matthews, D., Margutti, R., Metzger, B. D., et al. 2023, RNAAS, 7, 126
McKinney, J. C., Dai, L., & Avara, M. J. 2015, MNRAS, 454, L6
Metzger, B. D. 2022, ApJ, 932, 84
Metzger, B. D., & Perley, D. A. 2023, ApJ, 944, 74
Migliori, G., Margutti, R., Metzger, B. D., et al. 2024, ApJL, 963, L24
Miller, M. C., & Hamilton, D. P. 2002, ApJ, 576, 894
Mockler, B., Guillochon, J., & Ramirez-Ruiz, E. 2019, ApJ, 872, 151
Nadyozhin, K. D. 1994, ApJS, 92, 527
Nakar, E., & Piro, A. L. 2014, ApJ, 788, 193
NASA High Energy Astrophysics Science Archive Research Center (HEASARC), 2014 Astrophysics Source Code Library, ascl:1408.004
Natarajan, P. 2014, GReGr, 46, 1702
Natarajan, P. 2021, MNRAS, 501, 1413
Nayyeri, H., Hemmati, S., Mobasher, B., et al. 2017, ApJS, 228, 7
Nicholl, M., Srivastav, S., Fulton, M. D., et al. 2023, ApJL, 954, L28
Nicholl, M., Wevers, T., Oates, S. R., et al. 2020, MNRAS, 499, 482
Oke, J. B., Cohen, J. G., Carr, M., et al. 1995, PASP, 107, 375
Osterbrock, D. E., & Ferland, G. J. 2006, Astrophysics of gaseous nebulae and active galactic nuclei (Univ. Science Books)
Pasham, D. R., Ho, W. C., Alston, W., et al. 2022, NatAs, 6, 249
Pasham, D. R., Lucchini, M., Laskar, T., et al. 2023, NatAs, 7, 88
Payne, A. V., Shappee, B. J., Hinkle, J. T., et al. 2021, ApJ, 910, 125
Peres, A. 1962, PhRv, 128, 2471
Perley, D. A. 2019, PASP, 131, 084503

Perley, D. A., Fremling, C., Sollerman, J., et al. 2020, ApJ, 904, 35
Perley, D. A., Ho, A. Y. Q., Yao, Y., et al. 2021, MNRAS, 508, 5138
Perley, D. A., Mazzali, P. A., Yan, L., et al. 2019, MNRAS, 484, 1031
Phinney, E. S. 1989, in IAU Symp. 136, The Center of the Galaxy, ed. M. Morris (Cambridge: Cambridge Univ. Press), 543
Prentice, S. J., Maguire, K., Smartt, S. J., et al. 2018, ApJL, 865, L3
Pursiainen, M., Killestein, T. L., Kuncarayakti, H., et al. 2024, MNRAS, 537, 3298
Rees, M. J. 1988, Natur, 333, 523
Reines, A. E., & Volonteri, M. 2015, ApJ, 813, 82
Repetto, S., Davies, M. B., & Sigurdsson, S. 2012, MNRAS, 425, 2799
Reynolds, C. S., & Reynolds, S. C. 1999, ASPC, 161, 178
Ricarte, A., Tremmel, M., Natarajan, P., & Quinn, T. 2021a, ApJL, 916, L18
Ricarte, A., Tremmel, M., Natarajan, P., Zimmer, C., & Quinn, T. 2021b, MNRAS, 503, 6098
Rigault, M., Neill, J. D., Blagorodnova, N., et al. 2019, A&A, 627, A115
Robitaille, T. P., Tollerud, E. J., Greenfield, P., et al. 2013, A&A, 558, A33
Rodriguez-Gomez, V., Genel, S., Vogelsberger, M., et al. 2015, MNRAS, 449, 49
Rybicki, G. B., & Lightman, A. P. 1986, rpa (Wiley), 400
Sadowski, A., & Narayan, R. 2016, MNRAS, 456, 3929
Sandoval, L. E., Maccarone, T. J., Corsi, A., et al. 2018, MNRAS: Letters, 480, L146
Sazonov, S. Y., Ostriker, J. P., & Sunyaev, R. A. 2004, MNRAS, 347, 144
Schlegel, D. J., Finkbeiner, D. P., & Davis, M. 1998, ApJ, 500, 525
Schulze, S., Yaron, O., Sollerman, J., et al. 2021, ApJS, 255, 29
Scoville, N., Aussel, H., Brusa, M., et al. 2007, ApJS, 172, 1
Seabold, S., & Perktold, J. 2010, Statsmodels: Econometric and Modeling with Python, in 9th Python in Science Conf., 57
Shappee, B. J., Prieto, J. L., Grupe, D., et al. 2014, ApJ, 788, 48
Sicilia, A., Lapi, A., Boco, L., et al. 2022, ApJ, 924, 56
Skilling, J. 2004, AIPC, 735, 395
Skilling, J. 2006, BA, 1, 833
Sollerman, J., Fremling, C., Perley, D., & Laz, T. D. 2024, TNSTR, 2024-2511, 1
Somalwar, J. J., Ravi, V., Dong, D. Z., et al. 2023, ApJ, 982, 163
Somalwar, J. J., Ravi, V., Yao, Y., et al. 2025
Speagle, J. S. 2020, MNRAS, 493, 3132
Steidel, C. C., & Sargent, W. L. W. 1992, ApJS, 80, 1
Sun, N. C., Maund, J. R., Crowther, P. A., & Liu, L. D. 2022, MNRAS: Letters, 512, L66
Takeo, E., Inayoshi, K., Ohsuga, K., Takahashi, H. R., & Mineshige, S. 2019, MNRAS, 488, 2689
The Astropy Collaboration, Price-Whelan, A. M., Lim, P. L., et al. 2022, ApJ, 935, 167
The Astropy Collaboration, Price-Whelan, A. M., Sipőcz, B. M., et al. 2018, AJ, 156, 123
Tonry, J. L., Denneau, L., Heinze, A. N., et al. 2018, PASP, 130, 064505
Tsuna, D., & Lu, W. 2025, ApJ, 986, 84
Tuna, S., Metzger, B. D., Jiang, Y.-F., et al. 2025, ApJ, 989, 27
Ulmer, A. 1999, ApJ, 514, 180
Van Der Walt, S., Colbert, S. C., & Varoquaux, G. 2011, CSE, 13, 22
van Velzen, S., Gezari, S., Cenko, S. B., et al. 2019, ApJ, 872, 198
van Velzen, S., Gezari, S., Hammerstein, E., et al. 2021, ApJ, 908, 4
Verner, D. A., Ferland, G. J., Korista, K. T., & Yakovlev, D. G. 1996, ApJ, 465, 487
Virtanen, P., Gommers, R., Oliphant, T. E., et al. 2020, NatMe, 17, 261
Walt, S. J. v. d., Crellin-Quick, A., & Bloom, J. S. 2019, JOSS, 4, 1247
Weller, E. J., Pacucci, F., Hernquist, L., & Bose, S. 2022, MNRAS, 511, 2229
Wen, Z. L., & Han, J. L. 2024, ApJS, 272, 39
Wilms, J., Allen, A., & McCray, R. 2000, ApJ, 542, 914
Woosley, S. E. 2017, ApJ, 836, 244
Wu, S., Coughlin, E. R., & Nixon, C. 2018, MNRAS, 478, 3016
Wu, S. C., & Fuller, J. 2022, ApJL, 940, L27
Yao, Y., Chornock, R., Ward, C., et al. 2025, ApJL, 985, L48
Yao, Y., Ho, A. Y. Q., Medvedev, P., et al. 2022, ApJ, 934, 104
Yao, Y., Guolo, M., Tombesi, F., et al. 2024, ApJ, 976, 34
Yao, Y., Lu, W., Guolo, M., et al. 2022, ApJ, 937, 8
Yao, Y., Ravi, V., Gezari, S., et al. 2023, ApJL, 955, L6
Zou, H., Gao, J., Xu, X., et al. 2021, ApJS, 253, 56